Sensorless Position Control of Piezoelectric Ultrasonic Motors: a Mechatronic Design Approach

THÈSE N^{O} 4752 (2010)

PRÉSENTÉE LE 27 AOÛT 2010

À LA FACULTÉ SCIENCES ET TECHNIQUES DE L'INGÉNIEUR
LABORATOIRE D'ACTIONNEURS INTÉGRÉS
PROGRAMME DOCTORAL EN SYSTÈMES DE PRODUCTION ET ROBOTIQUE

ÉCOLE POLYTECHNIQUE FÉDÉRALE DE LAUSANNE

POUR L'OBTENTION DU GRADE DE DOCTEUR ÈS SCIENCES

PAR

Markus FLÜCKIGER

acceptée sur proposition du jury:

Prof. A. Billard, présidente du jury
Prof. Y. Perriard, directeur de thèse
Prof. H. Bleuler, rapporteur
Prof. B. Dehez, rapporteur
Prof. E. A. Lomonova, rapporteur

ÉCOLE POLYTECHNIQUE
FÉDÉRALE DE LAUSANNE
Suisse
2010

Sensorless Position Control of Piezoelectric Ultrasonic Motors

a Mechatronic Design Approach

Neuchâtel, EPFL
2010

To Ilona, Gudrun and Paul

Abstract

This dissertation considers mechatronic systems driven by piezoelectric ultrasonic motors (PUM). The focus is set on optimal system design and sensorless position control.

Mechatronic industry faces the challenge to deliver ever more efficient and reliable products while being confronted to increasingly short time to market demands and economic constraints driven by competition. Although optimal design strategies are applied to master this challenge, they do not entirely respond to the given circumstances, as often only local criteria are optimised. In order to obtain a globally optimal solution, the many subfunctions of a mechatronic system and their models must be interrelated and evaluated concurrently from the very beginning of the design process.

In this context PUM have been used increasingly during the last decade for various positioning applications in the field of mechatronic systems, laboratory equipment, and consumer electronics where their performances are superior to conventional electromechanical drive systems based on DC or BLDC motors. The position of the mobile component must be controlled. In some cases open-loop control is a solution, but more often than not sensors are used as feedback device in closed-loop control. Sensors are expensive, large in size and add fragile hardware to the device that compromises its reliability. Thus, not only the superior performance is not fully exploited but also the economical feasibility of the PUM drive system is jeopardised.

Replacing sensors by advanced control techniques is an approach to these problems that is well established in the field of BLDC motors. Those *sensorless control* strategies are not directly transferrable, because of the fundamentally

different working principles of PUM. Hence, the research of sensorless closed-loop position control techniques applicable to PUM and their validation with digitally controlled functional models is the very topic of this thesis.

We propose a dedicated design methodology to this statement of the problem. A core model of the mechatronic system is conceived as general and simple as possible. It then develops for the different interrelated views reflecting the mechanical, electromechanical, drive electronic, sensorial and digital control functions of the global system. Each one becoming more specific and detailed in this process, the different views still enable mutual constraint adjustments and the dynamic integration of results from the other views during the design process. Starting with the stator of the PUM, a view describes the mechanical displacement. An electric equivalent model is written such that power input from the drive electronics is related to the mechanical energy transmitted to the mechanics. The resulting differential equations are solved by the finite element method (FEM). Position feedback configurations in the mobile part of the PUM are modelled analytically in order to be implemented in digital control and their electrical implications are updated to the stator model. In this way, sensors do not necessarily materialise physically any more, but are distributed among the mechanical configuration, the drive electronics and the digital controller. With respect to the sensor data, the controller is not simply receiving finalised data on the measured system parameter, but rather implements the sensor itself in software.

Finally, the position detection performance obtained with the aforementioned design methodology was evaluated with the example of mechatronic locking devices actuated by custom-made as well as OEM motors. Functional models of motors, electronics and digital controllers were used to identify the limits of the proposed methods, and suggestions for further research were deduced. These results contribute to the development of robust sensorless position controllers for PUM.

Keywords: Piezoelectric ultrasonic motor, USM, Mechatronics, Sensorless position control, Digital control, Finite Element Method, Optimal design.

Zusammenfassung

Die vorliegende Dissertation behandelt durch piezoelektrische Ultraschallmotoren (PUM) angetriebene mechatronische Systeme. Den Schwerpunkt bilden die Entwurfstechnik sowie die sensorlose Positionsregelung.

Die in der Entwicklung mechatronischer Systeme Tätigen stehen vor der Herausforderung, immer leistungsfähigere und zugleich zuverlässigere Produkte liefern zu müssen, währen sie sich mit zunehmend kurzen Entwicklungzeitspannen und vom Wettbewerb getriebenen ökonomischen Zwängen konfrontiert sehen. Um dieser Aufgabe gerecht zu werden, kommen vermehrt fortschrittliche Entwurfstechniken zum Einsatz. Diese sind jedoch nicht zielführend wenn nur einzelne Funktionen optimiert werden. Um globale Optimallösungen zu erlangen müssen die Teilfunktionen mechatronischer Systeme und ihre jeweiligen Modelle zueinander in Bezug gesetzt und schon bei Beginn des Entwurfsprozesses simultan konzipiert werden.

In diesem Umfeld werden PUM vermehrt für Positionierungsaufgaben in mechatronischen Systemen, Laborgeräten und der Unterhaltungselektronik eingesetzt, wo ihre Eigenschaften jenen von Gleichstrom- oder Synchronmotoren überlegen sind. Bei diesen Anwendungen ist die Positionsregelung wesentlich. Meistens werden direkte Positionssensoren für die Rückführung im geschlossenen Regelkreis verwendet. Sensoren sind jedoch oft kostspielig, gross und die zusätzliche Gerätetechnik senkt die Zuverlässigkeit, was gewisse Vorteile von PUM zunichtemacht und die wirtschaftliche machbarkeit gefährdet.

Im Bereich der Synchronmotoren werden aus diesen Gründen Positionssensoren durch fortgeschrittene Methoden der Regelungstechnik ersetzt. Die technischen Grundlagen solcher *sensorlosen Regler* sind nicht direkt auf PUM über-

tragber. Hier setzt die vorliegende Dissertation an, indem nach Prinzipien gesucht wird, welche sensorlose geschlossene Positionsregelkreise für PUM zugänglich machen. Die entwickelten Steuerungen werden anhand von eigens entwickelten Funktionsmustern überprüft.

Wir schlagen eine zur Lösung dieser Problemstellung geeignete Entwurfs-Methodik vor. Ein Kernmodell des mechatronischen Systems wird so allgemein und einfach wie möglich aufgestellt. Davon ausgehend werden verschiedene in gegenseitiger Beziehung stehende Sichtweisen entwickelt, welche die Wechselbeziehung der mechanischen, elektromechanischen, elektronischen und sensorischen Komponenten des Gesamtentwurfs beschreiben. Während der Entwicklung dieser genaueren und zugleich spezifischeren Modelle wird darauf geachtet, dass jeweilige Anpassungen der Nebenbedingungen und die Integration von Resultaten bezüglich der anderen System-Funktionen möglich bleiben. Vom Stator des PUM ausgehend werden die Schritte der Energieumwandlung mit Hilfe von elektrischen Analogiemodellen beschrieben und in Bezug zu den konstitutiven Gleichungen der Piezoelektrizität gesetzt. Die resultierenden Differentialgleichungen werden mit der Methode der finiten Elemente (FEM) numerisch gelöst. Die Einrichtungen zur Stellungsrückmeldung des PUM-Rotors werden wiederum analytisch modelliert, und deren Auswirkungen auf das Betriebsverhalten im Statormodell in Betracht gezogen. In diesem Sinn sind Sensoren also nicht mehr physisch präsent, sondern verteilen sich auf die mechanische Konstruktion, die Antriebselektronik, sowie den zeitdiskreten Regler. Die Steuerung empfängt nicht direkt Positionsmessdaten, sondern wertet indirekte Messungen aus, um die Rotorposition softwarebasiert zu rekonstruieren.

Schliesslich wird die mit der obengenannten Entwurfsmethodik entwickelte sensorlose Positionssteuerung am Beispiel von mechatronischen Schliesszylindern ausgewertet. Sowohl eigens angefertigte als auch OEM PUM werden zu diesem Zweck beigezogen. Funktionsmuster der Positionierungssysteme dienen der Ermittlung ihrer Leistungsfähigkeit, als auch zur Identifikation von Leistungsgrenzen der vorgeschlagenen Methoden. Die Ergebnisse der vorgelegten Forschung tragen bei zur Entwicklung von robusten sensorlosen Positionsreglern für PUM.

Schlüsselwörter: Piezoelektrischer Ultraschallmotor, USM, Mechatronik, Sensorlose Positionssteuerung, Zeitdiskrete Regelungstechnik, Methode der finiten Elemente, Entwurfstechnik.

Acknowledgements

This dissertation was conducted at the Integrated Actuators Laboratory (LAI) at the Swiss Federal Institute of Technology in Lausanne and Neuchâtel (EPFL). In particular I would like to thank my thesis director Prof. Yves Perriard who was instrumental in identifying this challenging research topic. Prof. Perriard offered invaluable motivation while also allowing me significant latitude in developing the research project. I am very greatful for both of these qualities.

I would also wish to express my appreciation for the advice and support of many friends and colleagues. Especially, I would like to express my gratitude to:

- Prof. Aude Billard, the jury president, and the co-examiners Prof. Hannes Bleuler, Prof. Bruno Dehez, and Prof. Elena A. Lomonoava, for the inspiring discussions and their constructive comments on my work.

- Dr. Matteo Bullo who was my mentor at LAI, Dr. José Fernandez for the stimulating collaboration and for initiating me to FEM, Dr. John Murphy and Dr. Laurent Cardoletti for sharing their large knowledge in the field of digital control and motor drive electronics, Stéphane Burri for beeing my hands during the fabrication of functional models, my most loyal office mate Joël Maridor, Dr. Pierre-Daniel Pfister for his support at various occasions, Paolo Germano for answering questions just about everything, Dr. Christian Köchli for our stimulating discussions and the teaching experience in the frame of the microcontroller course, Omar Scaglione, Dr. André Hodder and the other colleagues at the LAI who contributed in various ways to this work.

- Prof. Roger Gassert, Dr. Dominique Chapuis, Prof. Dragan Damjanovic, Fabian Kägi, Dr. Jean-Marc Breguet, and Dr. Elena Vdovina Beck for their kind advice.

- Andreas Schürmann, Sébastien Bourgeois, and Tannessob Sob for their contributions to the research project during their Master thesis, Manfred Giljum for his contributions during his visit at LAI, Elmar Rothenhöfer for his expert advice in FEM contact modeling, as well as to Dayan Barloggio, Flavio Dias, Nils Karlsson, Frédéric Loizeau, Nicolas Lorétan, and Stefan Rigert, who worked on student projects.

- William Zogg, Dr. Andreas Häberli, Thomas Burger, and Bruno Wagner for the excellent collaboration in the frame of the KTI project with Kaba AG.

- Rainer Ott for bettering this thesis, Ursi Ott for support, and Roger Tremp.

This research has been funded in parts by the KTI (Kommission für Technologie und Innovation).

Markus Flückiger

Neuchâtel, June 2010

Contents

CHAPTER 1

Introduction

1.1 Research Objectives

This thesis develops a design methodology for the optimal integration of piezoelectric ultrasonic motors (PUM) into mechatronic systems. By doing so, we optimise the motor, the drive electronics and the position control method, while the interdependency of all subsystems is the gist of the design approach. The focus is set on the research of sensorless and self-sensing position control methods applicable to PUM.

1.2 Background and Development Trends

1.2.1 History of Piezoelectricity

Pierre and Jacques Curie first experimentally demonstrated the direct piezoelectric effect along with a superficial theoretical explanation in 1880 by clamping a variety of crystals in a jaw vice [34].

Lippmann had suggested in 1876 an analogy between heat energy and electric energy [124], a work on which he based his theoretical considerations on conservation of electric charge in 1881 [125]. Therein he stated that the piezoelectric effect, that had been demonstrated a year earlier, was reversible. He used

a thermodynamic approach to piezoelectricity to herald the converse piezoelectric effect. Though this perception was not compatible to the Curies mechanistic study, they adopted Lippmann's equations to predict the displacement amplitudes to be expected in a laboratory experiment. The same year they hence demonstrated the converse piezoelectric effect indirectly by measuring the pressure induced by the created displacement with a manometer [35]. A year later, an article brought the phenomenon recently demonstrated into line with contemporary research efforts in the field of crystallography. Relating it to pyroelectricity, it named the effect piezoelectricity [71], which gained general acceptance [175].

A first comprehensive mathematical description of crystal physics was published in 1910 [219]. It introduced the Voigt notation reducing symmetric tensors to matrices and vectors. To date it is the standard way of writing the constituent equations of piezoelectricity and will be applied in this work.

A comprehensive textbook focusing on piezoelectricity was published in 1946 [19].

The converse piezoelectric effect was referred to for motor concepts in 1942 [230]. The relative displacement of hemihedral crystals, however, was not important enough for the practical use in motors. Therefore research focused on alternative materials presenting a piezoelectric effect [96].

The search for a ceramic with a higher relative dielectric constant for use in capacitors led to significant though unpublished research efforts on barium titanate during World War II [67]. The discovery of its ferroelectricity [220] explained the good dielectric properties of the material. The crucial step for the use of piezoelectric ceramics was the evidence that barium titanate had piezoelectric properties when it was permanently poled by applying an electric field above coercivity [63].

Lead zirconate titanate (PZT) solid solutions near the tetragonal–rhombohedral phase boundary rapidly replaced the other ferroelectric ceramics due to its much stronger piezoelectricity [90]. Explicit expressions for piezoelectric constants in terms of microscopic variations in charge density induced by atom displacement have been derived and shown to depend only on the internal strain parameters and the first and second moments of the charge-density variation produced by motion of an atom, respectively [133]. Concerning PUM, some reports of practical implementations using the newly discovered PZT are found, but research aiming for large scale industrial use started only in Japan not prior to 1980 [212].

1.2.2 Piezoelectric Motors: History and Current State

First vibration motor concepts using composite piezoelectric crystal elements were suggested in 1942 [230]. However, only when stable piezoelectric ceramics

could be fabricated, practical realisation of piezoelectric motors came within range.

Piezoelectric transducers [6] [204], bimorph actuators [140], a first practical ultrasonic motor implementation [7] and quasistatic motors [134], later commercialised as the Inchworm motor, were proposed. Although refined motor concepts were proposed [217] and control methods suggested [215], due to the high cost of piezoelectric ceramics and technical problems regarding vibration amplitude control, these motors remained in an experimental stage, and were no valid alternative to contemporary stepper motors [24]. Integration into commercial products came only after further developments in Japan. A major motivation was the fast growing semiconductor industry's demand for positioners combining electromagnetic compatibility and high precision. The availability of piezoelectric ceramics at moderate cost further stimulated research activities [211].

After first comprehensive experiments with a standing wave motor [177], the traveling wave ultrasonic motor was patented in 1982 [178]. To this day, it is by far the best studied piezoelectric motor. After resolution of the control issues [95], it had gained publicity when integrated by Canon into their SLR autofocus lens promoted as the world's fastest. However, the traveling wave motor was replaced by multimode motors for economic reasons in succeeding products [234], [129].

Piezoelectric micromotors were developed in the field of robotics [167] and for wrist watch applications, either conventionally machined [147] or microfabricated [135], [52], [163]. Speed and position sensing is a particular challenge with these low power drives of very small size [162]. Dedicated self-oscillating drivers [203] [83] and rotor position detection methods were reported [164] [213] and commercialised for wrist watch applications [182].

At the time of writing, piezoelectric motors and actuators commercialised by original equipment manufacturers (OEM) encompass a large product range offering solutions to a multitude of positioning problems with a considerable variety of actuation principles and respective performances.

Actuators

Recent improvements of the manufacturing processes, piezoelectric ceramics and electrodes for piezoelectric stack actuators enable stiffer actuators with low electrical capacity, high specific displacement and decreased load and temperature influence on the overall performance [74]. Those ameliorations enable generally lower operation voltage, increased dynamics, result in acceptable performance at high and cryogenic temperatures, raise lifetime and hereby, open new application fields and markets. Not least, the position of competitors relying on

piezoelectric technology on the motor market strengthened by the development.

Positioning Motors With Subnanometer Resolution

Most of the properties immanent in actuators are found in motors, too. This is precisely because nanopositioning motors generally represent piezoelectric actuators in special assemblies and configurations. Motion is generated by successive and coordinated clamp/unclamp cycles of several actuators. In this way, motors with increased travel range are obtained, while preserving the crucial conveniences of the actuators. Friction at the stator-rotor interface is static. Therefore, wear and tear is neglectable and open-loop as well as self-sensing and auxiliary indirect sensor methods for closed loop position control remains feasible.

Multiaxis Positioning Systems

Multiaxis precision positioning stages driven by piezoelectric motors provide an interesting alternative to conventional electromagnetic and hydraulic solutions. In the subnanometer, low load segment, in the first instance in semiconductor industry, for waver arrangement, piezoelectric positioning stages have taken over due to their better precision combined with higher dynamics. But also as a replacement of hydraulic systems in airplanes and antenna alignment for radiotelescopes, where very high loads must be positioned precisely, piezoelectric motors are an option [37].

Piezoelectric Ultrasonic Motors

Piezoelectric ultrasonic motors generally operate at resonance. This enables high speed motors with extreme accelerations combined with a very low response time within small overall dimensions, leading to easy integration into mechatronic systems. Output force is significantly lower than for quasi-static motors. Obtained precision is an order of magnitude inferior. Therefore, piezoelectric ultrasonic motors are a good choice for positioning applications in the mm to cm travel range for applications where very short response times and high accelerations are crucial. Micrometer resolution is achieved in open-loop operation. For closed-loop control, position encoders are inevitable. Summarising, specific solutions exist first for positioning precision in the sub-nanometer span, combined with high active force but at low speed. For a large overall operation range, high dynamics and considerable speed of motion is available at precision in the micrometer span. Dedicated designs enable to a certain extend a trade-off between the two different application areas but, generally speaking, high speed and wide operation range are in contrast to high precision at high force. Whereas for

actuators and quasi-static motors conclusive solutions for precise position control exist, for ultrasonic motors, direct position sensors are necessary to enable closed-loop position control. Thus sensorless position control is the core issue where we are after new solutions with this thesis work.

1.2.3 Sensors

The breakthrough of handheld devices and the automation of many spheres of everyday life has tremendously increased the research efforts on small actuators and motors. Becoming apparent for many maybe with automated window lifters in cars and similar enjoyable aids, passing by image stabilising actuators in digital cameras and by far not ended with automated drug delivery to patients suffering from diabetes and other chronic diseases, integration of actuators is a discipline still pushing further miniaturisation, improving efficiency, and reducing cost. In this prospect, conventional sensors are a major hindering factor for achieving the design goals, as they are expensive, large in size and add fragile hardware to the device. Therefore, emerging methods replacing conventional sensors by indirect measurement and mathematic algorithms implemented in microprocessors advance the ongoing development [153].

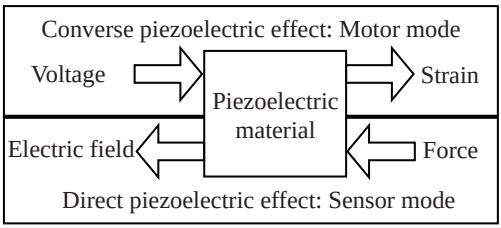

Figure 1.1. *Direct and converse piezoelectric effect and how they are exploited in a self-sensing actuator [151].*

With regard to piezoelectric motors, we differentiate between sensorless and self-sensing techniques. Sensorless control refers to the replacement of direct sensors measuring a system state by other sensors, mainly for current and voltage sensing, in conjunction with mathematic algorithms observing the same system state. First reports are found prior to 1980 with position observers for step motors [120]. A comprehensive study on observability and sensorless closed-loop control is presented by Antognini [4]. Self-sensing refers to the property of piezoelectric ceramics to function as actuator and sensor simultaneously by exploiting the indirect and direct piezoelectric effects, respectively (Fig. 1.1).

Benefitting from the emergence of ever faster and cheaper digital signal processors, complex algorithms nowadays can be implemented. Unless the technology of direct sensors would experience a comparable evolution, which is - at the very least - most unlikely, in the long run sensorless control will replace conventional control techniques.

1.2.4 The Future of Piezoelectric Materials

High power piezoelectric ceramics for ultrasonic motor applications need to have a high mechanical power factor and must be resistant to depoling or mechanical degeneration that may be caused by the relatively high electric fields applied for vibration generation at high frequencies. These aims are reached with acceptor doping and improved manufacturing processes of lead-zirconium-titanate (PZT) piezoelectric ceramics.

The vast majority of commercial PUM therefore use materials of this category, taken together under the classification of hard PZT, as active material. In this context, especially because piezoelectric motors should be biocompatible for certain applications, but also because the PZT manufacturing process (principle given in Eq. 1.1) as well as recycling of PZT are environmentally problematic, there is a necessity to replace PZT by less harmful materials.

$$PbO + ZrO_2 + TiO_2 \overset{heat}{\overset{700-800^\circ C}{\Longrightarrow}} \underbrace{Pb(Zr,Ti)O_3}_{powder} \overset{sinter}{\overset{1200^\circ C}{\Longrightarrow}} \underbrace{Pb(Zr,Ti)O_3}_{ceramic} \quad (1.1)$$

Furthermore, because the harmfulness of lead is not only scientifically proven since long [21], but today is generally accepted, legislation has been enforced. In the European Union lead is already banned for various applications under the *Restriction of the use of certain hazardous substances in electrical and electronic equipment (RoHS)* directive and other regions of the world apply similar restrictions or are about to follow. For now, application fields where hazardous substances are unavoidable are exempt. However, the exemption clause is revised every four years and it is most probable that PZT will be banned as soon as a valid replacement is available. Therefore, lead-free piezoelectric materials have been attracting attention worldwide as new materials in place of PZT-based piezoelectric ceramics. As a result, during the last decade a tremendous effort in finding lead-free ceramics as satisfactory replacements has been undertaken.

First steps towards lead-free ceramic materials suitable for practical use in piezoelectric actuators were done at the beginning of the 21st century. Piezoelectric ceramics using solid solutions of $(Sr,Ca)_2NaNb_5O_{15}$ (SCNN [232],[39])

and first materials with properties for the converse piezoelectric effect comparable to PZT were found by the Toyota research laboratories as published in *Nature* [176]. The reported composition $(K_{0.44}Na_{0.52}Li_{0.04})(Nb_{0.86}Ta_{0.10}Sb_{0.04})O_3$ ($KNLNTS$) showed best results. Other KNN contributions were published later [80], [101]. More recent developments include $BNLKT$ [238], [79] and research on the economic preparation of $KNLNTS$ [32]. Comprehensive reviews on these last developments are given by [169] and [199].

Recently, piezoelectric motors using KNN and SCNN lead-free piezoelectric ceramics have reached the prototype stage:

- KNN plate motors showed weak efficiencies and are sensible to wear and tear [201].
- KNN-based rotary motors were evaluated [112] [113].
- Using SCNN stacks, considerable efficiency improvements were achieved [41]. Prototype motors were tested for mobile device applications [40].
- Furthermore, $LiNbO_3$ single crystals were evaluated [200] and a standing wave motor was tested [202].

Notwithstanding all these arrived successes, the alternative materials only under optimal conditions reach the performances of PZT. In some niche application fields, those new materials appear adequate, but there is no general replacement ready yet. Therefore, with the prospect of being forced to realise PUM with less performing materials, but characteristics equivalent or better than those currently on the market, optimal design will gain an even bigger interest.

1.3 Mechatronic System Approach

Mechatronic industry faces the somewhat paradoxical challenge to deliver ever more performant and reliable products while being confronted to increasingly short time to market demands and economic constraints driven by competition. Expected to master the consequent ambition, the design engineer cannot rely on trial and error methods any more, but is increasingly dependent on comprehensive design strategies. Furthermore, mechatronic systems are combinations of many subsystems and every one of these is modeled in different ways for optimisation of the criterion in question. The integration of the different subsystems is only in its beginnings. Often the computer assisted design (CAD) model of the mechanics is not compatible with the model of the electromechanical conversion, which itself is not integrated with the electronic hardware model and the software. Thereby, no mathematically funded economic cost function can be

applied to the global system. Hence, even if optimisation procedures are applied to individual subproblems separately, the global design will not be optimal. Only when treating the optimal design of the subfunctions concurrently from the very beginning of the conceptual design stage, an optimal system may be obtained. In these circumstances the challenge arises of updating an existing product in prediction of future customer needs rather than as a response to them. Possibly, the new design therefore should respond to an eventually identified market opportunity. In the present study we address the case where a product is redesigned using a new technology in order to evaluate the promised superiority over the existing technology.

1.3.1 Application Example

The design methodology shall be verified with the example of a mechatronic locking device, wherein a mechanical locking configuration must be toggled between a locked and an open state at a low response time. The load to be moved is very small and the wanted motion range moderate. PUM respond best to the combined challenges of high safety, high efficiency, low cost in mass production, and easy integration into small mechatronic devices. As an additional benefit, a dimensional analysis shows that efficiency decreases linearly with volume reduction, whereas a quadratic decrease is observed for wound motors[147]. Important research has been done on innovative motor concepts[221], as well as optimisation of drive and control electronics[123]. However, efforts for optimal integration of these contributions are still rare and, as mentioned, in many cases position sensors are used for closed-loop control.

1.4 Dissertation Outline

With reference to the research objectives, and taking into account the actual circumstances in research on motors, sensors as well as mechatronic system development, we identify three main issues to be addressed.

1. Direct sensors are necessary for closed-loop position control, which implies low efficiency, high cost and low reliability.

2. High structural complexity of PUM leads to important manufacturing and assembly costs. We also observe that the majority of state of the art piezoelectric motors are driven by two or more phase shifted excitation signals [193]. Apart from developments on power electronics for piezoelectric actuators we therefore identify the need for motors with simplified working principles.

3. The rather complex electronics, operating at high frequencies, are another negative cost factor, which is an obstacle for commercialisation in many potential application fields. Motors should be drivable by a single low voltage signal, reducing the number, size and cost of the needed passive components such as inductors and capacitors in the drive electronics and obviating the need of power transformers.

In this context, we have to answer the following questions:

- How can the bulky, expensive and failure prone position sensors be effectively replaced?
- Which perspectives exist for simplifying the motor structures?
- Which optimal design methods respond best to the limitations with respect to piezoelectric materials and the particular working principles of PUM?

Aiming at a general formulation of the design methodology (Chapter 2) and the model views for motor optimisation (Chapter 3), drive electronics design (Chapter 4) as well as control (Chapter 5), the mechatronic locking device application is introduced in detail only in Chapter 6. An evaluation of the performance is reported in Chapter 7. General conclusions are drawn in Chapter 8.

CHAPTER 2

Design Methodology

Contents

2.1 Introduction

Already prior to the appearance of digital electronics and information technology, engineers were aware of the fact that a complex mechatronic system must be designed according to a well defined methodology. Strategies to search for innovative concepts, systematic methods for selecting the best one and procedures for design in detail were developed. The latter consisted generally in some kind of parametric analysis, an approach that evaluates the influence of selected design variables on the objective. A comprehensive review on design methodologies being beyond the scope of this thesis, the interested reader is referred to [145]. Some used designed experiments, allowing for parallel evaluation of

several design variables, but often every variable was evaluated independently, leading to an iterative design process [15]. The concept of a truly multidisciplinary design methodology however is rather new [36]. A sweeping innovation in the field of design methodologies unfolded only with the increasing computer performance and the consequent appearance of a variety of stochastic and deterministic optimisation tools.

As a consequence, for electromagnetic motors, where the involved physical phenomena are well understood, optimal design may therefore rely on global optimisation using the analytical models of the respective phenomena [29], [166] [155]. Pursuing the same final aim, a somewhat different starting point is encountered for PUM.

Whereas in the field of piezoelectric actuators models are available, this is not the case to the same extend for PUM.

In the first case, materials and the respective relations of applied charge and resulting displacement governed by the converse piezoelectric effect are fairly well understood [208] and referred to as what is known as the softening type nonlinearity [149]. Analytical models simultaneously useful for design and control [109] [30] are available. Hence, self–sensing position control is a widely established method in the fields of piezoelectric actuators, benders, cantilevers and in active vibration damping. There, very accurate models in conjunction with admissible assumptions for linearisation allow for self–sensing position feedback control using observers and similar reconstruction filter based techniques [168] [131] [192]. Therefore, in this case, integrated measurement and power electronics for piezoelectrical self–sensing actuators are suggested [103].

In the second case, however, when dealing with PUM, this is only half the picture. It is at the friction interface between stator and rotor, where the nature of the continuous motion of a PUM materialises. Comprehensive design models were developed [239], [70], [228] and further completed [240], but useful for control only in a very restricted way [185]. The main issue about these models is, that as much as they are useful for design and optimisation, heretofore no absolute rotor position detection is achieved on their basis. This is, effectively, because these models commonly feature a concentration on design relevant variables such as steady state speed and torque, or efficiency and related design parameters. Still more, the reason is that the amplitude-dependent nonlinearity that greatly influences the transient dynamics of the motor along with the complex stator/rotor contact phenomena, are just very complex [137]. Therefore, what is desirable for sensorless position control, equations linking the rotor position accurately to the drive signals for every operation condition, are not yet available.

In this respect, we first give a short overview on methods developed in the quest to fulfill the need for methodic design. Then, we aim to point out a frame-

work for the extension of pure model based optimisation towards a more global approach in the field of PUM based mechatronic systems featuring sensorless position control. Finally, a design methodology for a mechatronic system driven by a PUM is proposed.

2.2 Mechatronic Design Approach

Commonly, mechatronics is defined as *the synergistic integration of mechanical engineering, with electronics and intelligent computer control in the design and manufacturing of industrial products and processes* [87].

Fig. 2.1 gives a generic example of an electromechanical actuator inducing a mechanical process. First, the system is not configured optimally, as mutual constraints among the subsystems are taken into account only superficially. Second, because the components of the system are not designed in a global view, but each one separately, eventual synergies cannot be recognised.

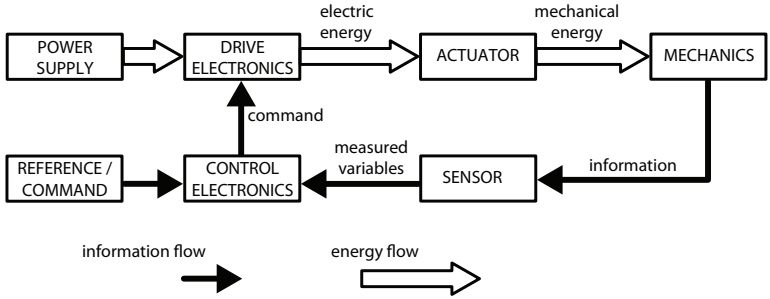

Figure 2.1. *Electromechanical system with electronic control*

Integration within a mechatronic system is hence put into practice in two parallel modes (Fig. 2.2). While the integration of components leads to an optimal configuration of the overall system, the integration by information processing allows for replacing entire system components such as sensors and introduces new opportunities with respect to advanced control and process supervision [86].

Rather than stringing together the components, a mechanical frame whose external dimensions are limited by application-specific constraints houses all the components of the mechatronic system. A power supply, often batteries, which are however more and more replaced by energy harvesters, supplies the electromechanical actuator through dedicated drive electronics with the needed electric energy. The actuator, fully integrated into the mechanical setup, transforms

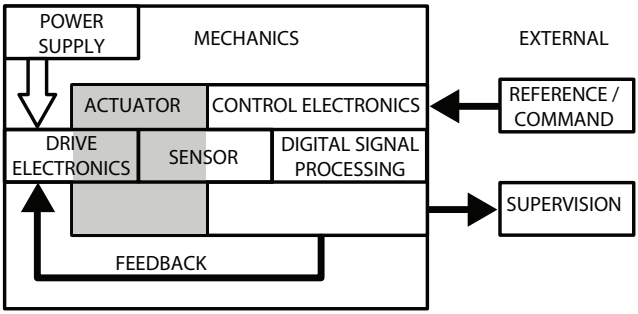

Figure 2.2. *Mechatronic drive system*

the electric to mechanical energy and induces the mechanical process. State variables of that process are directly sensed. The boundary of actuator and drive electronics blurs, as the electric part of the actuator itself is used to tune the drive signal optimally.

In a similar sense, this is true for the sensor, which is however distributed between the actuator or the mechanical process on the one side and the control electronics on the other, and usually does not materialise in its own physical dimension any more. Information treated within the control electronics usually composed mainly of a digital signal processor with its peripherals, allows for implementing advanced feedback control algorithms. Optionally, external references are given to the controller and some data is output for external supervision or into a global system controller.

This highly integrated design reduces dimensions not only by optimal mutual configuration of the integrated components but also by replacing former mechanical and electronic components by software. Removing mechanical and electronic components prone to failure also increases reliability. Generally, when exceeding a certain number of unities in batch production, the above detailed improvements lead to considerable reduction of production costs.

With these definitions, we can summarise that the system design approach consists in considering the mechanical, electronic and information processing components as an overall integrated system from the very beginning by applying a simultaneous engineering approach.

2.2.1 Simultaneous Engineering

Responding to those circumstances, we suggest a design methodology for mechatonic systems driven by PUM. Due to the discrete nature of the design problem, a

global deterministic optimisation based on an analytical system model is not feasible. Hence, the methodology consists of a combination of local optimisation and multiple criteria decision making strategies. The goal is to develop a design process, where the optimal design of all subfunctions is linked to the same core model. In concrete terms, the mechanical system, the actuator, drive electronics, sensors and the controller are optimised, if applicable, using models based on the same fundamental set of governing equations. The approach is introduced in Section 2.2.1.

In this way, we are able to establish a direct relation from the requirements of sensorless position control to the system design from the very beginning and throughout the design process up to the outcome of the final solution. With the mutual constraints established, every function of the system is designed using them as boundary conditions. The resulting iterative optimisation process of the subfunctions is introduced in Section 2.2.2.

With the aim of a globally optimal solution, we have further to choose the components fulfilling best their respective functions. For this purpose, a well-founded comparison method must be used (Section 2.2.3).

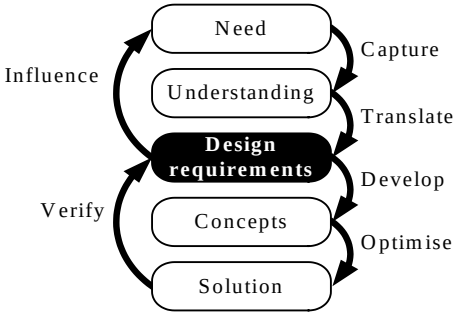

Figure 2.3. *Product creation process [161]*

We have to be aware of the fact, that the design process, starting with the requirement specifications and leading to a solution, is embedded in a larger process of product creation as illustrated in Fig. 2.3.

At the very beginning, a need is captured. Proper understanding of it lays the fundament for the translation to design requirements. This involves the analysis of any component of the mechatronic system and the factors influencing it. At this stage, the very need that emerges in the shape of customer requirements for instance may be influenced, which is however beyond the frame of the present work.

For here, at the point of departure are the requirement specifications. Because the required task is not solved by one system component alone, but different system components solve different tasks jointly, it is impossible to design and arrange them independently. On the contrary, mechanics, electronics and information processing must be considered as an integrated overall system from the very beginning of the design process. The tool used is a concurrent model based design approach referring to a core model [171].

Model views

Once the design requirement are initially defined, simultaneous engineering starts. A core model of the system develops for different views, while keeping the way open for mutual constraint adjustments and dynamical integration of the results from the other views (Fig. 2.4).

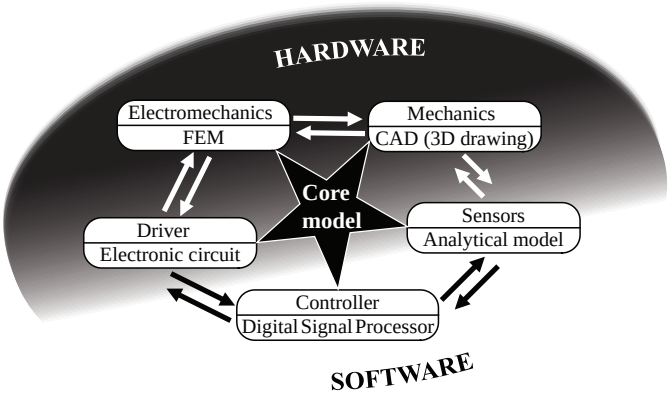

Figure 2.4. *Concurrent model based optimal design*

Electromechanics Starting with the stator of the PUM, a view must be developed that describes the mechanical motion. The equivalent electric circuit model is written in a way that power from the drive electronics relates to mechanical energy transmitted to the mechanics. The resulting differential equations are solved by the finite element model method.

Mechanics The mechanical configuration is designed with a computer assisted design (CAD) tool. Starting with the rotor of the PUM, which is purely me-

chanical, it must be conceived such that an indirect measurement of the relevant system parameters is possible. Then, the feedback to the stator must be updated in the electromechanical model of the stator on the one hand, and the effect of the integrated self–sensing feature must be modelled, on the other hand.

Sensor The sensor may be distributed among different subsystems of the mechatronic device or even materialise simply in a particular mechanical or electromechanical configuration, gaining its sensing properties only from a dedicated interpretation of the electric supply signals. However that be, a model must describe its variation as a function of the mapped system parameter. This is done preferably in an analytic manner in order to implement it easily in the control electronics.

Control Electronics The control electronics have external references and sensor data as input and output a command to the drive electronics as well as eventually some supervision data to be treated externally. With respect to the sensor data, it is not simply receiving finalised data on the measured system parameter, but rather implements the sensor itself in software using the analytical model which describes it.

Drive Electronics The driver is commanded by the control electronics output, and is in some way fusioned to the actuator. This in the sense that one must consider the overall electrical characteristics of the drive-motor system in order to design the drive signal according to the requirement specifications.

2.2.2 Iterative Design Process for the Subfunctions

As against earlier work on integrated actuator design, where integration consists in an optimal combination of the subsystems and the decision if some designated subsystems should be implemented in mechanical or electronic form [152], [111], [181] a further step is introduced here. On the one hand, using the advantages of the piezoelectric technology, design freedom with respect to geometric actuator shape is increased and allows for the creation of veritably integrated direct drives. On the other hand, integration of closed loop control is pushed further and a variable mechanical configuration of the load is converted to actuator position information according to [147]. However, these facts do not change the fundamental issues of integrated design, but represent only a further development. Hence, we are eligible to base the methodology on these antecedents and the design methodology for piezoelectric drives can follow the general concepts

employed for electromagnetic motors [29] [166]. As explained, the design requirements are in the center of any design process. Well compiled requirement specifications are the basis for concept development and give a framework for modelling, where a judicious constraint definition is fundamental for successful optimisation. Once an optimal solution is found, the specifications are verified with the design requirements and the model is updated according to eventual discrepancies in order to find the final optimal solution in an iterative design process (Fig. 2.5).

Every action taken during the process must have a clearly defined objective in order to reach the final aim of an optimal solution in the end. The main stages with their respective objectives are:

1. **Requirement specifications** Outgoing from the identified need requirement specifications are detailed. It is a crucial step in the design process, as all subsequent stages rely on the requirement specifications and In the end, performance is evaluated with respect to requirements. It encompasses a comprehensive definition of objective functions and global, component level and mutual constraints among the components as well as the definition of the figures of merit and their weighting.

2. **State of the art** Existing solutions to the design problem are evaluated in order to understand their benefits and eventual inconveniences. The gathered information lays the basis for the concept development, but by no means replaces the original process of innovation.

3. **Concept development** Innovation, new concepts, generally on the basis of existing principles, are searched for. If independent components exist, possiblities of mechanical integration and replacement of hardware by signal processing is evaluated.

4. **Selection** Based on the spadework done during the specification of the requirements, best suited concepts are selected.

5. **Optimisation** Employing mathematical optimisation algorithms with the objective functions and constraints as defined, selected subsystems are optimised. Results are fed back to the concurrent design process in order to implement them in the integration process (core model with concurrent constraint adjustment. The optimisation leads to a selection of the best solution for functional model fabrication.

6. **Validation** With the help of functional models the final design is refined. A performance evaluation with respect to the requirements allows for validating the design.

7. **Prototyping** Final solution ready for field tests and then industrialisation.

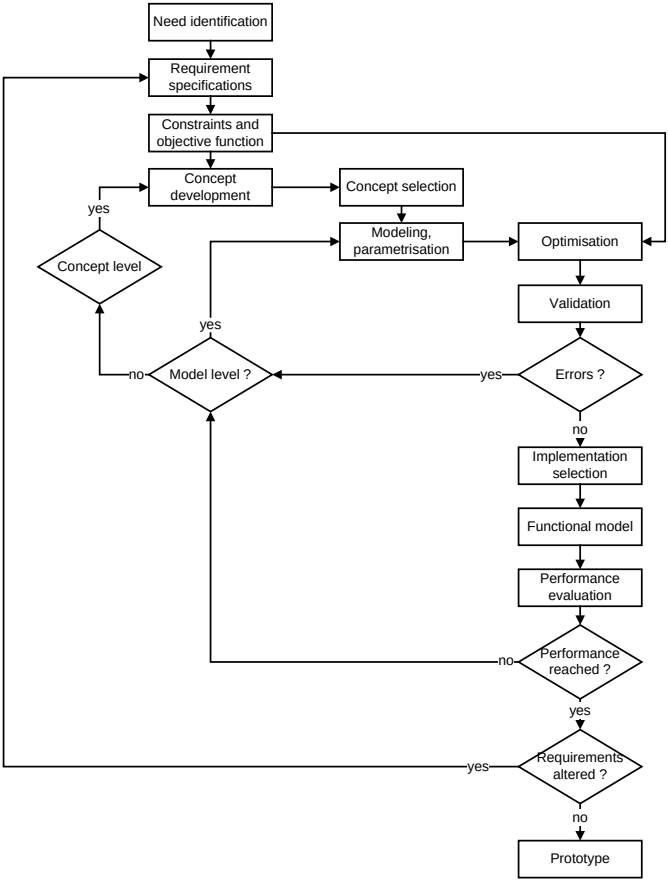

Figure 2.5. *Optimal design process of subfunctions*

2.2.3 Selection

A purely qualitative selection of solutions contains the risk of wrong decisions due to the human factor and is therefore not worth striving for. Multiple Criteria Decision Making (MCDM) has therefore become an important research topic

and some achievements may be outlined here. Increasingly researched by Chen [28] and others, different methods exist [144], up to fuzzy analytic hierarchy processes [207].

Notwithstanding, due to two main factors, analytical MCDM methods are not applicable as is in the present case. First, some requirements are fulfilled only by the complete system, but not by the particular components. A purely mathematical method would have to consider the fact that some of the requirements can be fulfilled through the combination of components. Second, quantification of the decision criteria must be controllable also for intermediate performance values, and not only at the global performance evaluation stage.

Consequently, we use a combination of figures of merit and quantitative comparison after optimisation to find the best solution, as illustrated in Fig. 2.6.

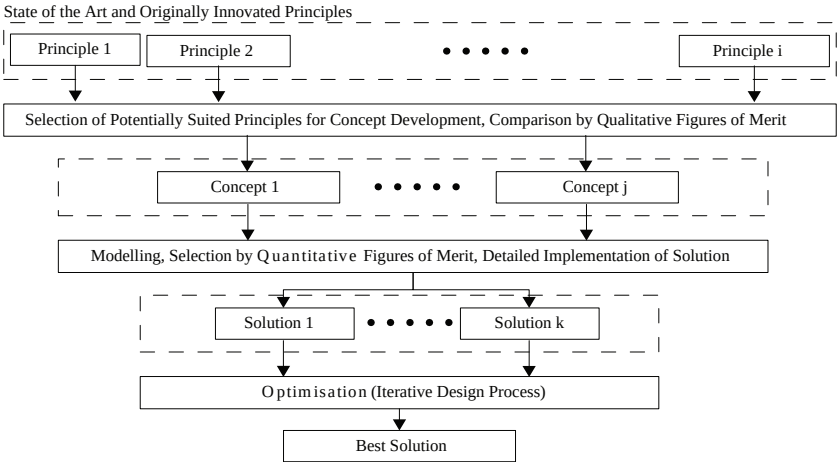

Figure 2.6. *Selection Process*

2.2.4 Implementation

The methodology is implemented in the following chapters. The development of the core model and its implementation for optimal stator design (Chapter 3) is followed by the drive electronics design (Chapter 4), the controller development (Chapter 5) and finally the integration of the subfunctions (Chapter 6) as well as a performance evaluation. The process of performance evaluation is distributed as for the implementation of every subsystem, the intermediate performance criteria

are evaluated. Finally, performance and limitations of the complete system in different configurations are presented in Chapter 7, and evaluated with respect to the requirement specifications.

CHAPTER 3

Core Model and Optimal Stator Design

Contents

3.1 Background

Piezoelectric ultrasonic motors are characterised by two stages of energy conversion. Electrical energy is converted to mechanical vibration by the means of the converse piezo-electric effect in the stator. At the interface between stator and rotor, frictional coupling transforms these vibrations to a continuous motion

of the rotor. This second-stage conversion of stator to rotor motion is a vibro-impact system and inherently displays non-linear dynamics because vibration cycles of the stator surface cease to be symmetric due to impact with the rotor [51] (Fig. 3.1). Because friction models are non-linear and, especially in the case of intermittent contact, become very complex [239] [70] [228] [240] [185] [128] [180] they are clearly not useful as a basis for a sensorless position controller and their applicability to optimisation remains disputed.

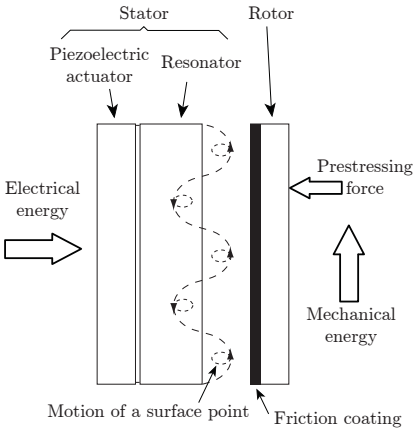

Figure 3.1. *Working principle of a piezoelectric ultrasonic motor: Electrical energy is converted to mechanical vibration by the means of the converse piezoelectric effect. A friction interface transforms these vibrations to a continuous motion (Adaption from [211]).*

3.2 Objectives

Electric equivalent models are a very useful analysis tool and are widely used for PUM design. One of the most comprehensive approaches is the one by Sashida [179]. An analysis model is developped in the equivalent model methodology, representing in a very detailed manner the non-linearities and losses present in the motor. We are looking for a strategy, which differs therefrom in two decisive intentions. First, we intend to develop a controller that is able to keep the working point of the motor in its approximately linear operation range for all operating conditions, even at start-up. Therefore the motor behaviour is supposed to be linear and only the linear operation range is modelled. Second, the working principles of PUM being already well understood and described in the state of the art [209] we do not aspire after a very precise analysis model. Rather, we

must develop a model describing the electric and mechanical components of the motor in a way allowing us to understand by and large the feedback from the mechanics to the drive signals to be used for self-sensing position. Further, such a model will also be useful to apprehend the results from FEM optimisation. Therefore, the objective of this work is to use a model that can be implemented in different views, while clearly defining the passage from one view to another. Every view shall proof useful for the design of one of the major system components, respectively. In this sense, after presenting the model, a view for stator design is developped in this Chapter, a view for the design of the drive electronics is implemented in Chapter 4 and finally the view for the self-sensing position controller in Chapter 5.

3.3 Derivation of the Electric Equivalent Model

Based on the constitutive equations of piezoelectricity and the electric equivalent model of a pieoelectric ceramic element is developped. It will conduce as core model to the design process and to the self-sensing position controller. Details on the notation are found in Appendix B.1.

The relative mechanical displacement S of an elastic solid under constraint T is given by the Hooke's Law:

$$S = sT \tag{3.1}$$

where s is the compliance of the medium expressed in $[m^2/N]$. Within a dielectric material exposed to an electric field E, the electric displacement D is

$$D = \epsilon E \tag{3.2}$$

where ϵ is the dielectric constant of the medium expressed in $[Cm/V]$. In a piezoelectric material, the mechanical and electric effects affect each other:

$$\text{direct piezoelectric effect: } \frac{\partial D}{\partial T} \neq 0 \tag{3.3}$$

$$\text{converse piezoelectric effect: } \frac{\partial S}{\partial E} \neq 0 \tag{3.4}$$

This interaction can be approximated by linear relations among the four variables D, E, S and T, wherefrom only two are independant. Choosing arbitrarly

one mechanical and one electric variable as independant, say S and D, the linear relations write:

$$S = \left.\frac{\partial S}{\partial T}\right|_E T + \left.\frac{\partial S}{\partial E}\right|_T E \tag{3.5}$$

$$D = \left.\frac{\partial D}{\partial T}\right|_E T + \left.\frac{\partial D}{\partial E}\right|_T E \tag{3.6}$$

Using

$$s^E = \left.\frac{\partial S}{\partial T}\right|_E \qquad d = \left.\frac{\partial S}{\partial E}\right|_T \tag{3.7}$$

$$d = \left.\frac{\partial D}{\partial T}\right|_E \qquad \epsilon^T = \left.\frac{\partial D}{\partial E}\right|_T \tag{3.8}$$

Equations (3.6) yield

$$S = s^E T + dE \tag{3.9}$$

$$D = dT + \epsilon^T E \tag{3.10}$$

and similarly, by choosing T and D as independant variables:

$$T = c^E S - e^t E \tag{3.11}$$

$$D = eS + \epsilon^S E \tag{3.12}$$

The coefficients s, d, ϵ and e beeing the principle material constants. For piezoelectric ceramics, they can be found only empirically and the values provided by the manufacturers diverge by up to 20%.

The piezoelectric effect being inherently anisotrope, these coefficients depend on the direction. The axis definition for piezoelectric ceramics is given in Fig. 3.2. The coordinate system is not based on the crystallographic lattice direction, but the positive polarization direction is defined as the Z axis of the orthogonal system. The X, Y and Z axes are respectively noted 1, 2 and 3, while the rotations around each axis are noted 4, 5 and 6. To indicate the direction, two indexes are attributed to the coefficients. The first defines the direction of the cause, the second the direction of the effect.

Compliance s^E_{13} is the compliance at constant electric field for a constraint in direction 1 and displacement along direction 3.

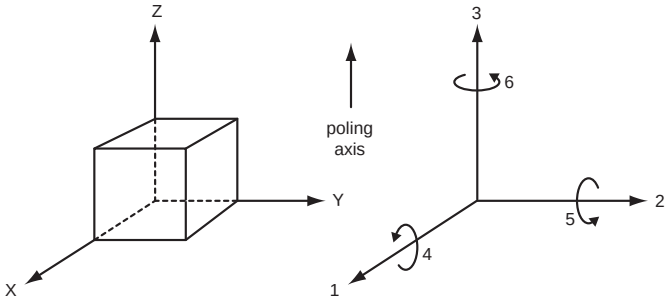

Figure 3.2. *Definition of directions*

Permittivity ϵ_{33}^{T} is the permittivity for a displacement and an electric field in polarization direction with constant constraint.

Piezoelectric constants The first index corresponds to direction of the electric variable (field or displacement) and the second to the mechanical variable (constraint or displacement). Hence, d_{13} may link both, or the displacement along direction 1 to the electric field along direction 3 or the dielectric displacement along direction 1 to the constraint along direction 3:

$$d_{31} = \left.\frac{S_1}{E_3}\right|_T = \left.\frac{D_3}{T_1}\right|_E \tag{3.13}$$

3.3.1 Piezoelectric Coupling and Circuit Model

Following a method developed in electro-acoustics and since widely used in the field of piezoelectric actuator design, it is possible to model the piezoelectric coupling by a schematic using a bipole that realizes an ideal transformation between a mechanical and an electrical parameter. This representation is then used to deduce an electric equivalent circuit of the piezoelectric actuator which may be used as core model as explained afterwards.

For the derivation of the electric equivalent circuit we consider a square piezoelectric sample clamped to the bottom according to [173], which represents a very simple realisation of a piezoelectric actuator (Fig. 3.3). The model obtained in such a way is then easily extensible to different and more complex motor configurations. The procedure allows therefore for obtaining an equivalent circuit model that is valid for all piezoelectric motors treated in this work. Defining:

ξ Displacement of the top face defining a speed $v = \dot{\xi}$,

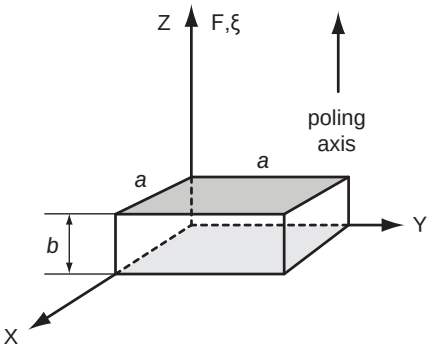

Figure 3.3. *Piezoelectric plate*

Q Electrical charge defining an electric current $i = \dot{Q}$,

U_c Voltage applied to the electrodes,

F_c Traction applied to the plate,

d Piezoelectric charge constant,

and supposing small variation around static values, charge and displacement may be expressed as linear functions, respectively:

$$Q = dF_c \tag{3.14}$$

where d is the piezoelectric charge module in $\frac{C}{N}$,

$$\xi = dU_c \tag{3.15}$$

where d has the unities $\frac{m}{V}$.

When voltage U_c and traction F_c are applied simultaneously, the displacement is the sum of the one induced by the applied voltage given in Equation 3.15 and the one due to the applied force, calculated applying the compliance of the short-circuited piezoelectric plate C: $\xi = CF_c$. Similarly, electrical charge is the sum of Equation 3.14 and the charge induced by an applied voltage on the

unconstrained piezoelectric plate, calculated with its free static capacitance C_0': $Q = C_0' U_c$. The piezoelectric coupling is hence defined by:

$$Q = C_0' U_c + dF_c \tag{3.16}$$

$$\xi = CF_c + dU_c \tag{3.17}$$

The sinusoidal steady state solution of these equations writes:

$$\underline{I} = j\omega C_0' \underline{U_c} + j\omega d \underline{F_c} \tag{3.18}$$

$$\underline{v} = j\omega C \underline{F_c} + j\omega d \underline{U_c} \tag{3.19}$$

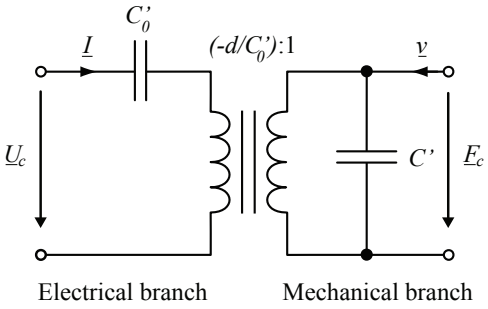

Figure 3.4. *Equivalent Circuit*

The piezoelectric coupling coefficient $(j\omega d)^{-1}$ defines the ratio of voltage $\underline{U_c}$ to speed $\underline{v}$ of the unconstraint piezoelectric element and, reciprocally, the ratio of force $\underline{F_c}$ to current $\underline{I}$ with short-circuited electrodes. It is an imaginary number as the coupling equations are written as functions of the characteristic parameters $\underline{U_c}$, $\underline{I}$, $\underline{F_c}$, $\underline{v}$, and not as functions of the effectively coupled variables voltage and displacement as well as force and charge. Therefore, the piezoelectric coupling can not be represented by a simple two port device, because as well in the case of a transformer as for a gyrator, the respective ratios must be real numbers.

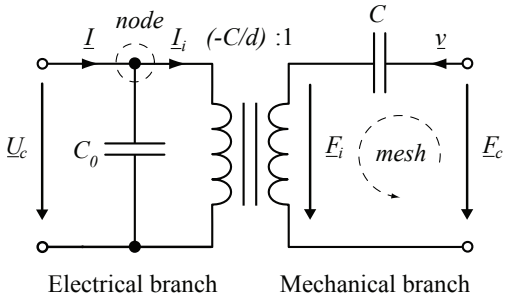

Figure 3.5. *Equivalent Circuit*

From the schematic representation given in Fig. 3.5 the coupling is defined with equations (3.20) and (3.21):

$$\underline{U_c} = \frac{-C}{d}\underline{F_i} \tag{3.20}$$

$$\underline{I_i} = \frac{d}{C}\underline{v} \tag{3.21}$$

With Kirchhoff [92] we write the nodal rule of the electric branch

$$\underline{I} - \underline{U_c} j\omega C_0 - \underline{I_i} = 0 \tag{3.22}$$

and the mesh rule of the mechanical branch

$$\underline{F_i} + \frac{\underline{v}}{j\omega C} - \underline{F_c}. \tag{3.23}$$

Plugging (3.20) into (3.23) we find the piezoelectric coupling equation for displacement (3.19)

$$\underline{v} = j\omega C\underline{F_c} + j\omega d\underline{U_c} \tag{3.24}$$

and using (3.22) with (3.21) , (3.23) and (3.20) , we find

$$\underline{I} = j\omega\underline{U_c}\left(C_0 + \frac{d^2}{C}\right) + j\omega d\underline{F_c} \tag{3.25}$$

which equals (3.18) for

$$C_0' = C_0 + \frac{d^2}{C}. \tag{3.26}$$

With respect to Fig. 3.4, we are now able to determine the static capacitor in blocked state ($v = 0$) C_0 and the mechanical compliance C' in open circuit condition using (3.26):

$$C_0 = C_0' - \left(\frac{d^2}{C}\right) \tag{3.27}$$

$$C' = C - \left(\frac{d^2}{C_0}\right) \tag{3.28}$$

The coefficient $\left(\frac{d^2}{C}\right)$ links the equivalent capacitance C_m to the mechanical compliance C

$$\left(\frac{d^2}{C}\right) = \left(\frac{d}{C}\right)^2 C = C_m \tag{3.29}$$

because $\left(\frac{d}{C}\right)^2$ is the inverse square of the transformer ratio in the quadripole representation [91].

This validates the representation of the piezoelectric coupling by the schematic of Fig. 3.5.

Defining the relative variables according to the piezoelectric plate (Table 3.1), the equations governing the piezoelectric coupling (3.16) and (3.17) are linked to the constitutive Equations:

$$AD = \epsilon\frac{A}{b}bE + dAT \tag{3.30}$$

$$bS = \frac{b}{\tilde{E}A}AT + dbE \tag{3.31}$$

The compliance matrix for constant electric field $s^E = \frac{1}{\tilde{E}}$ and permittivity for constant stress $\epsilon^T = \tilde{\epsilon}$ yield the constitutive Equations

$$D = dT + \epsilon^T E \tag{3.32}$$

$$S = s^E T + dE. \tag{3.33}$$

Variable	Definition	SI units
Relative displacement	$S = \frac{\xi}{b}$	$[-]$
Stress	$T = \frac{F_c}{A}$	$[N/m^2]$
Electric field	$E = \frac{U_c}{b}$	$[V/m]$
Electric displacement	$D = \frac{Q}{A}$	$[C/m^2]$
Static capacity	$C_0' = \frac{\tilde{\epsilon} A}{b}$	$[F]$
Compliance	$C = \frac{b}{\bar{E} A}$	$[m/N]$

Table 3.1. *Piezoelectric plate equations*

3.4 FEM View of the Core Model

For the derivation of the FEM model we start with the constitutive equations of piezoelectricity with $\boldsymbol{T}$ and $\boldsymbol{D}$ as independent variables given in (3.12). In order to solve these equations according to the theory of finite elements, the set of differential equations must be completed by defining the respective relations among the involved quantities [110].

The elastic behaviour of the piezoelectric media is expressed by Newton's Law

$$F = \frac{\partial}{\partial t}\left(\rho \frac{\partial \xi}{\partial t}\right) \tag{3.34}$$

and writes with force defined as the divergence of the dyadic stress tensor $\boldsymbol{T}$, $F = \nabla \cdot \boldsymbol{T}$:

$$\nabla \cdot \boldsymbol{T} = \frac{\rho \partial^2 \boldsymbol{\xi}}{\partial t^2} \tag{3.35}$$

with the density of the piezoelectric medium ρ and the mechanical displacement $\boldsymbol{\xi}$. Further, the electric behaviour assuming insulating piezoelectric media is

given by the Maxwell's Equation.

$$\nabla \cdot \boldsymbol{D} = 0 \tag{3.36}$$

Expressing the electric field in terms of electric potential Φ

$$\boldsymbol{E} = -\nabla\Phi \tag{3.37}$$

and the mechanical strain in terms of the mechanical displacement ξ

$$\boldsymbol{S} = \begin{pmatrix} \frac{\partial}{\partial x} & 0 & 0 \\ 0 & \frac{\partial}{\partial y} & 0 \\ 0 & 0 & \frac{\partial}{\partial z} \\ \frac{\partial}{\partial y} & \frac{\partial}{\partial x} & 0 \\ 0 & \frac{\partial}{\partial z} & \frac{\partial}{\partial y} \\ \frac{\partial}{\partial z} & 0 & \frac{\partial}{\partial x} \end{pmatrix} \boldsymbol{\xi} = \boldsymbol{B}\boldsymbol{\xi} \tag{3.38}$$

we can solve the now complete set of differential equations (3.12 and 3.35-3.38) with appropriate boundary conditions for mechanical displacements and forces, as well as electrical potential and charge using Hamilton's variational principle as extended to piezoelectric media [206].

$$\delta \int L dt = \int \left(E_d - E_e + E_c + W\right) dt = 0 \tag{3.39}$$

with δ denoting the first-order variation.

The energies described by the Lagrangian term are the dielectric energy

$$E_d = \frac{1}{2} \iiint_V \boldsymbol{D}^t \boldsymbol{E}\, dV, \tag{3.40}$$

elastic energy

$$E_e = \frac{1}{2} \iiint_V \boldsymbol{S}^t \boldsymbol{T}\, dV, \tag{3.41}$$

kinetic energy

$$E_c = \frac{1}{2} \iiint_V \rho \dot{\boldsymbol{\xi}}^{\mathbf{2}} \, dV, \tag{3.42}$$

and work done by the exciting electrical field and externally applied forces

$$W = \iiint_V \boldsymbol{\xi}^t \boldsymbol{F_B} \, dV + \iint_{A_F} \boldsymbol{\xi}^t \boldsymbol{F_S} \, dA_F - \iint_{A_C} \boldsymbol{\Phi} Q_S \, dA_C + \sum \boldsymbol{\xi}^t \boldsymbol{F_P} - \sum \boldsymbol{\Phi} Q_P \tag{3.43}$$

where

V	Volume of the piezoelectric medium $[m^3]$
A_C	Surface where charges are applied $[m^2]$
A_F	Surface where forces are applied $[m^2]$
$\boldsymbol{F_B}$	Vector of mechanical body forces $[N/m^3]$
$\boldsymbol{F_S}$	Vector of mechanical surface forces $[N/m^2]$
$\boldsymbol{F_P}$	Vector of mechanical point forces $[N]$
Q_S	Surface charges $[As/m^2]$
Q_P	Point charges $[As]$

On this basis FEM consists in the subdivision of a complex system to be computed into small discrete elements defined by their nodes, where the mechanical and electrical quantities ξ, F, Φ and Q are calculated. The process of subdivision may be automated and is called meshing. The values of these variables are determined at an arbitrary position of the system by a linear combination of polynomial interpolation functions $N(x, y, z)$ and the nodal point values of the variables as coefficients. Instead of building the FE model by defining every singel node of every element individually, we exploit the powerful tools provided by the commercial FEM software Ansys[1]. A CAD model thoroughly designed for FEM serves as solid model for Ansys. It is defined by key points, lines, areas and volumes. Functioning as a basis for generating the FE model, the solid model must anticipate the particularities of meshing. Furthermore, a dedicated element design ascertains precision and avoids errors during the solving process. We choose the 10-node tetrahedral element with quadratic displacement behavior, designated as SOLID98 by Ansys, which is well suited to model irregular

[1] Ansys is a software for finite element modeling for the solution of non-linear problems in the fields of fluid- and thermodynamics, piezoelectricity and electromagnetism. www.ansys.com

meshes. For instance, the displacement ξ is then evaluated as

$$\xi(x,y,z) = \sum_{i=1}^{10} (N_{\xi,i}(x,y,z)\xi_i(x_i,y_i,z_i)) \tag{3.44}$$

where $N_{\xi,i}$ is the interpolation function of the displacement.

The other variables are interpolated by analogy, using appropriate interpolation functions. With the vector of nodal point displacements ξ_i (order 30), and analogically, for the nodal forces F_i, electric potentials Φ_i and charages Q_i.

With the interpolation functions for the displacement $\boldsymbol{N}_\xi$ and the electric potential $\boldsymbol{N}_\Phi$, (3.37) and (3.38) write:

$$\boldsymbol{E} = -\nabla\boldsymbol{\Phi} = \nabla\left(\boldsymbol{N}_\Phi\boldsymbol{\Phi}_i\right) = -\boldsymbol{B}_\Phi\boldsymbol{\Phi}_i \tag{3.45}$$

$$\boldsymbol{S} = \boldsymbol{B}\boldsymbol{\xi} = \boldsymbol{B}N_\xi\xi_i = \boldsymbol{B}_\xi\boldsymbol{\xi}_i \tag{3.46}$$

where $\boldsymbol{B}_\phi$ and $\boldsymbol{B}_\xi$ are the spatial derivatives of the respective interpolation function arrays.

The solution of the Lagrangian (3.39) by applying the aforementioned approximation yields the set of linear differential equations that describe one single piezoelectric finite element [42].

Finally, for the complete mesh, the differential equations for each finite element are collocated to (3.47), where forces and electric potentials are averaged to F and Φ on the region of interest.

$$\begin{bmatrix} M & 0 \\ 0 & 0 \end{bmatrix}\begin{bmatrix} \frac{\partial^2\xi}{\partial^2 t} \\ \frac{\partial^2\phi}{\partial^2 t} \end{bmatrix}+\begin{bmatrix} C & 0 \\ 0 & 0 \end{bmatrix}\begin{bmatrix} \frac{\partial\xi}{\partial t} \\ \frac{\partial\phi}{\partial t} \end{bmatrix}+\begin{bmatrix} K_{\xi\xi} & K_{\phi\xi} \\ K_{\xi\phi} & K_{\phi\phi} \end{bmatrix}\begin{bmatrix} \xi \\ \phi \end{bmatrix} = \begin{bmatrix} F \\ Q \end{bmatrix} \tag{3.47}$$

with the globally assembled field quantities as defined for numerical solution with Ansys:

$$M = \rho\iiint_V N_\xi^t N_\xi \, dV \tag{3.48}$$

the mass matrix,

$$K_{\xi\xi} = \rho \iiint_V N_\xi^t \boldsymbol{C} N_\xi \, dV \tag{3.49}$$

the stiffness matrix,

$$K_{\phi\phi} = \rho \iiint_V N_\phi^t \boldsymbol{\epsilon} N_\phi \, dV \tag{3.50}$$

the dielectric matrix,

$$K_{\xi\phi} = K_{\phi\xi}^t = \rho \iiint_V N_\xi^t \boldsymbol{d} N_\phi \, dV \tag{3.51}$$

the piezoelectric coupling matrix.
The Rayleigh damping matrix is expressed as

$$\boldsymbol{C} = \alpha M + \beta K_{\xi\xi} \tag{3.52}$$

where α is the mass damping and β the stiffness damping. These constants must be determined from two target damping ratios corresponding to two selected modes of vibration [42]. The mass damping constant being close to zero in our application [151], only β was considered for the numerical simulations.

3.5 Stator Optimisation Methodology

To respond to the need for efficient optimisation procedures adapted to the FEM simulation based design of piezoelectric motors, we use a dedicated design methodology that combines sensitivity analysis and FEM based optimisation algorithms [47]. It allows for well understanding the influence of the geometrical and physical parameters on the movement of the motor. The parameters with an important impact on the objective function, the vibration amplitude of the stator, are free during optimisation, the others are fixed. The methodology is applicable to any PUM topology and will be applied similarly for designing linear and rotary single-phase PUM with the goal of maximising output speed, force and torque, respectively. This is achieved by optimising the actuator geometry in order to increase the vibration amplitudes that cause the continuous movement. First of all,

the motor structure is parametrised. Then, with the aim of reducing the number of simulations, but also in order to limit the variation ranges of the simulation parameters, a preoptimisation stage is necessary. Thus, sensitivity analysis is carried out using design of experiments, which is a good way to obtain the influence of the input parameters on the objective function [15]. An optimisation study, based on the results from preoptimisation, is then realised using Ansys. The resonator shapes obtained at each stage of this optimisation process are fabricated and analysed in order to validate the design methodology in the case of the linear motor. After the successful validation we directly manufacture a functional model of the final optimised design in the case of the rotary motor. Interferometric vibration measurements validate quantitatively the FEM model along with the suggested design methodology.

3.5.1 FEM Based Design Optimisation

A sensitivity analysis allows for selecting significant design variables of a numerical model. The selected variables are then assigned as free parameters in a FEM based optimisation algorithm. The insignificant variables are fixed. Hereby the restriction of free variables reduces considerably the calculation time necessary for the optimisation without reducing the accuracy of the results.

3.5.2 Finite Element Method

FEM simulations are used first to perform the modal analysis and then to calculate the modal shapes at the selected frequencies with the respective harmonic and transient analyses. The particular methods are explained in Appendix B.2.

3.5.3 Preoptimisation

The objectives of the preoptimisation stage are twofold. On the one hand we aim to understand the influence of the different design variables on the objective function. Only those with an important influence are used for the optimisation in order to reduce calculation time. On the other hand, the fact to vary the design variables for the sensitivity analysis leads already to a preoptimised motor design [46]. The sensitivity analysis is performed according to the following steps:

- definition of the parameters to be analysed as design variables,
- creation of sets of values of the design variables according to an experimental design,
- FEM simulations,

- saving of the results vector,
- determination of the most significant design variables.

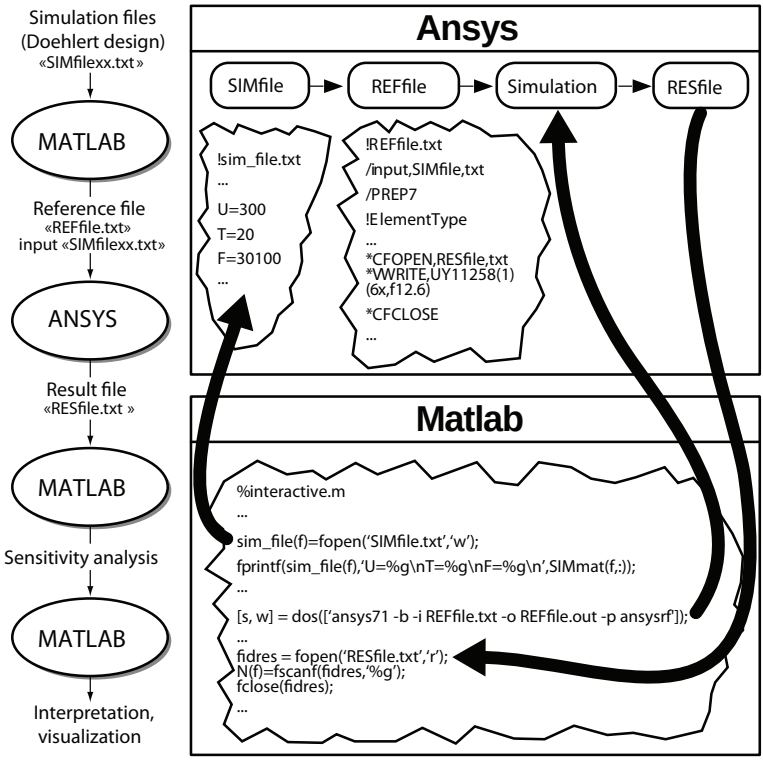

Figure 3.6. *Steps of the preoptimisation procedure [47]*

These different steps are carried out by using the Matlab[2] software in conjunction with Ansys. The first one is used to create simulation files by varying the design variables according to the selected method. Once these files are created, they are used in a reference file that is launched n times toward Ansys via Matlab in batch mode in order to execute the simulations according to the experimental design. At the end of each simulation, a result file is created by Ansys and

[2]Matlab is a commercial, platform independant software for the solution of mathematical problems and the graphical representation of results. It is particularly designed for matrix calculation, wherefrom its name is derived: MATrix LABoratory. www.mathworks.com

treated with Matlab, which stores the obtained results in a vector. This answer vector is then analysed to determine the most significant design variables. The employed routines as well as the various interactions between the two softwares are illustrated with Fig. 3.6.

The performed sensitivity analysis is basically a Taylor approximation around the initial input configuration of the system. The influences of the system variables on the function are given by the first order derivatives and the interactions among them are the derivatives with respect to the different variables.

Say the considered system is described by a function f, which relates the design variables $x_1^*, \ldots, x_d^*$ to an output y.

The second order Taylor approximation for a function with two design variables x_1^*, x_2^* with the center of approximation at x_{1m}^*, x_{2m}^* is given by:

$$\begin{aligned} y(x_1^*, x_2^*) = f(x_{1m}^*, x_{2m}^*) &+ f_{x_1^*}(x_1^* - x_{1m}^*) \\ &+ f_{x_2^*}(x_2^* - x_{2m}^*) + f_{x_1^* x_2^*}(x_1^* - x_{1m}^*)(x_2^* - x_{2m}^*) \\ &+ f_{x_1^* x_1^*}(x_1^* - x_{1m}^*)^2 + f_{x_2^* x_2^*}(x_2^* - x_{2m}^*)^2 \end{aligned} \tag{3.53}$$

In the sensitivity analysis we make a transformation of coordinates into the center of approximation (at $\bar{x}_m^*$) and normalize the coordinates with dx_i.

$$x_1 = \frac{x_1^* - x_{1m}^*}{dx_1} \tag{3.54}$$

$$x_2 = \frac{x_2^* - x_{2m}^*}{dx_2} \tag{3.55}$$

The variance of the input variable in the analysis, dx_i, we can choose freely. It is the average between the maximum and the minimum values for the design variables in the simulations and defines how close to the center we place the points for the approximation.

$$dx_i = \frac{x_{imax}^* - x_{imin}^*}{2} \tag{3.56}$$

Introducing the following definitions

$$a_0 = f(x^*_{1m}, x^*_{2m}) \tag{3.57}$$
$$a_1 = f_{x^*_1} dx_1 \tag{3.58}$$
$$a_2 = f_{x^*_2} dx_2 \tag{3.59}$$
$$a_{11} = f_{x^*_1 x^*_1} dx_1^2 \tag{3.60}$$
$$a_{12} = f_{x^*_1} f_{x^*_2} dx_1 dx_2 \tag{3.61}$$
$$a_{22} = f_{x^*_2 x^*_2} dx_2^2 \tag{3.62}$$
$$\tag{3.63}$$

we may write the response function based on the taylor approximation as:

$$y(\boldsymbol{x}) = a_0 + a_1 x_1 + a_2 x_2 + a_{11} x_1^2 + a_{12} x_1 x_2 + a_{22} x_2^2 \tag{3.64}$$

By extending this representation of the response function $y(\boldsymbol{x})$ to d design variables, (3.64) yields:

$$\begin{aligned} y(\boldsymbol{x}) = a_0 + \sum_{i=1}^{d} a_i x_i + \sum_{i=1,j=1}^{d} a_{ij} x_i x_j + \cdots \\ \sum_{i=1,j=1,k=1}^{d} a_{ijk} x_i x_j x_k + \cdots + a_{i\ldots d} x_i \ldots x_d \end{aligned} \tag{3.65}$$

The coefficients $a_0, a_1, \ldots$ shall be called the effects of the x_i factors. One makes the distinction between:

$\boldsymbol{a_0}$ constant effect (equal to the experiments mean),

$\boldsymbol{a_i}$ main effects,

$\boldsymbol{a_{ij}}$ effects of the first order interactions,

$\boldsymbol{a_{ijk}}$ effects of the second order interactions.

Effects of third or higher order interactions are generally not useful.

Equation (3.65) describes the so called response surface of the considered system. It is an approximation of its behaviour around the center of the approximation at $\bar{x}^*_m$. The goal of a sensitivity analysis is to determine the coefficients of this formula and by that to get quantitative values for the influence of the different parameters and of their interactions. After we have determined those coefficients we can use the formula to predict the response of the system

at points where no experiment was carried out. The precision of the approximation depends on the order of the approximation. Of course, the accuracy of the calculated results will increase the closer we get to the center of approximation. Beyond the study of the influence of the design variables we can use the response surface methodology to find a minimum or maximum of the response of our system. The coefficients indicate the direction of such maxima/minima and we can change the design variables accordingly. Because too big changes may give wrong results (because it is a local approximation), we have to apply small changes and carry out new approximations at the new input configurations. Like this we will find an optimum after several iterations. Nevertheless, it can happen that the maxima/minima found with the help of this method are only local maxima/minima of the response of the system. If this happens we have to restart the iteration at a new point, that is, a new input configuration.

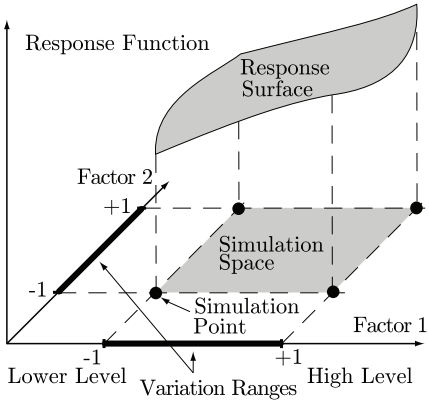

Figure 3.7. *Response surface analysis illustrated for two factors.*

The relation of simulation space and the response surface is illustrated in Fig. 3.7 in the case of two design variables. A response surface design according to Doehlert reduces the number of simulations to be executed in comparison to factorial or composite designs. With d design variables, $n = d(d+1)+1$ simulations must be executed. In matrix notation, which is best adapted for the use with Matlab and Ansys, the matrix of simulations $\mathbf{E}$ for n simulations is

given by:

$$\mathbf{E} = \begin{pmatrix} x_{11} & x_{12} & \cdots & x_{1d} \\ x_{21} & x_{22} & \cdots & x_{2d} \\ \vdots & \vdots & \vdots & \vdots \\ x_{n1} & x_{n2} & \cdots & x_{nd} \end{pmatrix} \tag{3.66}$$

Transformed into the absolute coordinate system, where x_{im} are the mean values of the design variables i at the center of approximation:

$$\mathbf{E}^* = \begin{pmatrix} x_{11} & x_{12} & \cdots & x_{1d} \\ x_{21} & x_{22} & \cdots & x_{2d} \\ \vdots & \vdots & \vdots & \vdots \\ x_{n1} & x_{n2} & \cdots & x_{nd} \end{pmatrix} \begin{pmatrix} dx_1 & 0 & \cdots & 0 \\ 0 & dx_2 & \cdots & 0 \\ \vdots & \vdots & \vdots & \vdots \\ 0 & 0 & \cdots & dx_d \end{pmatrix} \tag{3.67}$$

$$+ \begin{pmatrix} x_{1m} & x_{2m} & \cdots & x_{dm} \\ x_{1m} & x_{2m} & \cdots & x_{dm} \\ \vdots & \vdots & \vdots & \vdots \\ x_{1m} & x_{2m} & \cdots & x_{dm} \end{pmatrix} \tag{3.68}$$

Hence we can write the model matrix $\mathbf{X}$ as:

$$\mathbf{X} = \begin{pmatrix} 1 & x_{11} & x_{12} & \cdots & x_{11}x_{11} & x_{11}x_{12} & \cdots & x_{11}x_{11}x_{11} & \cdots \\ 1 & x_{21} & x_{22} & \cdots & x_{21}x_{21} & x_{21}x_{22} & \cdots & x_{22}x_{22}x_{22} & \cdots \\ \vdots & \vdots & \vdots & \vdots & \vdots & \vdots & \vdots & \vdots & \vdots \\ 1 & x_{n1} & x_{n2} & \cdots & x_{n1}x_1 & x_{n1}x_{n2} & \cdots & x_{n2}x_{n2}x_{n2} & \cdots \end{pmatrix} \tag{3.69}$$

With the vector of coefficients

$$\mathbf{A} = \begin{pmatrix} a_0 & a_1 & a_2 & \cdots & a_{11} & a_{12} & \cdots & a_{111} & \cdots \end{pmatrix}^T \tag{3.70}$$

the response function (Equation (3.65)) for n simulations is written in the following form:

$$\boldsymbol{Y} = \boldsymbol{X}\boldsymbol{A} \tag{3.71}$$

The simulation matrix has the elements x_{ij}. The x_{ij} are the simulation value x_j of the simulation i.

With the response vector $\mathbf{Y}$ obtained from FEM simulation, the coefficients are calculated:

$$\mathbf{A} = (\mathbf{X}^T\mathbf{X})^{-1}\mathbf{X}^T\mathbf{Y} \tag{3.72}$$

3.5.4 FEM Optimisation

Topology optimisation of piezoelectric actuators was investigated with the conclusion that the efficiency improvements were not justifying the far more complex fabrication of the non-standard topologies [191]. Promising for piezoelectric actuators, thinfilm applications and microfabrication in general, the method is not applicable to PUM at the current stage of research [22].

Therefore, because original research on the subject of topology optimisation is beyond the frame of this dissertation, a FEM optimisation algorithm implemented in Ansys is used to maximise the displacement of the stator by geometric optimisation in accordance with the geometry defined for preoptimisation.

The FEM optimisation using the Ansys optimisation module involves several steps. First, an analysis file to be used during looping must be created. It builds the model parametrically, obtains the solution, and retrieves and assigns the response quantities that are used as state variables and objective function to the parameters. Finally, the design variables and the objective function must be declared and the optimisation method must be defined.

The design variables are the variables that are modified during the optimisation process. They are selected out of the input variables used in the sensitivity analysis. The calculation time increases strongly with the number of design variables. Hence, we select the significant input variables as design variables and drop the insignificant ones. As we have seen in Section 3.5.3, due to a judicious sensitivity analysis, the fact of using only a restricted set of design variables does not influence the optimisation results. As Ansys minimises the objective function and we are searching for the maximum, the negative displacement is used as objective function. The first order method is used while choosing the default values provided by Ansys for the line search step size and the forward difference for the gradient computation. The optimisation is run in batch mode for efficiency reasons.

The first order method converts the optimisation problem to an unconstrained one by adding penalty functions to the objective function. It uses gradients of the dependent variables with respect to the design variables. For each iteration, gradient computations are performed in order to determine a search direction, and a line search strategy is adopted to minimise the unconstrained problem. This results in several analysis loops for each optimisation iteration. The optimisation

loop terminates when the change in objective function either from the best design to the current design or from the previous design to the current design is less than the objective function tolerance. The tolerance is defined as 1 percent of the current value, which is the Ansys default. Moreover, the maximum number of iterations is fixed in order to terminate the optimisation loop when none of both above-mentioned terminal conditions is reached.

Because the first order method, if the starting points of the design variables are not chosen appropriately, presents the risk of finding local minima of the objective function instead of the global minimum, the optimisation results are verified with the subproblem approximation method.

Further information on the particularities of the first order optimisation method implemented in Ansys is available in the theory reference for ANSYS and ANSYS Workbench [3]. Sections 6.5.1 presents an experimental validation of the optimisation methodology.

CHAPTER 4

Drive Electronics

Contents

4.1 Introduction

Along with sensorless control methods, optimally designed drive electronics are of significant importance when searching to increase efficiency of a mechatronic system. A generally accepted method for the design of motor drive electronics is the numerical simulation of the electronic circuitry with PSpice. To be able to do this, we need a load model, which translates to represent the piezoelectric motor by an electric equivalent model. In addition to the electric equivalent representation of the piezoelectric coupling, the mechanical load will be integrated in the electric equivalent model, which will in this way represent the complete driver-motor system. After recalling the drive requirements, a review of the literature on piezoelectric motor drivers is done. It shall give an overview on the most common approaches and state their respective advantages and inconveniences. On this basis, three concepts, a piezoelectric transformer based driver, as well as LC and LLCC resonant converters are evaluated in more detail. A full analytical model of the electronics-motor system may prove useful for design and control. But only if, for the first case, precision is high enough, and, additionaly, for the latter case, the model is simple enough to permit real time control. Both challenges were met up to some extend, but with important restrictions. Murphy in the case of a piezoelectric stack transducer uses a complete transducer model to compute the electric impedance over a large frequency range [136]. On the one hand, this model is not easily extendable to other motor configurations than stack actuators. On the other hand, we do not necessarily need a model for a large frequency range, but an accurate model valid around resonance. Nakagawa [137], Maas [128], Bullo [18], Giraud [59], McFarland [70] and others did not suggest a model based control for industrial use, but rather for laboratory experiments. These analysis and design models are therefore not useful for the indirect position detection objective. Hence, we rely on the equivalent electric circuit methodology adapted from electro-acoustics [173] succesfully applied to some extend [147] [122] [99] and extended in Section 4.2 in sight of design for self-sensing.

4.1.1 Drive Requirements

PUM are nowadays established as an alternative to electromagnetic drives in particular niche markets. The predominance of small motors and the main application field being mobile devices, the motors we focus on in this work must be supplied from battery or energy harvesters. Depending on the application the available voltage of such power sources ranges from 3 V to 10 V DC and peak currents should be kept below 100mA. Furthermore, the piezoelectric ultrasonic motors dedicated to these application fields operate in the 100 kHz frequecy

range. This implies some constraints on the drive electronics with respect to time constants. In order to reduce stress in the piezoelectric element to increase its longevity on the one hand and reduce losses on the other hand, the harmonics of the drive signal should be suppressed. In other terms, a pure sine wave should be used to supply the piezoelectric ultrsonic motor.

4.2 Electric Equivalent Circuit

The replacement of the mechanical branch by its electric equivalent in the representation of Fig. 4.1 will lead to the electric equivalent circuit representation of the piezoelectric coupling as shown in Fig. 4.2.

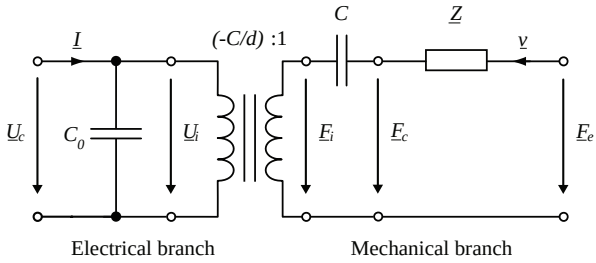

Figure 4.1. *Caracteristic circuit model*

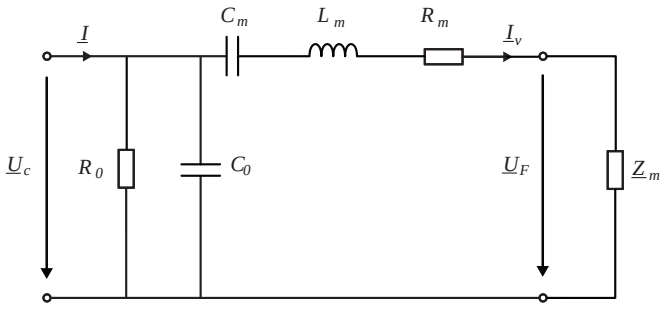

Figure 4.2. *Electric equivalent circuit of the motor*

C_0 is the static capacitor and C_m represents the equivalent compliance of

the piezoelectric resonantor and is defined in (3.29). R_0 displays the dielectric losses in the piezoelectric element. The equivalent inductance

$$L_m = m_e \left(\frac{d}{C_0'} \right)^2 \tag{4.1}$$

is an image of the vibrating active mass. It is found via the kinetic energy. Reasoning with the example of the piezoelectric plate (Fig. 3.3), with $b + \xi \cong b$ along the z-axis and supposing the mass homogeneously distributed along b. Then, the kinetic energy stocked in the element dz of z is

$$dE_c = \frac{mv(z)^2}{2b} dz \tag{4.2}$$

where $v(z) = \frac{zv}{b}$. Integration yields the total kinetic energy

$$E_c = \int_0^b dE_c = \frac{1}{2} \frac{m}{3} v^2. \tag{4.3}$$

Hence, $m_e = \frac{m}{3}$.

$\underline{Z_m}$ represents the electric equivalent of the mechanical impedance in contact with the piezoelectric element. It represents generally the mobile part of the motor.

Some authors [179], [214] suggest to introduce losses into the equivalent circuit model as shown in Fig. 4.3a. R_F and C_r are an equivalent representation of the slip phenomenon between the stator and the rotor, R_r models mechanical losses resulting from the movement of the rotor, and R_L is the equivalent load.

Two main reservations lead to the conclusion that for the present application such a detailed model is inadequate. First, no reliable identification method for all of the parameters representing the different loss factors is available. Second, comparison of both, the simple model developed here and the model of Sashida with approximate loss factors shows that around resonance where the model is valid, the difference is too small in order to justify the considerably increased complexity of the model. Similarly, a cascaded multimode electric equivalent model (Fig. 4.3b) is not useful, as we cosider only the variations of frequency characteristics strictly around the selected resonance frequency.

Plotting admittance and phase of the input impedance of the electric equivalent circuits illustrates the close match of the complex and simple models around resonance (Fig. 4.4). The motional admittance model of Fig. 4.2 and the cascaded circuit model of Fig. 4.3b are compared to a static model where the PUM

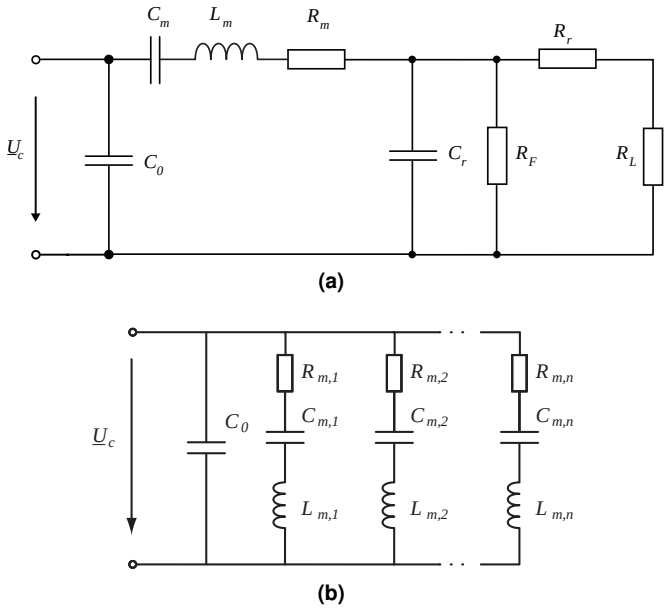

Figure 4.3. *Equivalent electric models taking into account a) losses and b) multiple modes*

is modelled simply by its static capacitance C_0. The numerical values of the shown example with resonance frequency at $385\,kHz$ and the corresponding matching circuit are given in Tables 4.1 and 4.2, respectively.

4.3 Resonance Matching and Oscillation Condition

The motional capacitance C_m and motional inductance L_m in the electric equivalent circuit represent stiffness and the inertia of the vibrator, respectively. The mechanical losses of the vibrator are modelled with R_m.

The sharpness of the resonance is indicated by the quality factor Q_m:

$$Q_m = \frac{1}{\omega_m C_m R_m} \tag{4.4}$$

Using the mechanical quality factor, we may define a figure of merit M_p

Table 4.1. *Numerical values of the evaluated motor models*

	Cascaded circuit model					
Parameter	$R_{m,1}$	$L_{m,1}$	$C_{m,1}$	$R_{m,2}$	$L_{m,2}$	$C_{m,2}$
Value	2500 Ω	137 mH	3 pF	1950 Ω	100 mH	2 pF
Parameter	$R_{m,3}$	$L_{m,3}$	$C_{m,3}$	$R_{m,4}$	$L_{m,4}$	$C_{m,4}$
Value	2500 Ω	30 mH	5 pF	2800 Ω	90.9 mH	1 pF
	Motional admittance				Static Capacitor	
Parameter	R_m	L_m	C_m		C_0	
Value	97.1048 Ω	5.11 mH	32.9 pF		557 pF	

Table 4.2. *Numerical values of the evaluated motor models*

Parameter	R_s	L_s	C_s	L_p
Value	20 Ω	0.3 mH	560 pF	0.3 mH

defining the ratio of consumed reactive power to active power useful for motion:

$$M_p = Q_m \frac{C_m}{C_0} = \frac{1}{\omega_m R_m C_0} \tag{4.5}$$

For optimal power transfer, the motional admittance Y_m of the excited system must equal the electric admittance Y. This translates to matching the electrical resonance frequency to the mechanical resonance frequency of the ultrasonic motor.

The motional admittance in terms of the (4.4) yields:

$$\underline{Y}_m = \frac{1}{R_m(1 + jQ_m(\frac{\omega}{\omega_m} - \frac{\omega_m}{\omega}))} \tag{4.6}$$

where the dissonance between the mechanical resonance and the excitation is expressed with $\frac{\omega}{\omega_m} - \frac{\omega_m}{\omega}$.

Using this expression, the total admittance seen by the supply when considering the static capacitance of the piezoelectric vibrator C_0 can be approximated

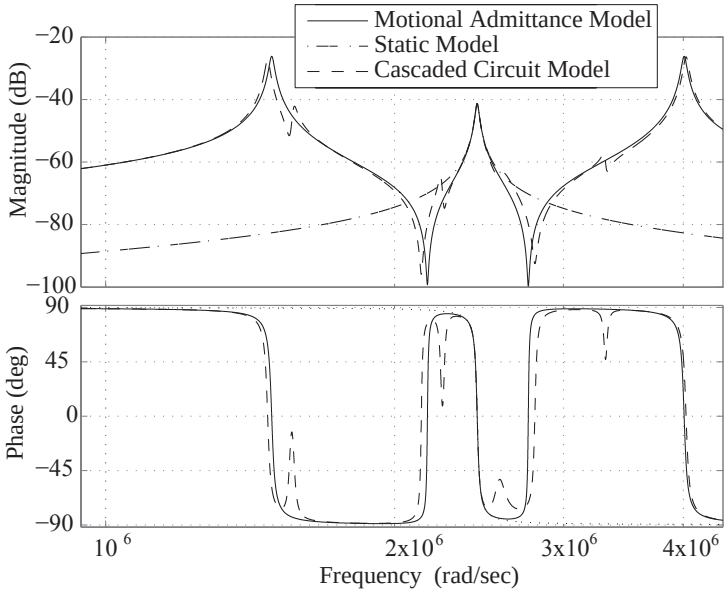

Figure 4.4. *Comparison of the cascaded model implementing parasitic modes, the model implementing a single motional branch and the simplified model only implementing the static capacitance.*

around resonance as:

$$\underline{Y} = \underline{Y}_0 + \underline{Y}_m = j\omega C_0 + \frac{1}{R_m(1 + jQ_m(\frac{\omega}{\omega_m} - \frac{\omega_m}{\omega}))} \tag{4.7}$$

The admittance magnitude maximum at the mechanical resonance frequency is slightly shifted with respect to the first zero crossing of admittance phase at serial resonance ω_s. Similarly, antiresonance, where the admittance magnitude is minimal, does not coincide with the second zero crossing at parallel resonance ω_p. This situation is well illustrated by the off-centred unity circle in the admittance locus in Fig. 4.5.

For a given frequency, which is in our case the mechanical resonance frequency where vibration amplitude is maximal, this effect of the static capacitor

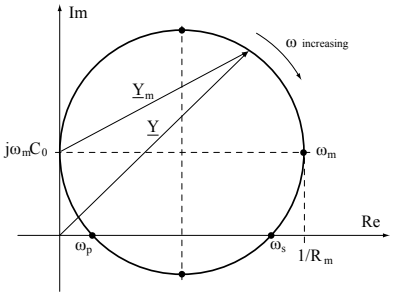

Figure 4.5. *Admittance locus of the piezoelectric element*

can be compensated by an inductor L_p in parallel to C_0:

$$L_p = \frac{1}{\omega_m^2 C_0} \tag{4.8}$$

This inductor consumes the reactive component of the current and hence the corresponding unity circle in the admittance locus is centered at the real axis. The mechanical resonance frequency f_m and the series resonance f_s are thus equal in the ideal case of perfect matching. The parallel resonance f_p disappears [147].

With these definitions the conditions for oscillation can be stated according to the general oscillator theory [26]:

1. Amplitude condition: The loop gain must be equal to or greater than 1
2. Phase condition: The loop phase must be zero (or equal to an integer multiple of 2π).

For design purposes, the phase condition may be expressed in terms of the electric equivalence. As aforementioned, the admittance locus must cross the real axis. With the imaginary coordinate of its center given as $\omega_m C_0$ and its radius $1/2R_m$, this condition yields:

$$\omega_m C_0 \leq \frac{1}{2R_m} \tag{4.9}$$

In terms of the figure of merit (4.5) the oscillation condition is $M_p \geq 2$.

4.4 State of the Art

A variety of driving principles for piezoelectric motors exists, most having in common a method to increase the voltage amplitude of a high frequency supply signal.

4.4.1 Linear Amplifier

The drive electronics play a key role for maximum performance of piezoelectric nanopositioning stages, tip-tilt mirrors and actuators. Ultra low noise, high stability servo controllers and linear amplifiers are essential there, because piezoelectric actuators respond to even microvolt changes of the control voltage with motion [31]. The high intrinsic losses of amplifiers operating as variable resistors, however, make such configurations little attractive for ultrasonic piezoelectric motors, where the negative influence of a small amount of total harmonic distortion on operation is not detectable and its effect on longevity is neglectable.

4.4.2 Switching Amplifier

Having excluded linear amplifiers, we will hence rely on some sort of switching amplifier to generate the high frequency drive signal in the range of hundert to several hundreds of kHz. A multitude of concepts and analysis are found in literature, among which the most relevant are listed in Fig. 4.6 [33] [98] [115] [116] [114] [223] [225] [150].

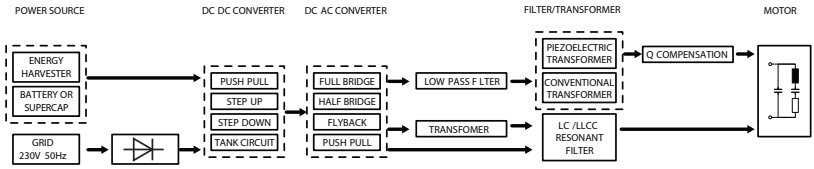

Figure 4.6. *Driver configurations using switching amplifier.*

Particular developments include self-adjusting power sources [9], [10] and energy feedback configurations (Fig. 4.7 [123]).

Due to their oversize, they are however not suited for mobile and other applications where available space is restricted and weight must be minimal. For the same reason, half-bridge configurations are prefered instead of full-bridges and no electromagnetic transformer can be used.

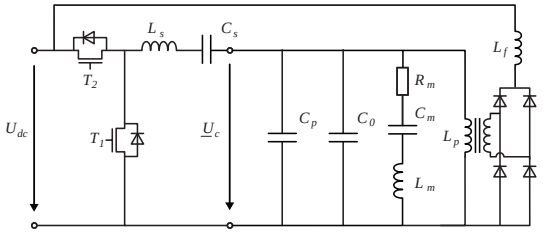

Figure 4.7. *Resonant converter with energy feedback*

4.4.3 Piezoelectric Transformer

Although the concept of a power transformer based on mechanical vibrations instead of electric fields was introduced by Rosen in the fifties [172], suitable materials only appeared in the eighties [38] and widespread application of the technology started with LCD backlighting in the ninetees of the last century [102]. Piezoelectric transformers have then been used to realise power converters of very high efficiency [117]. Fundamental limits on energy transfer were investigated [51], [100] and optimal working point tracking operation allows for maximising efficiency [119]. High power implementations are investigated [160]. An in-depth state of the art on piezoelectric transformer technology is beyond the scope of this work and can be found in [81]. Currently, two configurations have found widespread application, IHB and CLE inverters [236].

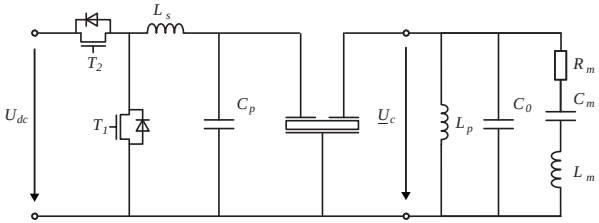

Figure 4.8. *Converter using a piezoelectric transformer to supply the voltage U_c to the piezoelectric motor*

When used as step-up converter, an additional switching stage (half-bridge) is necessary, which cancels out somewhat the efficiency gain of the drive system in the case of ultrasonic motors, adds additional components and cost. Much more interesting would be to combine the piezoelectric transformer with the

motor in order to transform directly the drive voltage to the needed amplitude [104], [132]. Two concerns appear with such a configuration (Fig. 4.8): First, the transformer must be able to transmit the necessary power to the motor, and second, the resonance frequency of both must be very close. While recent PT reach 97% efficiency up to 40 W output power, this is only true at a very narrow frequency range around resonance . Hence, not only should motor and transformer have the same resonance frequency, but also, the drift with temperature must be of the same order. The generally employed solution for the temperature drift problem is a PLL phase controller to track resonance frequency and hence the optimal working point [118]. More impeding is even the fact, that no straight forward solution exists for compensating the drift in motor resonance frequency depending on the applied load. Considering these arguments, the piezoelectric transformers are not yet an alternative to conventional step-up converters in motor drive applications, but remain mainly bounded to the backlight power supply and active damping [23] application.

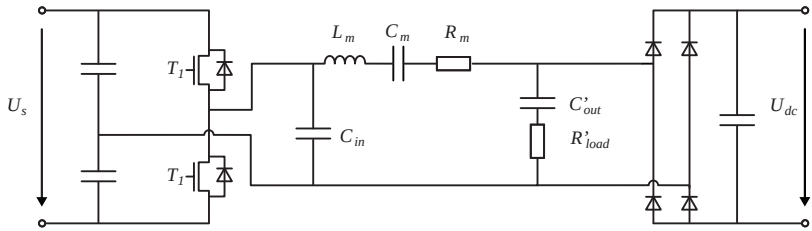

Figure 4.9. *Piezoelectric step-up converter. The piezoelectric transformer is represented by its electric equivalent circuit [94]*

Packaging of piezoelectric transformers is a major challenge and curbs the rapid commercialisation of more general purpose devices. The vibrations of the transformer must not be damped, else the efficiency decreases harshly. A good thermal transfer must be enabled, too. The only way, therefore, to package the device is to grasp it exactly at the nodes of the mechanical displacement. For this reason, some authors suggest to excite the second harmonic instead of the fundamental in order to duplicate the nodal points. In this way, however, the maximal performance potential of the PT is not exploited [94]. Current developments include design optimisation [44], [75], [210] as well as lead free technologies [64],[121].

4.4.4 Resonant Converters

Resonant converters refer to power converters featuring an output filter matching the mechanical resonance frequency of the piezoelectric load. Figures 4.10 and 4.11 illustrate the LLCC and LC configurations, respectively.

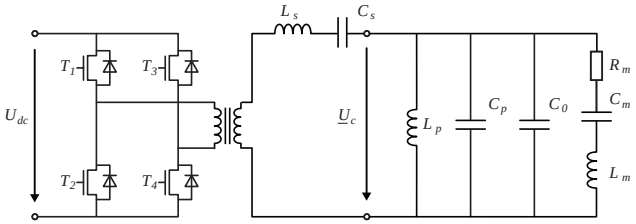

Figure 4.10. *Full bridge LLCC converter with transformer*

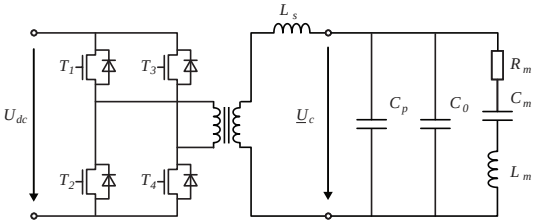

Figure 4.11. *Full bridge LC converter with transformer*

Similarly, both configurations are possible without transformer, as well as in a half bridge implementation [97].

4.5 Drive Electronics Design

For every element of the drive circuit, the optimal configuration must be found:

- DC-DC converter or power transformer
- Switching amplifier
- Resonance matching circuit

This choice depends on the motor as well as its application. At this evaluation stage of the design process, the requirements are not yet sufficiently well defined to be able to deduce valid constraints. Therefore, a rough selection is done, mainly based on the drive for miniaturisation. A step-up DC-DC converter is used to provide the high level voltage of the half-bridge resonant converter.

4.5.1 Resonant Converter Selection

According to the input stage, providing a direct current or a constant voltage, current source inverters (CSI) and voltage source inverters (VSI) are discerned. Contrary to the linear amplifiers, switching amplifiers operate theoretically without losses. The bridge transistors operate as switches instead of being used as variable resistances. In this way square waves are generated at the output. Ideally, implementing so called soft switching where the switch state is reversed exactly at zero voltage drop across the transistor, voltage is null during the conducting state and current is null during the open state. Real power losses are therefore mainly induced by the non-zero resistance of the transistor during the conducting state. Efficiency around 95% are reached for piezoelectric loads [1]. Both, LC and LLCC configurations are designed in order to be evaluated experimentally. During the design process, two different models of the piezoelectric load are used for each of the two configurations. The purpose of this approach is to evaluate the reduction in simulation time due to a simplified model and at the same time to verify if the consequent loss in precision is acceptable.

4.5.2 LC Resonant Converter

The piezoelectric capacitor C_0 varies during motor operation causing the output filter to get out of tune. In order to reduce this effect, a parallel capacitor C_p may be placed in parallel to the motor as shown in Fig. 4.12 [97].

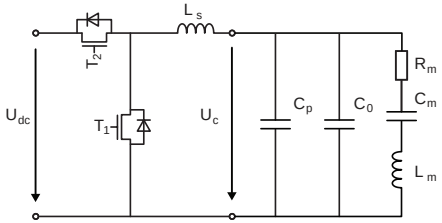

Figure 4.12. *Half bridge LC converter without transformer*

Matching the LC filter resonance frequency ω_f exactly to the mechanical resonance frequency of the motor (ω_m) is not advisable, because of the instability of a driver matched exactly to the motor resonance. Therefore, the filter is tuned to somewhat above mechanical resonance and the relative resonance frequency ω_r is introduced

$$\omega_r = \frac{\omega_m}{\omega_f} < 1. \tag{4.10}$$

The frequency of the signal applied to the system shall be noted as ω_s.
With

$$\omega_m = \frac{1}{\sqrt{L_m C_m}} \tag{4.11}$$

and

$$\omega_f = \frac{1}{\sqrt{L_s(C_0 + C_p)}} \tag{4.12}$$

the self inductor matching the filter to mechanical resonance is found by

$$L_s = \frac{L_m C_m}{C_0 + C_p} \tag{4.13}$$

With the input impedance

$$\underline{Z}_i = j\omega_s L_s + \frac{1}{j\omega_s C_s} + \frac{1}{Y_p} \tag{4.14}$$

where the parallel admittance

$$\underline{Y}_p = j\omega_s(C_0 + C_p) + \frac{1}{Z_m} \tag{4.15}$$

with the motional impedance

$$\underline{Z}_m = R_m + j\omega_s L_m + \frac{1}{j\omega_s C_m} \tag{4.16}$$

the transfer function of this configuration writes

$$\underline{G}_{LC}(j\omega_s) = \frac{\underline{U}_c}{\underline{U}_i} = \frac{Z_m}{j\omega_s L_s \left(j\omega_s Z_m \left(C_0 + C_p\right) + 1\right) + Z_m} \tag{4.17}$$

In order to express $\underline{G}_{LC}$ in terms of M_p, adding the stabilising parallel capacitor C_p to the oscillatory figure of merit given in (4.5) yields:

$$M_p = Q_m \frac{C_m}{C_0 + C_p} = \frac{1}{\omega_m R_m (C_0 + C_p)} = \frac{\sqrt{C_m L_m}}{R_m (C_0 + C_p)} \tag{4.18}$$

The transfer function at resonance is given by

$$\underline{G}_{LC}(j\omega_m) = \frac{R_m}{j\omega_m L_s (j\omega_m R_m (C_0 + C_p) + 1) + R_m} \tag{4.19}$$

plugging L_s according to (4.13) yields

$$\underline{G}_{LC}(j\omega_m) = \frac{\omega_f^2}{j\omega_m \frac{1}{R_m (C_0 + C_p)} + (\omega_f^2 - \omega_m^2)} \tag{4.20}$$

and using (4.18):

$$\underline{G}_{LC}(j\omega_m) = \frac{\omega_f^2}{j\omega_m^2 M_p + (\omega_f^2 - \omega_m^2)} \tag{4.21}$$

With the magnitude

$$\|G_{LC}\| = \frac{\omega_f^2}{\sqrt{\omega_m^4 M_p^2 + (\omega_f^2 - \omega_m^2)^2}} \tag{4.22}$$

the value for M_p maximising the power factor is found:

$$M_p = \sqrt{1 - \left(\frac{\omega_f}{\omega_m}\right)^2} = \sqrt{1 - \omega_r^2} \tag{4.23}$$

Finally the optimal value for the parallel capacitor C_p can be derived:

$$C_p = C_0 \left(\frac{Q_m}{1 - \omega_r^2}\right) \tag{4.24}$$

where Q_m is the mechanical quality factor of the load given in (4.4).

4.5.3 LLCC Resonant Converter

As we have seen in Section 4.3, it is possible to compensate the reactive power drawn from the supply by the imaginary part of the current in the piezoelectric ceramic with a parallel inductor L_p. However, in order to be able to tune the resulting output filter to the mechanical resonance of the motor, we have to add a series capacitor C_s. Hence we obtain a fourth-order LLCC resonant converter (Fig. 4.13) having two resonance frequencies ω_{fs} and ω_{fp}. Such a configuration allows for stabilising the voltage gain for the varibale quality factor of the piezoelectric load as will be shown in this section. We are therefore able to overcome one of the major drawbacks of series resonant converters.

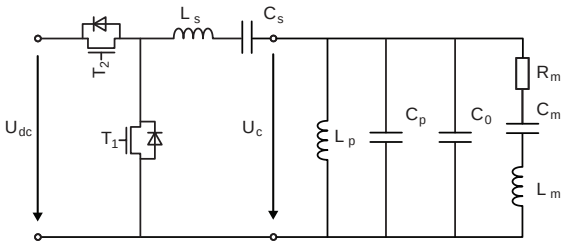

Figure 4.13. *Half bridge LLCC converter without transformer*

With the motional impedance

$$\underline{Z}_m = R_m + j\omega_s L_m + \frac{1}{j\omega_s C_m} \tag{4.25}$$

We find the parallel admittance

$$\underline{Y}_p = \frac{1}{j\omega_s L_p} + j\omega_s (C_0 + C_p) + \frac{1}{Z_m} \tag{4.26}$$

and adding the series tank the input impedance writes:

$$\underline{Z}_{\text{IN}} = j\omega_s L_s + \frac{1}{j\omega_s C_s} + \frac{1}{Y_p}. \tag{4.27}$$

We may now compute the transfer function of the LLCC filter with load:

$$\frac{1}{\underline{Z}_{\text{IN}} * \underline{Y}_p} = \frac{1}{\left(-\frac{j}{L_p\omega_s} + j(C_0+C_p)\omega_s + \frac{1}{R_m - \frac{j}{C_m\omega_s} + jL_m\omega_s}\right)} \cdot \frac{1}{\left(-\frac{j}{C_s\omega_s} + jL_s\omega_s + \frac{1}{-\frac{j}{L_p\omega_s} + j(C_0+C_p)\omega_s + \frac{1}{R_m - \frac{j}{C_m\omega_s} + jL_m\omega_s}}\right)} \tag{4.28}$$

In order to find the optimal excitation frequency, we consider first the LLCC filter only, while approximating the motor at resonance by its static capacitance C_0 in parallel with a resistor R_L representing the equivalent load of the motor [122]. The reactances of the serial and parallel branches of the filter write

$$\underline{X}_s = j\left(\omega_s L_s - \frac{1}{\omega_s C_s}\right) \tag{4.29}$$

and

$$\underline{X}_p = j\left(\frac{\omega_s L_p}{1-\omega_s^2 C_p L_p}\right), \tag{4.30}$$

respectively.

The transfer function $\underline{G}_{LLCC}$ of this approximation:

$$\underline{G}_{LLCC} = \frac{1}{1 + \frac{L_s - \frac{1}{C_s\omega_s^2}}{L_p} + (C_0+C_p)\left(\frac{1}{C_s} - L_s\omega_s^2\right) + j\left(\frac{L_s\omega_s}{R_L} - \frac{1}{C_s R_L \omega_s}\right)} \tag{4.31}$$

From the theory of complex numbers we find directly the phase

$$\underline{\phi}_{LLCC} = \arctan\left(\frac{\left(\frac{1}{C_s R_L \omega_s} - \frac{L_s\omega_s}{R_L}\right)}{1 + \frac{L_s - \frac{1}{C_s\omega_s^2}}{L_p} + (C_0+C_p)\left(\frac{1}{C_s} - L_s\omega_s^2\right)}\right) \tag{4.32}$$

The real part of the denominator of (4.31) being equal to zero at resonance,

$$0 = 1 + \frac{L_s - \frac{1}{C_s\omega_s^2}}{L_p} + (C_0+C_p)\left(\frac{1}{C_s} - L_s\omega_s^2\right) \tag{4.33}$$

the two positive solutions are approximately the filter resonance frequencies

$$\omega_{\text{fs}} = \left[\frac{K}{2} + \frac{1}{2}\sqrt{\left(K^2 - 4\frac{1}{L_s L_p C_s C_p}\right)}\right]^{1/2} \tag{4.34}$$

$$\omega_{\text{fp}} = \left[\frac{K}{2} - \frac{1}{2}\sqrt{\left(K^2 - 4\frac{1}{L_s L_p C_s C_p}\right)}\right]^{1/2} \tag{4.35}$$

where $\omega_{fs} < \omega_{fp}$ and

$$K = \frac{1}{C_p L_s}\left(1 + \frac{C_p}{C_s} + \frac{L_s}{L_p}\right). \tag{4.36}$$

The geometric frequency ω_g is then defined by:

$$\omega_g = \sqrt{\omega_{fs}\omega_{fp}} = \frac{1}{\sqrt{L_s C_s}} = \frac{1}{\sqrt{L_p(C_0 + C_p)}} \tag{4.37}$$

Designing the converter to be little dependant of the variations in the motional admittance, the quality factor Q_s relative to ω_{fs} should equal the quality factor Q_p realtive to ω_{fp}. Exploiting this property of the circuit, we can calculate the respective quality factors (cf. Fig. 4.14 [194]).

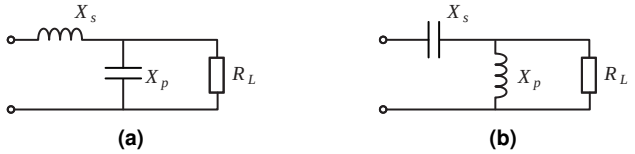

Figure 4.14. *Equivalent circuits of the LLCC resonant converter at a) $\omega_s = \omega_{fp}$ and b) $\omega_s = \omega_{fs}$*

For $\omega_s = \omega_{fp}$, X_p is capacitive and X_s inductive. By analogy, for $\omega_s = \omega_{fs}$, X_p is inductive and X_s capacitive. Hence, the quality factors become [194]:

$$Q_p = \frac{R_L}{\omega_{fp} L_s - \frac{1}{\omega_{fp} C_s}} \tag{4.38}$$

$$Q_s = \frac{R_L}{\frac{1}{\omega_{fs} C_s} - \omega_{fs} L_s} \tag{4.39}$$

From $Q_s = Q_p$ we find:

$$\frac{L_p}{L_s} = \frac{C_s}{C_p} \tag{4.40}$$

In terms of the quality factor (4.39), magnitude (4.31) and phase (4.32) become

$$\underline{G}_{LLCC} = \frac{1}{1 + \frac{L_s - \frac{1}{C_s \omega_s^2}}{L_p} + (C_0 + C_p)\left(\frac{1}{C_s} - L_s \omega_s^2\right) + j\frac{1}{Q_s}\left(\frac{L_s \omega_s - \frac{1}{C_s \omega_s}}{L_s \omega_{fs} - \frac{1}{C_s \omega_{fs}}}\right)} \tag{4.41}$$

$$\underline{\phi}_{LLCC} = \arctan\left(\frac{\left(\frac{1}{C_s \omega_s} - L_s \omega_s\right)}{Q_s\left(1 + \frac{L_s - \frac{1}{C_s \omega_s^2}}{L_p} + (C_0 + C_p)\left(\frac{1}{C_s} - L_s \omega_s^2\right)\right)\left(L_s \omega_{fs} - \frac{1}{C_s \omega_{fs}}\right)}\right) \tag{4.42}$$

respectively.

The PUM must be driven at the geometric frequency ω_g (4.37). This because, if $\omega_s = \omega_g$, the imaginary part of the denominator of (4.42) becomes zero and the real part equals 1. This means that a variation of the quality factor does theoretically not influence the voltage gain at ω_g. Similarly, with this condition, phase equals zero without being influenced by variations of Q. This behaviour, where the magnitude variation is very small, is illustrated in Figures 4.15 and 4.16 for $\omega_g = 2.44 Mrad/s$, the case of the resonant converter designed for the rotary PUM.

Beyond the assumption that harmonics suppression leads to lower stress in the piezoelectric stator, a detailed stress analysis was not performed, but may be found in literature [2].

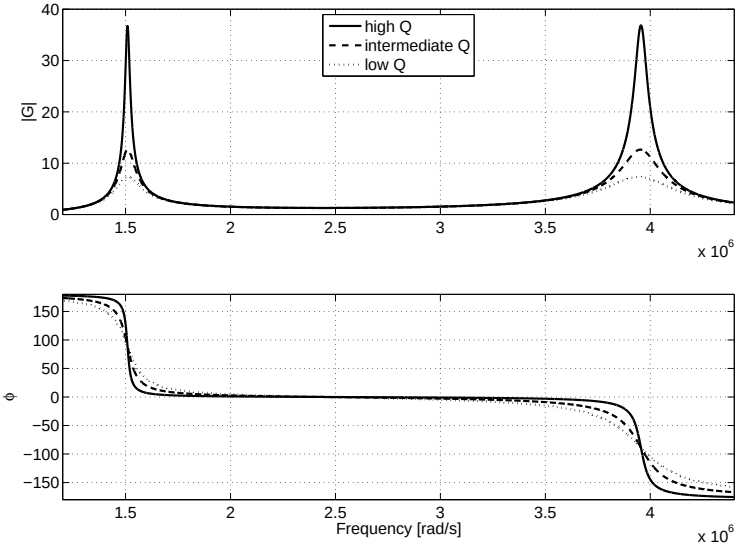

(a)

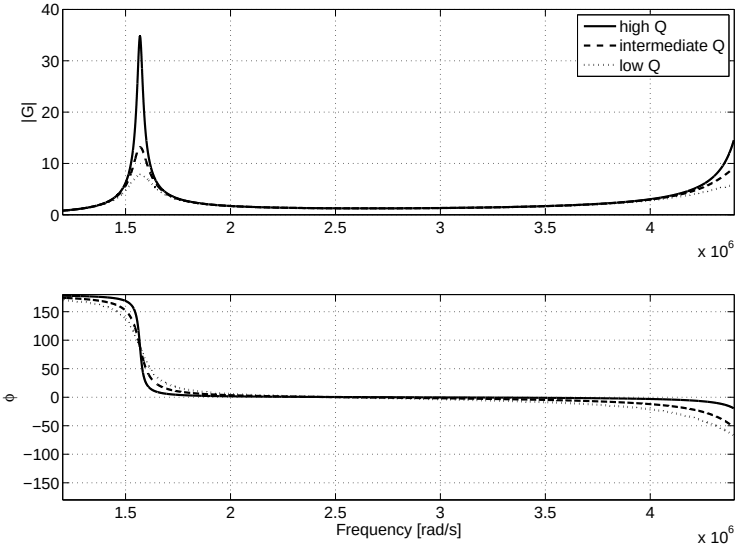

(b)

Figure 4.15. *Transfer characteristics for a) different quality factors; b) biased piezoelectric capacitance.*

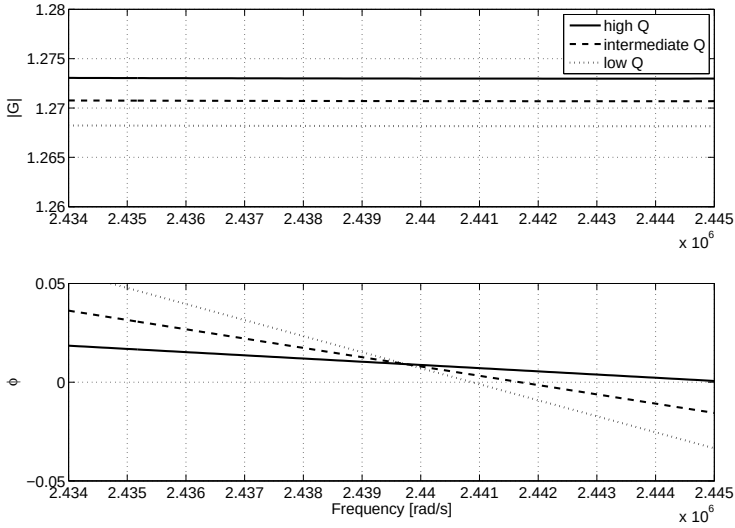

Figure 4.16. *Gain and phase variations of the real LLCC converter*

4.5.4 Comparison of the Converter Topologies

The better performance of the LLCC converter, compensating effectively the capacitive load and therefore suppressing the reactive power component is obtained at the cost of an additional inductor (Figures 4.17 and 4.18).

On the one hand it is true that because of the slightly lower power drawn from the source, the inductors L_s and L_p of the LLCC configuration may also be smaller than the series inductor L_s in the LC configuration. However, at this stage of research, no final decision should be taken, because first weighting factor must be introduced among the different constraints (size, efficiency, cost, allowable total harmonic distortion, stability, etc.).

4.6 Summary

This chapter introduced resonant converter concepts for PUM and the tools for resonance matching were made available. It has been shown, that piezoelectric transformers, despite the technology relationship, are useful to drive PUM only in very specific applications.

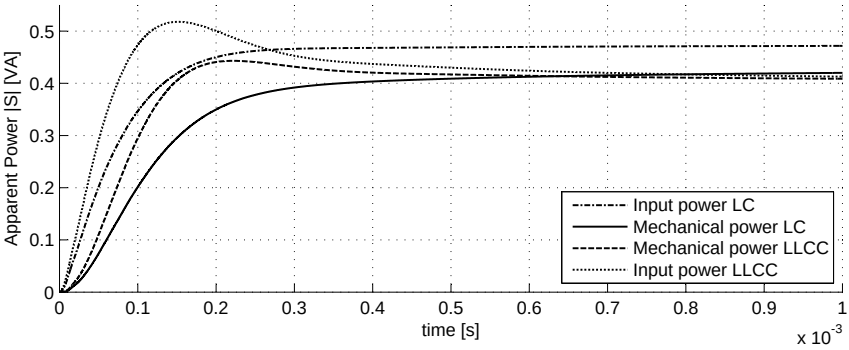

Figure 4.17. *Comparison of input power and mechanical power (full-bridge converter)*

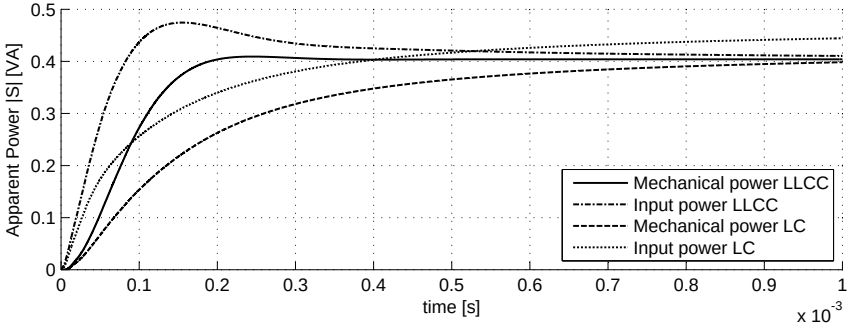

Figure 4.18. *Comparison of input power and mechanical power (half-bridge converter)*

CHAPTER 5

Sensorless Control

Contents

5.1 Objectives

Two control levels are necessary for efficient and save operation of the piezoelectric ultrasonic motor. An *inner control loop* regulates the drive frequency in order to track the working point where efficiency is maximised. Thereupon, an *outer control loop* uses sensorless or self-sensing control methods which deliver position or speed feedback. After a discussion of prior art, a selection of inner and outer control strategies will be evaluated in detail. Table 5.1 gives an overview on the techniques treated in this Chapter.

5.2 Literature Review

5.2.1 Piezoelectric Ultrasonic Motor Control

Research on piezoelectric motor control has been a very animated research field since the introduction of the traveling wave motor, hence for about the last thirty years. Important to the success of the traveling wave motor was to master its variable frequency characteristics. A frequency tracking controller does this [85]. Here, only the main subsequent achievements are listed:

- In 1990 a load-adaptive frequency tracking control implementation for ultrasonic motors driven by two-phase resonant converters was proposed [54], [55]. Most of later research on the subject refers to the suggested methods (Fig. 5.1).
- Speed tracking servo control systems combined phase and amplitude control techniques in order to reduce the influence of load variations [89].
- Adjustable speed control of ultrasonic motors by adaptive control strategies allowed to follow more precisely the varying motor characteristics [187].
- Artificial neural networks helped to further improve the adaptive controllers [184].
- Model reference adaptive control with dead-zone compensation was used to reduce the effects of the non-linear drive characteristics [183].
- An important criterion is also to drive the ultrasonic motor at its optimal working point in order to reach maxmium efficiency [188].
- Recently, a multitude of advanced neural controllers are presented for identification and speed control of PUM [233].

- Finally, another important issue is sensor failure. A way to deal with this problem are robust controllers [13], [62], [224], [14].

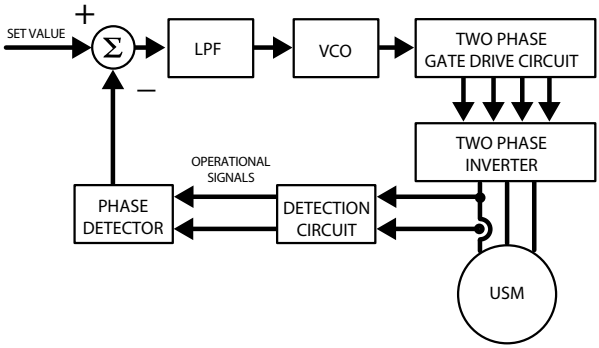

Figure 5.1. *Sensorless frequency tracking control of piezoelectric motors [55]*

5.2.2 Sensorless Speed Control

Sensorless speed control of PUM using neural networks was proposed in [190]. In the suggested method, a three-layer NN is used with offline training. The drive frequency, the RMS input voltage, and the surface temperature of the PUM are used as the inputs to the NN for speed estimation. The use of a neural network to identify nonlinear characteristics is very useful because of its nonlinear identification ability. However, this method presents some drawbacks when applied to position sensorless control, since speed integration contains an integral error that affects position estimation. A similar principle, but in a more general formulation, is addressed in [5]. Along with these efforts, a large variety of different sensorless speed controllers are known. Speed observers in combination with a position sensor [226], speed and possibly force sensing using a master-slave motor configuration [78], or using voltage look-up tables [72] are some of them. Because our main objective is position control, these methods are not further discussed here.

5.2.3 Sensorless Position Control

Three fundamentally different principles for detecting rotor position without a direct position sensor are found in literature:

- Interpretation of indirect measurements, for instance based on empiric motor models, mainly using artificial neural networks (ANN)

- Design for self-sensing of the PUM in order to produce position information in the drive signals

- Indirect position detection with integrated sensing elements such as piezoelectric stress sensors.

Stepper Motor

A first concept for sensorless position control proposed in 1990 was actually inspired by reluctance stepper motors in open-loop operation [213]. Similarly to the latter ones, this PUM motor uses standing waves designed such as that the driving members are not in continuous operation any more, but in contact to the rotor only for one step. At each step, a notch interrupts transmission of the active member's motion and the supply must be switched to the next consecutive member in order to shift the standing wave and resume operation. Taking the example of a rotary motor (Fig. 5.2), this working principle enables a priori position control at approximately continuous motion. However, the motor must be over engineered, motor performance is degraded by this special design and efficiency is low.

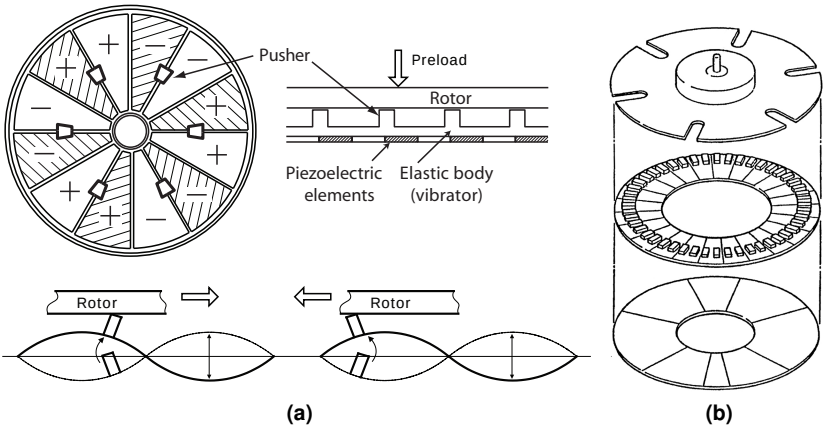

Figure 5.2. *a) Principle of the standing wave motor; b) Stepper motor*

Integrated Sensors

Inspired from vibration sensors used in structural analysis, piezoelectric thin film sensors on a cylinder surface were modelled [20], [11]. Such sensors may be integrated on a cylindrical motor in order to sense the vibration mode and hence motor velocity based on a observer [237].

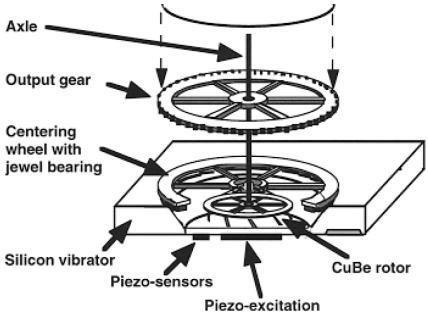

Figure 5.3. *Integrated piezoelectric stress sensor for position detection of an elastic force motor [165]*

Using integrated piezoelectric stress sensors that detect position by measuring the stress induced by the elastic fins of an elastic force motor (Fig. 5.3) is another intermediate solution. The sensing element is economic and does not consume power, but adds additional steps to the fabbrication process [164]. Moreover, the method is applicable only to a small range of PUM.

Online observation of electric signals

Indirect position detection based on the electric signals, which are usually phase voltage and current or charge, is generally implemented according to the block diagram shown in Fig. 5.4.

A method to estimate the rotor position of a piezoelectric actuator on the basis of phase voltage and the charge on the surface of the piezoelectric element is suggested in [56]. However, the addressed principles are not valid as is for PUM, where motion is generated by frictional coupling.

Position sensorless control for piezoelectric motors based on input voltage information only was suggested in [189], a collaboration between Meidensha Corporation and the Ryukyus University. The authors claim to observe an important position-dependant variation in the phase voltage of the motor, but do not specify enough details for that the experiments could be repeated.

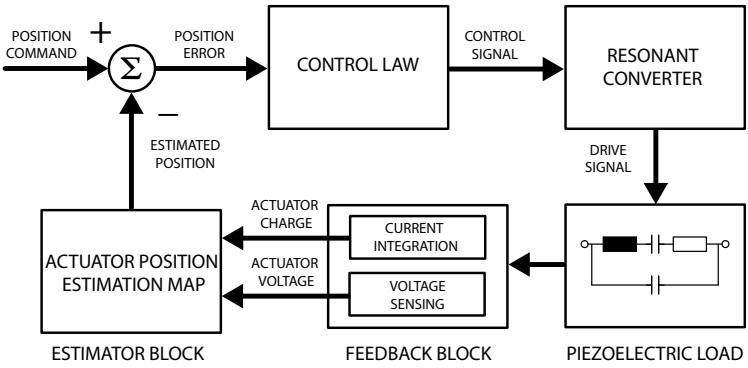

Figure 5.4. *Basic constituents of a sensorless position controller*

Design for Self-Sensing

In view of the drawbacks encountered with stepper motors and indirect piezoelectric sensors, [147] suggested an indirect position sensor based on angular modulation of the motional admittance. The method intends to obtain the same position information as the aforementioned approaches without compromising the motor performance. The method was first proposed for indirect position detection of a piezoelectric wrist watch motor and feasiblity tests were presented.

For the reliable operation of the motor, the stator must be excited close to the resonance frequency of its fundamental mode. This is ensured by a phase-locked loop (PLL) controller. With this configuration, the excitation frequency follows the variations of the motors electric characteristics due to load and temperature variations. In the case of an indirect position sensor, where the resonance is modified as a function of rotor position, there are different approaches suggested to detect the induced frequency variations:

- Comparison to a stable reference frequency
- Measurement with a frequency-to-voltage converter
- Measuring the time of a period, inversion
- Measuring the number of periods in a detection window

The limitations imposed by analog control techniques in this work may be overcome at least to some extend by digital control.

Table 5.1. *Overview on sensorless control strategies considered in this Chapter: Implemented methods are mentioned in bold face with reference to the respective section.*

	Inner control Loop: Optimal working point tracking			Outer control loop: Position control
Digital Control	Amplitude feedback	Phase voltage		**OEM compatible** Section 5.4.4
		Phase current		
		Transmitted power (MPPT) Section 5.3.3		Stepper motor
		Auxiliary voltage	Free phase (if available)	
			Isolated electrode portions	**Design for self-sensing** Section 5.4.3
	Phase feedback	Auxiliary voltage	Free phase (if available)	
			Isolated electrode portions	Integrated Sensors
		Phase current (PLL) Section 5.3.4		
	Artificial neural network 5.4.4			Artificial neural network
Analog Control	Self-oscillating driver	Active filter		Frequency measurement
		Section 5.3.1		
		Switching amplifier	Voltage feedback	
			Current feedback	

5.3 Inner Control Loop: Optimal Working Point Tracking

In Chapter 4 we explained that the power which is transmitted to the motor maximises its effect when the electric resonance frequency of the system, which is predominantely determined by the inductance of the electronic circuit and the static capacitance of the piezoceramic element, is matched to the mechanical resonance of the motor. Therefore, the drive electronics will be tuned such that electric resonance of the overall system coincides with the mechanical resonance frequency of the PUM. This point assured, we are able to track mechanical resonance by measuring electric resonance. Two fundamentally different methods to track resonance are distinguished: The self-oscillating configuration on the one hand and a feedback controller on the other hand. The latter one may be realised using different feedback variables or sets among them.

5.3.1 Self-Oscillating PUM

Oscillators are exemplary components to generate the drive signal for the excitation of an ultrasonic device in general. One particular design are quartz oscillators, exploiting the very stable resonance characteristics of the crystal to output particularly precise and frequency stable signals. The self-oscillating motor refers to a setup where the piezoelectric stator is not only used to generate the mechanical vibration that induces continuous motion, but also as replacement for a quartz oscillator governing the excitation frequency [83]. In contrast to the quartz oscillator, the aim is not a stable signal, but a signal whose frequency follows the variations of the piezoelectric motor and therefore excites it always at resonance.

Active Filter

In a quartz oscillator one single resonance mode is favoured by appropriate cut, electrode design and packaging and the resonator is therefore oscillating spontaneously at the selected mode given the oscillation conditions hold. With a piezoelectric ceramic resonator, however, the selected mode is often not the one where motional admittance is maximal and the unsolicited modes must be filtered.

Such an implementation is found in [147]. Two linear amplifiers in serial connection with the piezoelectric motor constitute the oscillator. The first one is a non-linear block ascertains that the circuit starts to oscillate while compensating the variations of the motional resistance. The second one is an active filter supressing the parasite modes.

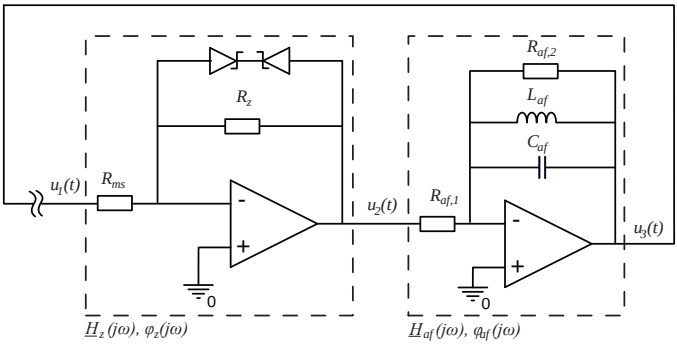

Figure 5.5. *Self-oscillating inner control loop [147]*

The open-loop transfer function is given by

$$\underline{H}(j\omega) = \underline{H}_z(j\omega) \cdot \underline{H}_{af}(j\omega) = \frac{\underline{U}_3}{\underline{U}_1} \tag{5.1}$$

Closing the feedback loop, $\underline{U}_3 = \underline{U}_1$:

$$\underline{H}(j\omega) = 1. \tag{5.2}$$

Applying the oscillation condition for phase (4.9) yields:

$$\phi = arg\underline{H}(j\omega) = \phi_1(\omega) + \phi_2(\omega) = 0 \tag{5.3}$$

The open-loop gain must exceed unity for oscillation to start and to compensate the motional resistance of the motor.

$$|\underline{H}(j\omega)| \geq = 1 \tag{5.4}$$

The phase condition is used to match the oscillation frequency to the selected mechanical resonance frequency. Because the non-linear block, assuming an ideal linear amplifier, has zero phase shift

$$\phi_1(\omega_m) = 0, \tag{5.5}$$

the filter block must not present any phase shift neither, which is the case only for

$$\omega_0 = \omega_m = \frac{1}{\sqrt{L_{af} C_{af}}}. \tag{5.6}$$

The head-to-tail mounted zener diodes with the resistor R_z limit the voltage amplitude of the oscillator at V_z. For $|v_2| < V_z$ the total loop gain at resonance is given by

$$|\underline{H}(j\omega_0)| = \frac{R_{af,2}}{R_{af,1}} \cdot \frac{R_z}{R_{ms}} \tag{5.7}$$

For the design of the filter, the following trade-off on its quality factor

$$Q_{af} = R_{af,2} \omega_0 C_{af} = \frac{R_{af,2}}{\omega_0 L_{af}} \tag{5.8}$$

must be fulfilled:

1. The loop gain must not exceed unity for the parasite modes whose admittance loci cross the real axis in the complex plane, hence Q_{af} must be maximised.
2. Because the mechanical resonance of the motor governs the oscillator, the filter quality factor must be in the same range as the motor quality factor, hence not too big.

Furthermore, the presented method is only valid for low power motors usually supplied by $1.5V$ as presented in [147] due to the inherently low efficiency of linear amplifiers. In order to maximise the efficiency of the self-oscillating PUM, it must be placed in the oscillator loop where electric energy is maximal.

Switching Amplifier

In order to exploit the potential of a piezoelectric motor operating at $20V$, $100mA$, therefore, the self-oscillating principle must be implemented with the switching amplifier as presented in Chapter 4. A possible configuration is shown in Fig. 5.6. Particular implementations of the method uses a free phase of the motor as feedback for the oscillator loop [198].

An oscillator circuit can also be realised with a switching amplifier [139], [193]. A LC series resonant circuit allows to select the modal frequency. The same conditions for loop gain and phase apply.

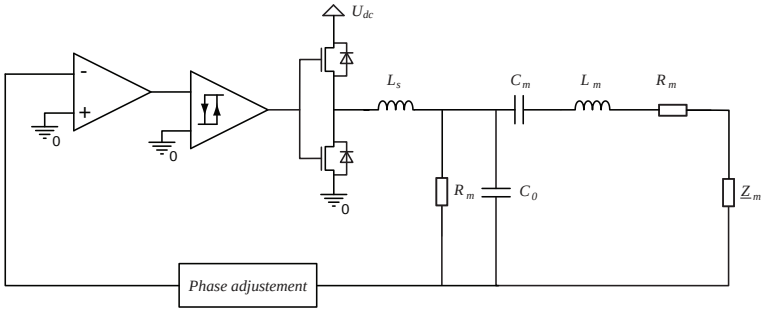

Figure 5.6. *Self-oscillating drive circuit with switching amplifier*

5.3.2 Closed-Loop Resonance Frequency Tracking

Amplitude Measurements

Phase voltage With an ideal voltage source, the phase voltage amplitude would remain stable with load variations and the consequent shift in resonance frequency. In reality, however, at resonance, the drive electronics have an internal resistance comparable to the series resistance of the piezoelectric ultrasonic motor, which varies with load. It is hence theoretically possible to control the excitation frequency by measuring the voltage drop across the motor.

Phase current At steady state, the current amplitude depends on the drive voltage amplitude and frequency [17]. Two working points are suggestive. First, current is maximal at resonance where admittance is maximal, maxima which coincides with the maximal vibration amplitude for the resonance matched drive circuit. Hence, this is the working point where the maximal effect is reached for a given supply voltage. Second, current is minimal at antiresonance where admittance is minimal, minimum which is tantamount to minimise losses in the piezoceramic.

Transmitted Power The variations in phase voltage being relatively small, its measurement alone is not promising for a frequency controller implementation. A target-aimed indicator is rather the maximal power transmitted to the piezoelectric motor by the drive electronics. It is obtained by four-quadrant multiplication of phase voltage and phase current. Adjusting the optimal working point by the means of MPPT is a widely known practice which is used mainly in solar power systems, asynchronous power generators [186] and wireless energy

transfer [58]. We evaluate if the principle applies to the case of driving a PUM, because, by definition maximal power is transmitted to the piezoelectric element at resonance where impedance is minimal. Basically, power point tracking may be implemented either in a continous way for analog control and with a discrete approach for digital control [12].

Auxiliary Voltage The direct piezoelectric effect is commonly used to design self-sensing piezoelectric actuators. Indeed, where an excitation signal is applied to the piezoelectric element to induce displacement by the converse piezoelectric effect, this very displacement engenders an electric potential by the direct piezoelectric effect. With piezoelectric ultrasonic motors, we can use this reasoning to track resonance. As we have seen, the displacement is maximal at resonance. Hence, by tracking the maximum of the voltage induced by the displacement, resonance can be tracked. In practice, an auxiliary piezoelectric element is used to sense the induced potential. The Shinsei traveling wave motor integrates a sensor element in the ring of active elements and single-mode standing wave actuators use the free electrode as feedback electrode. Other standing wave motors incorporate an isolated sensor portion in the electrode of the active element itself.

Limitations All the above mentioned amplitude measurements have in common that maxima or minima of the sensed variable must be controlled as a function of frequency. Hence, the corresponding function does not preserve its order over the frequency range in question, which results in a non-linear control law. A linearisation is possible for instance by limiting the permissible frequency range such that the amplitude variations are described by a monotonic function. Unless the expected variations are very slight, this approach is not feasible with a simple linear controller.

Phase Feedback

As can be seen easily in Fig. 5.7, the phase of the admittance and hence by definition the phase difference between supply voltage and motor phase current is a useful measure of the resonance frequency. At resonance, voltage and current are in phase, below resonance, current leads and above resonance, current lags. The shown admittance measurement is done at rest without load of a functional model with resonance frequency at 386.4 kHz.

Fig. 5.8 illustrates the case where the resonance frequency f_m is lower than it was at calibration (f_0). This occurs when temperature falls or load is smaller than the reference values at calibration. In Fig. 5.9 the opposite case is shown, which

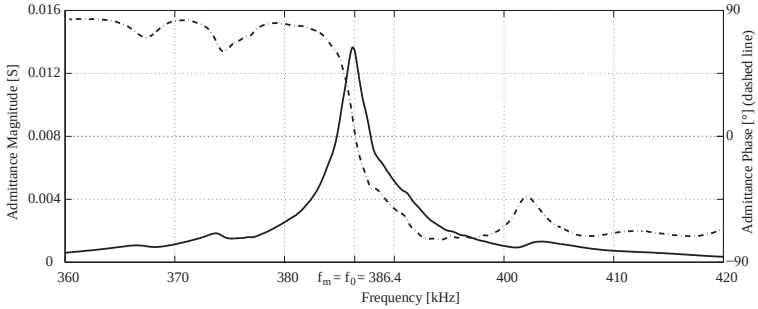

Figure 5.7. *Admittance measurement at rest without load*

occurs for instance when load is increased. We should note that such resonance frequency shifts are often a combination of different causes. The curves are drawn using the electric equivalent model as introduced in Chapter 3.

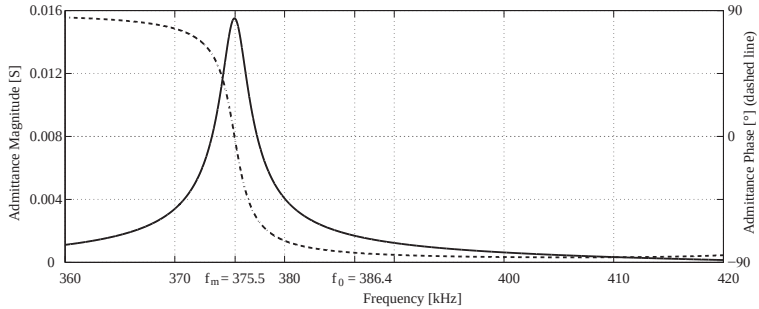

Figure 5.8. *Admittance simulation when the resonance frequency is decreased*

Phase differences, as well for phase current with respect to phase voltage as for auxiliary voltage to phase voltage, are monotonic functions of the excitation frequency around resonance. Therefore, in contrast to the amplitude measurements, a linear controller may be used for frequency tracking based on phase measurements.

Current Phase The phase shift of the line current with respect to the excitation voltage equals by definition the phase of the input admittance of the device to be

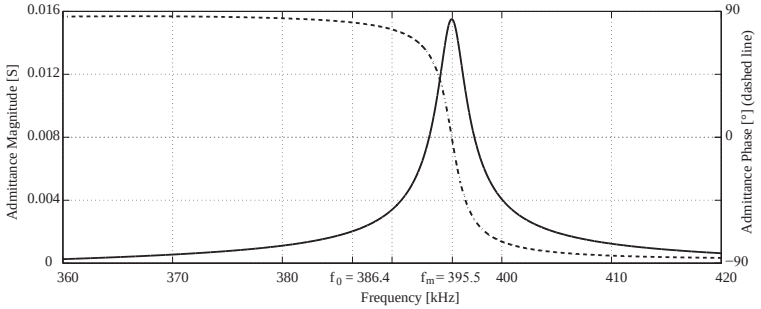

Figure 5.9. *Admittance simulation when resonance frequency is increased*

driven. With a resonance matched driver, current and voltage are in phase at resonance. Below resonance, current lead approaches $\pi/2$ and tends towards $-\pi/2$ above resonance. Within a control range that is restricted such that no parasitic modes intervene, no second zero crossing appears. The method is attractive as no additional electric connections are necessary and the phase can be measured easily.

Auxiliary Voltage Phase Depending on the configuration with and the position where the auxiliary voltage is measured, its phase difference with respect to the phase voltage is variable. Once the motor configuration fixed, it can be or predicted using analytical and numerical motor models or measured with an impedance analyser. The phase difference is contained between $-\pi/2$ and $\pi/2$ and depends on the excitation frequency. The method is only interesting for motor configurations where an existing free phase can be used and no additional sensor and electric connectivity are needed.

Synthesis

Two of the discussed optimal working point tracking methods are further evaluated. Firstly, a maximum power ponint tracking (MPPT) controller is suggested to control the power transmitted to the PUM, because it considers directly the issue of interest. In order to control the phase shift and hereby the frequency of the supply signal analogically, the phaselock loop concept is suited best [55]. Hence, secondly, a controller for tracking the current phase with a PLL is evaluated. In the case of a frequency matched drive design, it presents a simple indirect measurement of maximal efficiency.

5.3.3 MPPT Controller

Continuous Approach

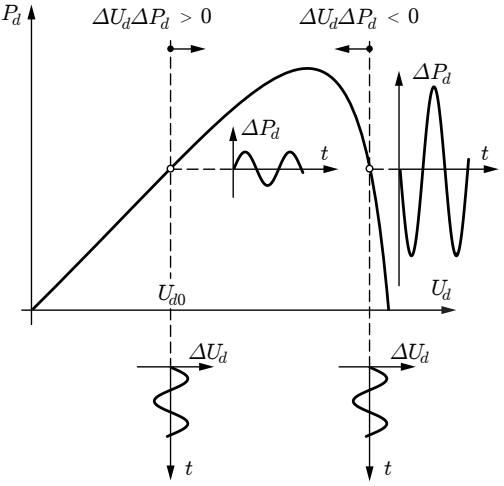

Figure 5.10. *Continuous MPPT*

Fig. 5.10 illustrates the continuous MPPT principle. The working frequency is generated by a voltage controlled oscillator. A periodic variation of ΔU_d is added to the constant VCO control voltage U_{d0}. The frequency of this variation is around 1kHz (well below the working frequency of around 400kHz and significantly higher than 50Hz), introducing a variation ΔP_d to the mean power P_d. At a frequency below the optimal working point, the product of ΔU_d and ΔP_d is positive ($\Delta U_d \Delta P_d > 0$). This is easily exploited to increase U_{d0} in order to reach the optimal working point. Contrarly, at a frequency above the optimal working point, $\Delta U_d \Delta P_d < 0$, which allows for reducing U_{d0} by the means of a control circuit. Finally, at the optimal working point, $\Delta U_d \Delta P_d \cong 0$ and U_{d0} is maintained. Hence this strategy is very appropriate for analog control.

A schematic representation of the controller is shown in Fig. 5.11. As described above, a periodic variation of ΔU_d is added to the standard VCO control voltage U_{d0}. The VCO output is fed to the piezoelectric element where phase current and voltage drop are measured. An analog four quadrant multiplicator calculates power from this data. A band pass Bessel filter cuts out the power variation corresponding to the perturbing signal and compares these two by the means of a XOR gate. A PI control is then used to adjust the VCO control value

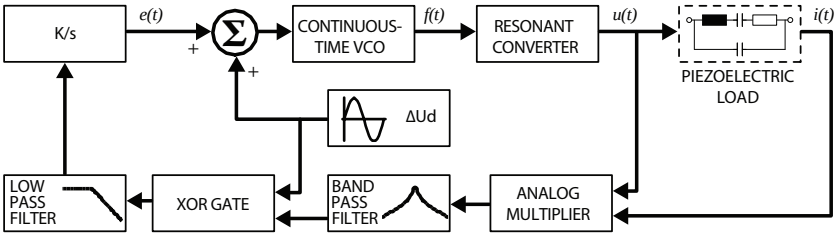

Figure 5.11. *Schematic representation of the analog MPPT controller*

in order to reach the optimal working point.

With the open-loop behaviour given in Figures 5.12-5.14, feeding the XOR output back to the VCO as shown in Fig. 5.11, the optimal working frequency will be reached in any case as illustrated with the closed loop results (Fig. 5.17).

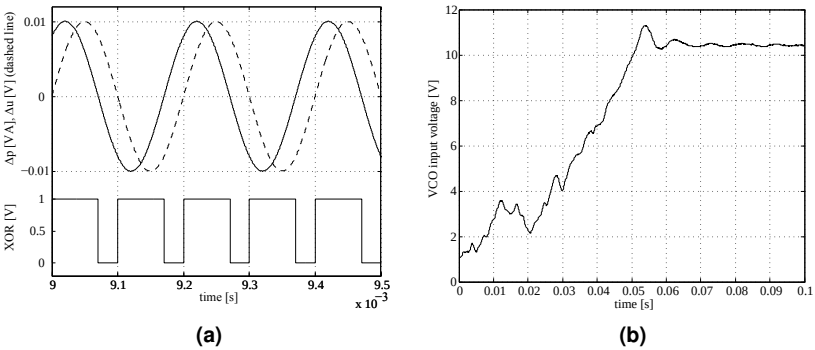

Figure 5.12. *a) Open-loop behaviour of the MPPT circuit: perturbing signal and observed power variation with the resulting XOR output signal at* $1/10$ *of the resonance frequency. Signals are in phase and the XOR output is high; b) Closed loop response of the MPPT circuit: starting voltage corresponding to a VCO output of* $1/10$ *of the resonance frequency.*

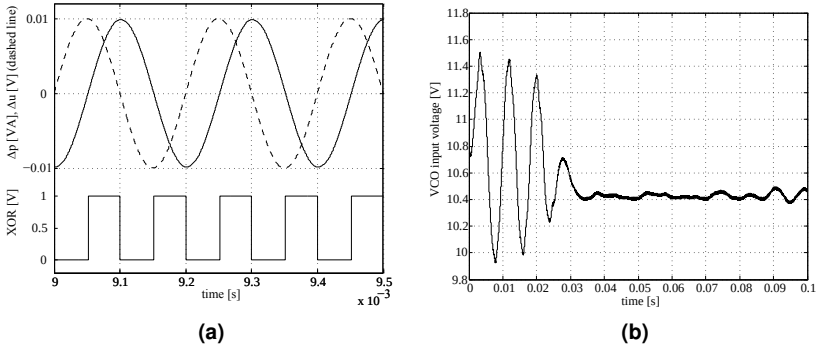

Figure 5.13. *a) Open-loop behaviour of the MPPT circuit: perturbing signal and observed power variation with the resulting XOR output signal at the resonance frequency. Power leads by $\pi/2$, the XOR output is a half duty cycle signal; b) Closed loop response of the MPPT circuit: starting voltage corresponding to a VCO output close to the resonance frequency.*

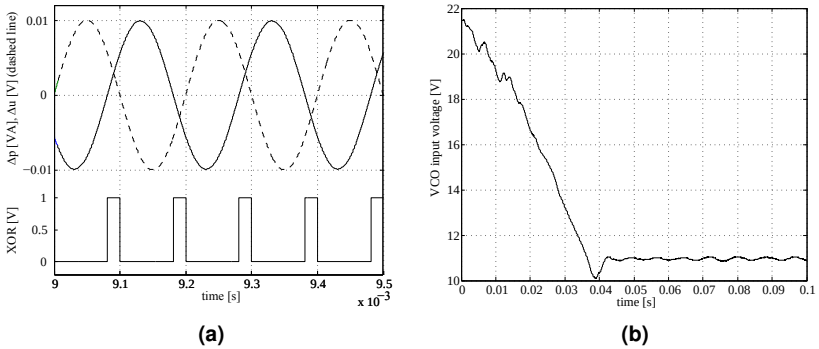

Figure 5.14. *a) Open-loop behaviour of the MPPT circuit: perturbing signal and observed power variation with the resulting XOR output signal at 2 times the resonance frequency. Phase shift is π, the XOR ouput is low; b) starting voltage corresponding to a VCO output of 2 times the resonance frequency.*

Discrete Approach

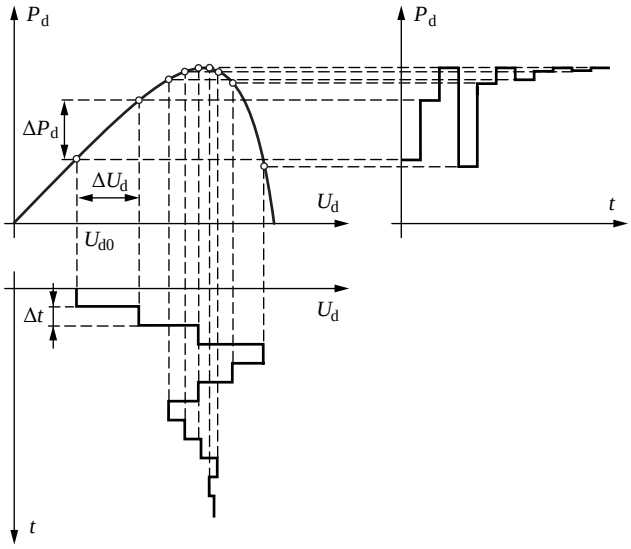

Figure 5.15. *Discrete MPPT*

For digital control, the strategy illustrated in Fig. 5.15 is preferrable. Starting from an initial working point U_{d0}, the DC voltage U_d is increased by a relatively large voltage step ΔU_d. Then, the power P_d is measured. If the difference ΔP_d between the new and the preceeding value is positive, U_d is increased again by the same voltage step ΔU_d. If, contrarly, $\Delta P_d < 0$, the variation direction is inverted and the voltage step is divided by 2, hence decreasing U_d by $\Delta U_d/2$. After a settling time, the optimal U_d will be reached.

Hence, two samples of the transmitted power at different times $t_1 < t_2$ are compared: $\Delta P = P_2 - P_1$. If their difference is positive then the last step was towards the power maximum, if in contrary their difference is negative then the last step was away from the power maximum and the step needs to be inverted. Adaptive step sizing is used to minimise oscillation around the power maximum.

Synthesis

A block diagram of the implemented digital MPPT controller is given in Fig. 5.16. The transient response of the analog controller is given in Fig. 5.17. Rise time is above $9\,ms$ and settling time within a $\pm 100\,mV$ band for the VCO input

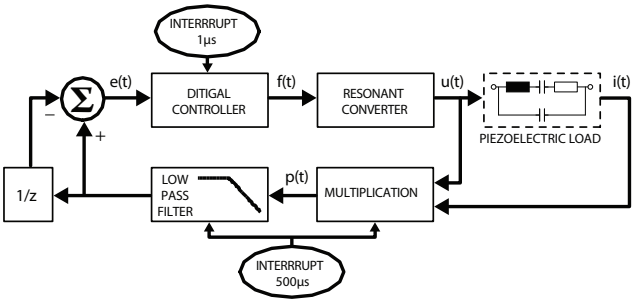

Figure 5.16. *Program layout of the digital MPPT controller*

is around $27\,ms$. This poor dynamic controller performance is not acceptable. The intrinsically non-linear controller in conjunction with digital filter design is unrewarding. Furthermore, in digital control, phase techniques are much more appropriate than amplitude measurements, where scaling problems, noise, and sampling issues are limiting factors.

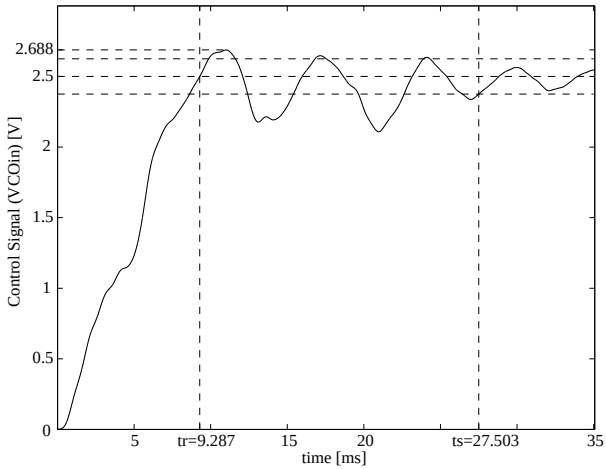

Figure 5.17. *Transient response of the MPPT controller*

5.3.4 Phaselock Techniques

This section will outline the working principle of the phaselock loop (PLL) for motor control applications and introduce the elements composing the PLL circuit. Design constraints will be addressed with focus on the analysis of stability for this type of control system. Finally, a PLL controller implemented with a standard component will validate the approach.

Definitions

PLL are in principle nonlinear time-varying systems. However, with either a large filter time constant or a narrow loop bandwidth as compared to the signal frequency, the average behavior over many cycles is approximately linear and time invariant. The detailed behaviour within a single cycle is of less concern in this case. Therefore, tools of linear analysis are valid and the PLL can be analysed by the means of Laplace transforms and the related transfer function concept. In ordinary electric circuits, a transfer function relates voltages or currents of the input and output signals. But in a PLL, the input or output variables of most interest are phases of the signals, not the amplitudes. The transfer functions considered here relate phase modulation of a signal applied in one location of the PLL to phase-modulation response in another location in the PLL [57].

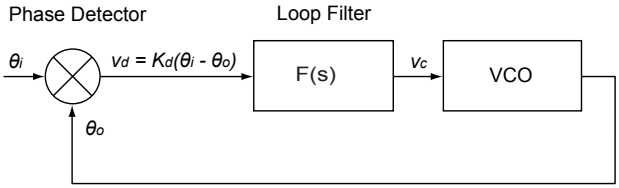

Figure 5.18. *The three main constituents of a PLL: Phase comparator, loop filter and VCO*

PLL for Frequency Tracking Control

From a control theory point of view the PLL is a feedback loop (Fig. 5.18) whose output is controlled by a reference signal. The feedback loop allows for comparing the output to this reference signal in order to adjust eventual errors.

For a PLL within its working range we can state:

- The output is the phase of an alternating signal θ_o

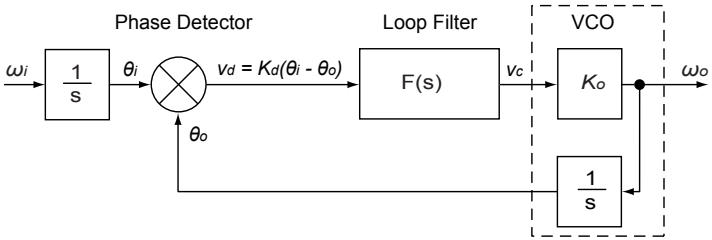

Figure 5.19. *The relation between phase and angular frequency allows for controlling the system in the frequency domain ($f = \frac{\omega}{2\pi}$)*

- The input is another alternating signal with phase θ_i
- The feedback loop compares the two phases θ_o and θ_i
- The output θ_o aligns to the input θ_i and phase error θ_e becomes ideally zero.
- The output frequency ω_o equals the input frequency ω_i.

For driving the piezoelectric motor, the configuration shown in Fig. 5.20 is introduced.

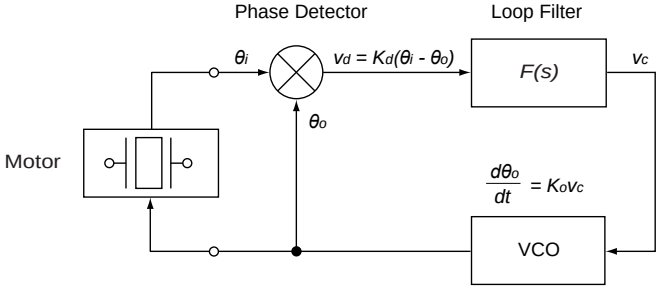

Figure 5.20. *Simplified block diagram of the PLL based circuitry driving a piezoelectric motor*

Voltage controlled oscillator

The voltage controlled oscillator (VCO), as its name says, outputs an alternating signal whose frequency is proportional to the dc voltage amplitude at its input. Most of implementations are based on the same working principle, which is basically charging and discharching a capacitor by the means of a current that is in

turn controlled by the input voltage. The output frequency of the VCO is proportional to the input voltage in a range called locking range. Within this span, the PLL is locked, its output frequency equals the input frequency. However, the capture range defined by the low-pass filter determines the frequency from which on the PLL is able to lock. Hence, the capture range is always smaller or equal to the locking range.

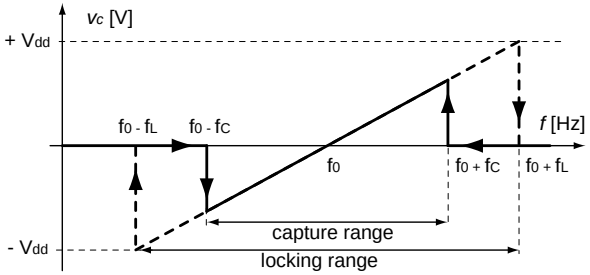

Figure 5.21. *VCO locking and capture ranges*

Transfer function The transfer function of the VCO is equal to its sensibility:

$$K_o = \frac{\Delta\omega}{\Delta v_d} = \frac{2\pi \cdot 2f_L}{2V_{dd}} \tag{5.9}$$

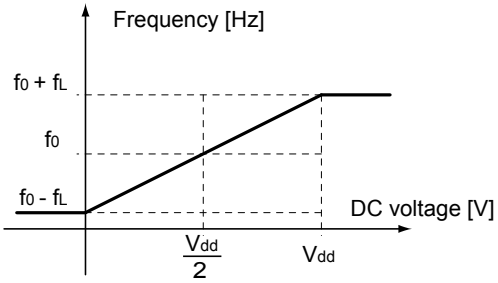

Figure 5.22. *VCO transfer function*

Phase detector

A phase detector compares the phase of two alternating signals and outputs a signal proportional to the phase shift between them. However, harmonic frequencies $n \times f_e$ appear as multiples of the input frequency f_e. Hence, the comparator output signal v_d is composed of its directly exploitable mean voltage and a multitude of harmonics which must be suppressed by a low-pass filter.

There are three ways to detect phase, namely:

- With a multiplyer circuit
- Using a XOR gate
- By the means of sequential devices

We use a phase-frequency detector for its ability to inambiguosly indicating phase differences from -2π to 2π.

Three-state phase-frequency detector While a XOR gate expects input signals with 50% duty cycle, a three-state phase-frequency detector does not work on the duty cycle, but on the rising edges of the input signals. Therefore, it is the natural choise for the motor control application, where variable environment and disturbances hinder an exact control of the duty cycle.

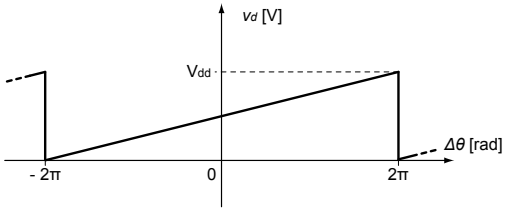

Figure 5.23. *Response characteristics of a phase-frequency three-state phase comparator*

The transfer function of the phase-frequency detector is given by its sensibility:

$$K_d = \frac{\Delta U}{\Delta \theta} = \frac{V_{dd}}{4\pi} \tag{5.10}$$

Loop filter

The main purpose of the loop filter is to establish the dynamic performance of the PLL. Furthermore, the filter cutoff frequency determines the capture range of the PLL. As a welcome side effect, the harmonics of the phase detector output signal and high frequency noise are eliminated.

To understand the design criteria introduced in this section, it must clearly be distinguish between the concepts of PLL order and PLL type. The order of the PLL is defined by the degree of the transfer functions characteristic polynomial $B(s)+A(s)$, whereas the type refers to the number of integrators in the feedback loop. The PLL order will have some influence on stability, while the PLL type influences crucially the control precision.

Since there will always be a VCO, which contributes in any case one integrator, a PLL is at least of type 1. Hence, the order of the loop filter defines the type of the PLL.

Transfer function analysis

Phase detector The phase detector (PD) output voltage is

$$v_d = K_d(\theta_i - \theta_o) = K_d\theta_e \tag{5.11}$$

where K_d is the phase-detector gain factor.

Loop filter The error voltage v_d is processed by the loop filter (LF), whose action is described in the frequency domain as

$$V_c(s) = F(s)V_d(s) \tag{5.12}$$

Voltage controlled oscillator The deviation of the voltage controlled oscillator (VCO) from its center frequency is $\Delta\omega = K_o v_c$, where K_o is the VCO gain factor. Since frequency is the derivative of phase, the VCO operation writes in the frequency domain as

$$\theta_o(s) = \frac{K_o V_c(s)}{s} \tag{5.13}$$

Combined transfer functions Combining the elements of the PLL we can write the overall loop transfer functions:

- Open-loop transfer function:

$$G(s) = \frac{\theta_o(s)}{\theta_e(s)} \tag{5.14}$$

- System transfer function:

$$H(s) = \frac{\theta_o(s)}{\theta_i(s)} = \frac{G(s)}{1 + G(s)} = \frac{K_d K_o F(s)}{s + K_d K_o F(s)} \tag{5.15}$$

- Error transfer function:

$$E(s) = \frac{\theta_e(s)}{\theta_i(s)} = \frac{1}{1 + G(s)} = \frac{s}{s + K_d K_o F(s)} \tag{5.16}$$

Phase Error

In order to understand how the PLL eliminates steady-state phase errors under variable frequency conditions, we have to evaluate the phase-error transfer function (5.16) with respect to the PLL type.

The steady-state phase errors are readily evaluated by means of the final-value theorem of Laplace transforms, which states that the steady-state value of a function in the time domain is determined from inspection of its transform in the tansform domain as follows [126]:

$$lim_{t\to\infty} y(t) = lim_{s\to 0} Y(s) \tag{5.17}$$

Application to the phase-error Equation 5.16 yields:

$$lim_{t\to\infty} \theta_e(t) = lim_{s\to 0} \frac{s^2 \theta_i(s)}{s + K_d K_o F(s)} \tag{5.18}$$

Phase offset There is no steady-state error resulting from a step change $\Delta\theta$ of input phase, as may be shown easily by substituting the Laplace transform of the input $\theta_i(s) = \Delta\theta/s$ into (5.18):

$$lim_{t\to\infty} \theta_e(t) = lim_{s\to 0} \frac{s\Delta\theta}{s + K_d K_o F(s)} = 0 \tag{5.19}$$

Frequency offset Since phase is the integral of frequency, a step change $\Delta\omega$ of input frequency manifests as input phase changing linearly with time $\theta_i(s) = \Delta\omega t$. Hence, substituting $\theta_i(s) = \Delta\omega/s^2$ into (5.18) yields the steady-state error for a step change of input frequency:

$$\theta_v = lim_{t\to\infty} \theta_e(t) = lim_{s\to 0} \frac{\Delta\omega}{s + K_d K_o F(s)} = \frac{\Delta\omega}{K_d K_o F(0)} \tag{5.20}$$

This static phase error, which may be written with the DC gain $K_{DC} = K_o K_d F(0)$ as

$$\theta_v = \frac{\Delta\omega}{K_{DC}} \tag{5.21}$$

is not acceptable for the present application. If anything, the main goal of piezoelectric motor control with a PLL is to eliminate the static phase error as fast as possible in order to match the VCO frequency to the resonance frequency of the piezoelectric actuator.

From the frequency offset equation (5.20) derives readily that

$$lim_{F(0)\to\infty}\theta_v = 0 \tag{5.22}$$

The goal of $F(0) = \infty$ is reached with an integrator in the loop filter, hence with a PLL of type 2.

Frequency ramp If input frequency is changing linearly with time at a rate of $\Lambda[rad/s^2]$, that is $\theta_i(t) = \Lambda t^2/2$, Laplace transformed phase is $\theta_i(s) = \Lambda/s^3$. Then, for a second order type 2 PLL, phase error may be written as

$$\theta_e(s) = \frac{s^2\theta_i(s)}{s^2 + sK_dK_oF(s)} \tag{5.23}$$

Applying the final-value theorem, the dynamic tracking error becomes apparent:

$$\theta_a = lim_{t\to\infty}\theta_e(t) = lim_{s\to 0}\frac{\Lambda}{s^2 + sK_dK_oF(s)} \cdot \frac{\Delta\omega}{s + K_dK_oF(0)}. \tag{5.24}$$

For θ_a to be zero it would be necessary that $F(s)$ had the form $Y(s)/s^2$, where $Y(0) \neq 0$. However, instead of using a loop filter with two cascaded integrators to reach this (which might introduce some annoyances at other points), we rather accept a control performance limited by the dynamic tracking error θ_a.

Stability Analysis

A control system is useful only when it is up to a certain extend insensitive to external factors, say stable. The Bode criterion of stability is useful to analyse the stability of a PLL based motor controller.

Loop parameters The transfer function in Equation 5.15 after replacing $F(s)$ for an adequate loop filter will contain numerous gains and time constants. Considering that only two poles and one zero are involved it is overdetermined. The transfer function of the second order type 2 PLL is specified by two loop parameters, the undamped natural frequency ω_n and damping ζ. With these loop parameters

$$\omega_n = \sqrt{\frac{K_d K_o}{\tau_1}}; \qquad \zeta = \frac{\tau_2}{2}\sqrt{\frac{K_d K_o}{\tau_1}} = \frac{\tau_2 \omega_n}{2} \tag{5.25}$$

where τ_1 and τ_2 are the time constants of the second order loop filter, the system transfer function rewrites as

$$H(s) = \frac{2\zeta\omega_n s + \omega_n^2}{s^2 + 2\zeta\omega_n s + \omega_n^2} \tag{5.26}$$

Damping ζ	$\frac{\omega_{gc}}{K}$	Phase Margin ϕ_M [deg]
0.5	1.27	51.8
0.707	1.10	65.6
1.0	1.03	76.4
2.0	1.002	86.4
5.0	1.00005	89.4

Table 5.2. *Relation of phase margin and damping in a PLL*

Stability Criterion A PLL will be stable if its phase lag at the gain crossover frequency ω_{gc} is less than $180°$:

$$Arg[G(j\omega_{gc})] > -\pi \tag{5.27}$$

Two restrictions apply:

1. The amplitude plot crosses 0 dB at only one frequency
2. The open-loop transfer function $G(s)$ is BIBO stable

The second condition is true if the system transfer function has no poles in the right-half plane. For a proof refer to e.g. Longchamp [126].

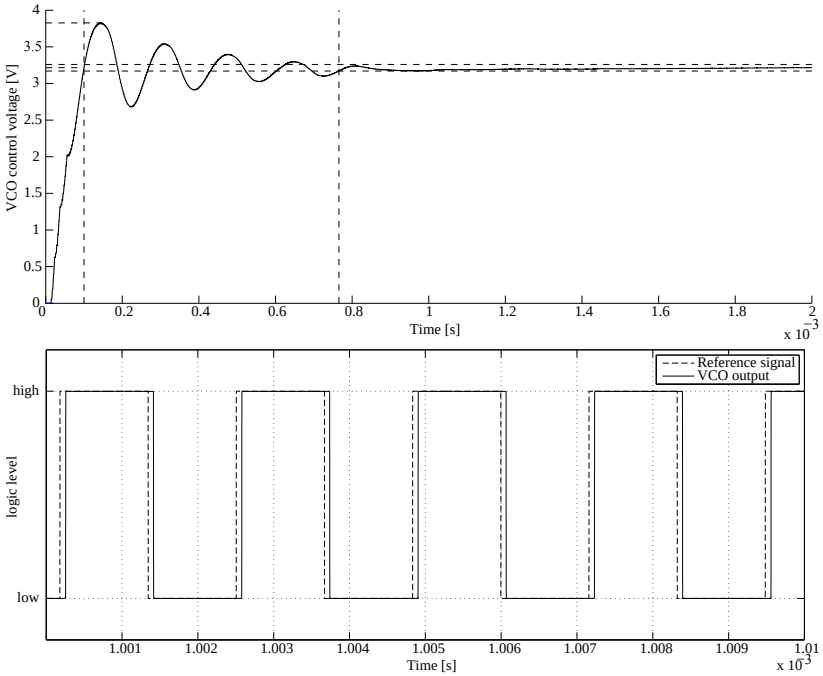

Figure 5.24. *Transient and steady state response of the simple PLL*

Stability margins The robustness of the PLL is given by its phase margin. This value is a measure for the loss of phase acceptable before crossing the limit of stability. Phase losses come either from phase noise or loop delays. The concept of phase margin derives from the stability criterion and is accordingly defined as

$$\Phi_M = Arg[G(j\omega_{gc})] + \pi \tag{5.28}$$

A PLL is hence stable if its phase margin is positive. However, it also gives a qualitative indication of the loop damping. From Table 5.2 we observe that:

- since $\zeta = 0.5$ is a rough lower bound on reasonable damping factor, a PLL should have a phase margin of at least $45°$, preferably more.
- With large damping, the phase margin approaches $90°$, a limit imposed by the presence of the pole at $s = 0$ inherent in the VCO.

Implementation of a 2^{nd} order type 2 PLL

According to the above considerations we design a PLL that tracks the resonance frequency of the piezoelectric load while accepting a dynamic tracking error θ_a. To design an appropriate loop filter the transfert function must be stated as a function of the filter time constant. Then, the loop filter is designed such that no poles of the system transfert function are in the right half plane. Then, having proved BIBO stability with zero or real negative poles, phase margin must be checked to be above $45°$.

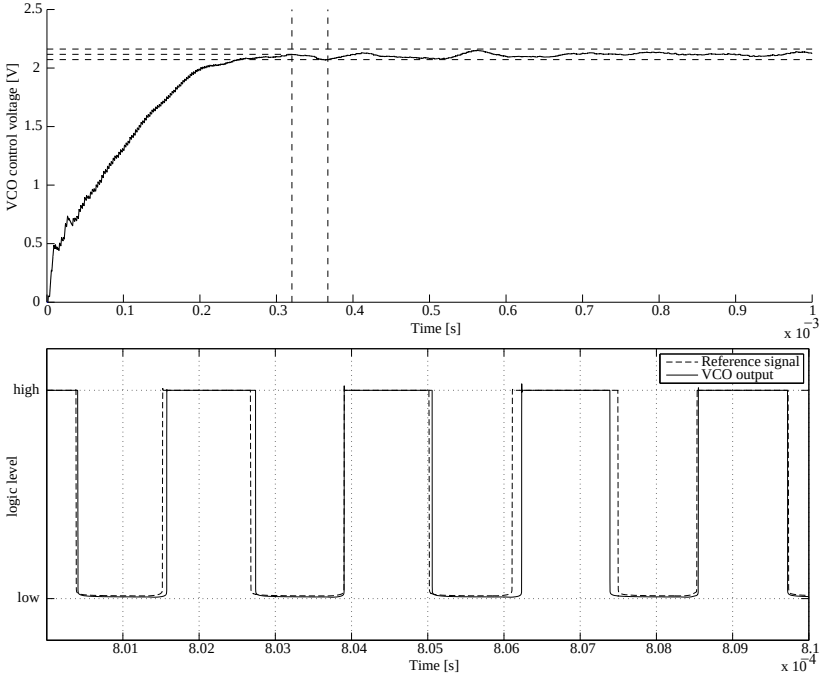

Figure 5.25. *Transient and steady state response of the PLL circuitry controlling the PUM drive frequency*

Spice simulation The PLL was evaluated without the piezoelectric load, simply matching the output to a reference signal. Fig. 5.24 shows the transient response of the VCO control voltage which is an image of the drive frequency and the steady state response of the VCO output compared to the reference signal.

Static phase error is eliminated and the dynamic phase error becomes apparent.

Based on the stability considerations an additional loop gain must be introduced when the PLL is used as optimal working point tracking controller. It was designed cancelling phase difference between phase voltage and current in accordance with the performance expectations for a type 2 PLL (Fig. 5.25). The reference signal is an image of the PUM phase current.

5.4 Outer Control Loop: Speed and Position

Reliability concerns, the strive for miniaturisation and cost issues are the main motivation to the replacement of direct position sensors in mechatronic systems. Nowadays, therefore, indirect position detection methods and position observers are good industry practice for many electromagnetic solutions, whereas research on the subject is only in its beginning in the field of piezoelectric motors. This section gives details on the researched methods.

5.4.1 Analytical Model Based Position Control

When the position is not directly measureable due to the above cited restrictions, we must identify measurable information that can be measured cheaper, with smaller sensors and more reliably. There are two distinct ways of doing so. Either, the motor must be designed in a way to deliver those information, or, even better, existing properties of phase voltage and phase current are identified to contain some information on the rotor position. With the first solution, which is also refered to as active method, the modifications of the phase currents will inevitably result in electric noise and in some cases also in a loss of performance [153]. The latter one, refered to as the passive method as no interference to the motor is done, uses signal processing algorithms such as the Kalman filter to identify the rotor position information contained in the drive signals. A Kalman filter minimises the estimation error for a linear system, but needs a fairly accurate system model in order to yield a succesful estimation.

The output characteristics of PUM are related to the drive signals by non-linear laws, due to the non-linear nature of the stator vibration, and because of the intermittent nature of the contact at the interface between stator and rotor. Furthermore, this contact involves complex tribological interactions, which are challenging to be described mathematically.

Recent modelling strategies aim for both, modelling the overall energy conversion mechanism of PUM from the application of voltage to the piezoelectric ceramic through to the rotation of the rotor, and validating their models and numerical results by experimention [137]. Work in this field encompasses both,

numerical [130] and analytical approaches [239]. A pathbreaking contribution by Hagood and McFarland in 1995 [70] used the Rayleigh-Ritz method for the dynamic response modelling of traveling wave ultrasonic motors. A review on these early serious models of PUM is given in [228]. Transient characteristics were later evaluated [209] and stick-slip models were introduced [61]. Simpler, though accurate approaches are obtained at the expense of neglecting again the transient phenomena [156]. Other important contributions are found in [65] [146] [69] [42] [157] [158] [159]. A particular approach, useful not only for optimisation, but also for controller simulation [93], used an equivalent electric representation in order to join the models of the individual system functions. Analytical model based controllers have been developed [127] [60] and contributed significally to the understanding of the phenomena involved in ultrasonic motor operation. However, the speed controllers resulting from such an approach are only interesting for laboratory use and industrialisation in the field of small motors fails because of the method's exorbitant complexity. Furthermore, none of the existing models does yet provide the tools for observer based position controllers [18].

Confronted to this situation we aim to research passive methods for detecting rotor position indirectly using empirical models which are linearised around the operation region of the motor (Section 5.4.2). Also, we investigate the feasibility of self-sensing methods which do not compromise the motor operation (Sections 5.4.3 and 5.4.4).

5.4.2 Artificial Neural Network Model Based Speed Control

A solution to this problem may be the development of dedicated numerical models. The aim is to replace the position sensor by indirect sensors and artificial neural network models that has the data from the indirect sensors as input and outputs speed. Design of Experiment (DoE) techniques are used to identify how the input parameters influence the output speed and in which manner the inputs interact. We consider only the linear regions of the experimental domain where the motor's behavior is useful. In such a way, a linear model can represent the motor characteristics well enough. The results obtained in this process show us which input parameters are useful as inputs to the ANN. The ANN is then trained using the DoE data obtained with a test bench as well as experimental data from the prototype of a force feedback joystick interface presented [49].

Modelling

While the linear characteristics of free vibration in the stator in the first stage can be modeled by equations of motion, the phenomenon at the stator-rotor interface

inherently displays non-linear dynamics and modelling becomes complex. Important contributions are the equivalent circuit model [179], finite element approaches [130] or the analytical model incorporating the stator-rotor interface forces and predicting the resulting motor performance as a function of design parameters [70]. Due to their complexity, these models are either difficult or even impossible to exploit for sensorless control purposes. An alternative are empirically built artificial neural network (ANN) models.

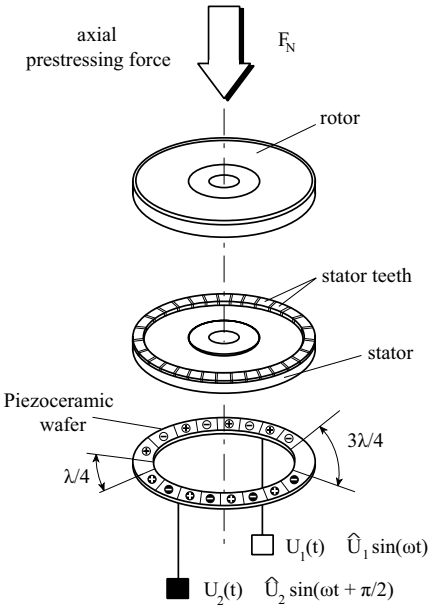

Figure 5.26. *Schematic of the motor structure. The piezoceramique wafer is etched into sectors according to wavelength (λ) of traveling wave. $\oplus$ or $\ominus$ indicate poling direction of sector.*

This means that the PUM is considered as black box. A sensitivity analysis with designed experiments identifies how the input parameters influence the output speed and in which manner the inputs interact. We consider only the linear regions of the experimental domain where the motor's behavior is useful. In such a way, a linear model can represent the motor characteristics well enough for control. The results obtained in this process show us which input parameters are useful as inputs to the ANN. The ANN is then trained using the data obtained with a test bench as well as experimental data from a haptic interface presented in [49]. The sensitivity analysis using DoE distinguishes the present project from earlier research done on the subject [190]. It allows one to find the

ideal input parameters to the neural network while optimising the accuracy of the output speed prediction.

Test Bench

A schematic representation of the test bench is shown in Fig. 5.27.

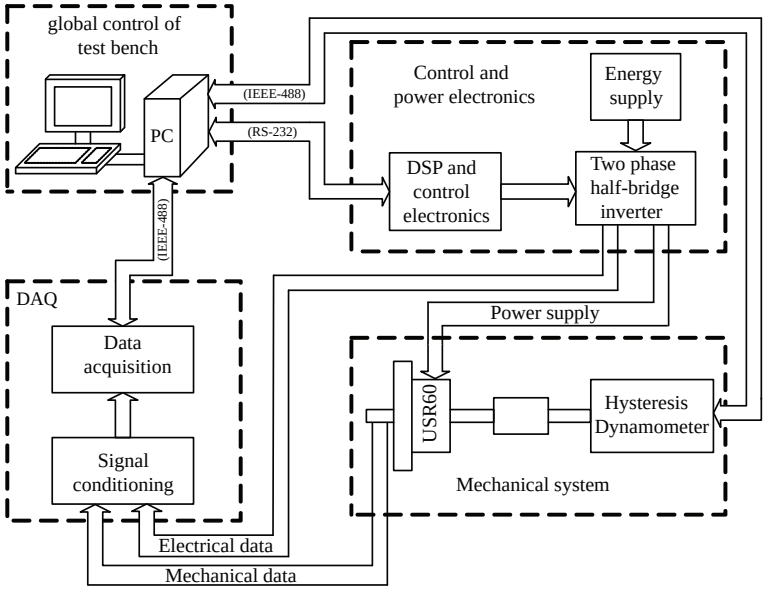

Figure 5.27. *Test bench [18]*

The mechanical system is composed of a Shinsei USR 60 PUM mounted on a aluminium support and coupled to a hysteresis dynamometer. The dynamometer delivers load torque independently of motor speed and therefore allows for measuring the motor characteristics on the full range from no load to motor blocking. Speed measurements for ANN training are obtained with a rotary optical encoder.

The control algorithms are implemented on a microcontroller. The power conversion circuit described in [18] generates the two alternating voltages which drive the motor.

Linear PUM Model

Using the experimental data with the design described in the previous section, we are able to span a linear model of the motor speed characteristics which is represented by its coefficients (Fig. 5.28).

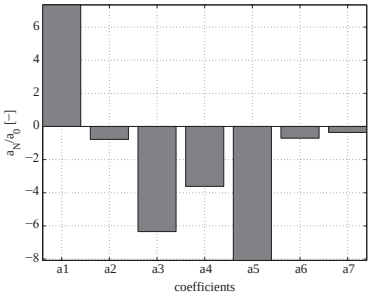

(a) *Principle relative effects of the different input parameters.*

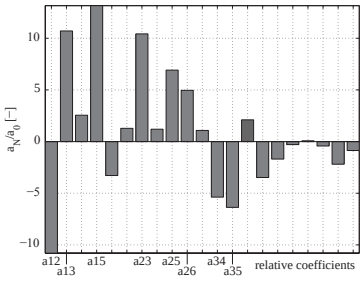

(b) *Interaction effects.*

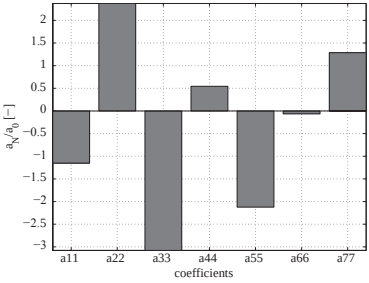

(c) *Quadratic effects.*

Figure 5.28. *Linear model coefficients.*

Temperature is held constant in experimentation, which is justified as in our application the motor is never in continuous motion for longer than a few seconds, and therefore its surface temperature remains stable. This hypothesis is valid only in well defined laboratory conditions and the study presented here must be extended to be of general validity.

The coefficients of the obtained linear model contain information about the parameter's influence on the output. Referring to Fig. 5.28a, we see that the parameters with the greatest influence on the speed output are frequency (f), current (Iph and I_{tot}) and the applied load torque (M). Fig. 5.28b represents the interaction coefficients. Interaction of Iph with Uph (a_{12}), $Itot$ (a_{13}) and f

(a_{15}) is important. The interaction of the two current measures being obvious, phase voltage and current are linked as the voltage is a image of the current by the piezoceramic impedance. Amplitude and intensity are then linked to frequency as the piezoceramic impedance is a function of its vibration frequency. From the above observations, it is apparent that frequency and load torque must be taken into account as inputs for the neural network. From the other possible inputs, phase current is selected as a third input parameter. Although its contribution to the output is slightly lower than the supply current's, the correlation with phase and supply voltage is higher.

Response Surface Analysis

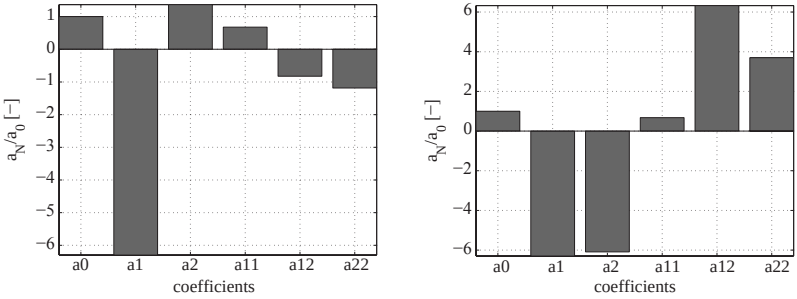

(a) *Coefficients for the response surface shown at Fig. 5.30; $a_1 \equiv f$ and $a_2 \equiv M$.*

(b) *Coefficients for the response surface shown at Fig. 5.31; $a_1 \equiv \phi$ and $a_2 \equiv M$.*

Figure 5.29. *Coefficients of the response surface models*

The excitation voltage of the piezoceramics must be chosen to obtain an optimal behavior and is not exploited as main control variable. For speed control we have thus the choice between frequency f and phase shift ϕ. We are especially interested in how the motor reacts on an externally applied load torque because this represents the intended working condition. Two studies are therefore necessary:

- speed output of the motor and the behavior under load when phase shift between the two excitation signals is varied at constant optimal driving frequency
- speed output of the motor and the behavior under load as a function of drive frequency when the phase shift between the two excitation signals is held constant.

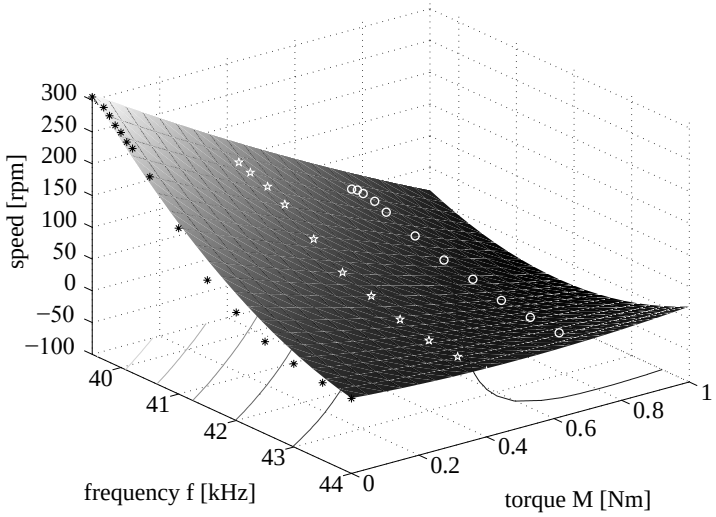

Figure 5.30. *Response surface: Torque and frequency*

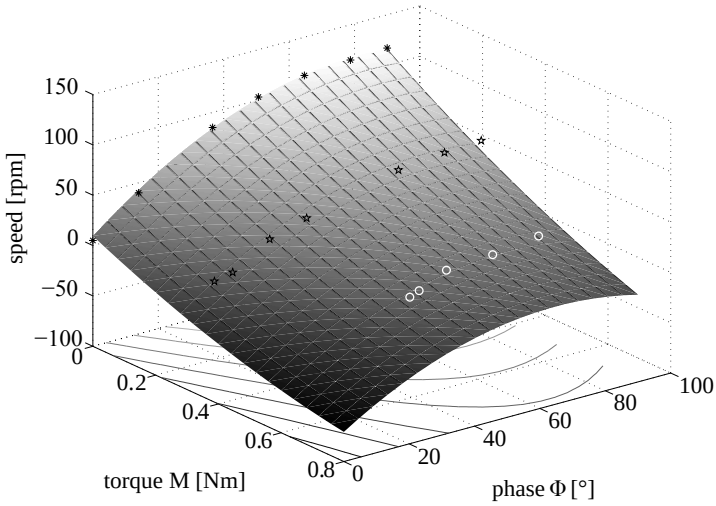

Figure 5.31. *Response surface: Torque and phase*

In both cases, a set of two parameters (f,M and ϕ,M respectively) is chosen to find the model coefficients by the method of least squares (Fig. 5.29).

The coefficients are then used to draw the response surface based on the entire normalised input space. The second order model taking into account main effects, interactions and squared terms delivers the best model of the real motor behavior, which was verified with measures outside the central composite design. At three levels of load torque, the respective second model parameter was varied in the region of interest (Fig. 5.31 and Fig. 5.30). The response surface corresponding to phase shift control (Fig. 5.31) does not match reality at high torque for low values of phase shift. Speed becomes negative there, which is not true, but rotor stops due to non-linearity in the rotor-stator surface contact phenomenon. This is known, and dead-zone compensation methods have been proposed [183]. However, for the present application, where high load torque is applied, this dead-zone is not acceptable and we therefore use a different frequency control method. Fig. 5.30 shows that by controlling the frequency on an interval of $40[kHz] \leq f \leq 44[kHz]$, the speed output follows a linear law over the entire working domain (load torque of M $\geq$ 0.8 Nm is never applied at normal working conditions).

Speed Control

Now we know that, basically, the speed of the PUM can be controlled by varying the frequency, the voltage amplitude and the phase difference of the two sinusoidal input waveforms. However, the PUM suffers from severe system nonlin-

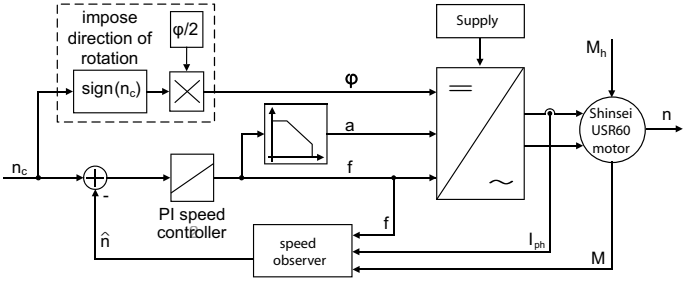

Figure 5.32. *Schematic representation of the implemented speed controller*

earities and parameter variations due to changes in load torque as well as surface temperature. Therefore, it is not possible to use a basic PID type controller without any precaution. We have developed a controller based on amplitude modulation of the supply voltage. We use the degree of freedom offered by the amplitude to linearize the frequency-speed characteristic chosen as control law in the previous section. The optimal variation of the supply voltage, making it

possible to linearize this characteristic, is obtained when the parameter of control a is a function of the frequency according to the diagram shown in Fig. 5.32.

As soon as the motor is operated outside the linear domain, it is likely to stop abruptly. Most commonly this happens when the commanded frequency is dropped below antiresonance which varies as a function of applied torque. This characteristic is taken into account in the control algorithm in order to prevent this pull-out phenomena. As we would limit the allowed frequency range by f_{min}, the drift of the resonance frequency induced by tempereture shift ΔT would decrease the maximum speed by Δn_f. Hence we introduce a speed limit n_{lim} leaving just a small security gap Δn_s relating to the resonance peak.

Speed Estimation Using Artificial Neural Networks

Estimating speed instead of using encoders reduces cost and dimensions of the haptic interface and increases reliability. An ANN algorithm is chosen for the purpose of speed estimation because of the nonlinearity of the motor characteristics and the fact that valid analytical models are still too complex to be exploited for control purposes. A neural network, given that enough information is supplied, can be trained to learn any function. Inspired by biologic nervous systems, it is composed of simple elements (neurons) working in parallel which are linked by weighted connections. These weights are adjusted during offline training in order to minimise the error between measured and estimated output.

The sensitivity analysis showed that a mathematical relation

$$n = f_{\hat{n}}(f, I_{ph}, M) \tag{5.29}$$

gives the relationship between motor speed n and frequency f, phase current I_{ph} and load torque M. Using this function $f_{\hat{n}}$, we are able to estimate motor speed. The ANN is then trained using the DoE data obtained with a test bench as well as experimental data from the prototype aiming to identify this relation. After the training step, the online simulation of the network, excited with measurements of frequency (f), phase current (I_{ph}) and load torque (M), allows us to estimate speed (Fig. 5.35).

The model of the neuron used is represented in Fig. 5.33, with R the number of elements in the input vector **p**. Each input is balanced by a corresponding weight $W_{1,R}$. The sum of the balanced inputs, with bias b, represents the input of the transfer function f_n associated to each neuron. Any differentiable transfer function f_n may be used to generate the neuron output. Several neurons combined in parallel form a layer and multiple layers are called a multi layer ANN. Every element of the input vector **p** is connected to every neuron via the matrix

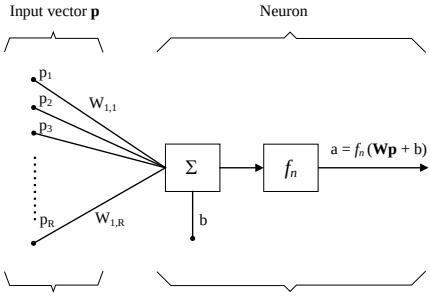

Figure 5.33. *Neuron model*

W containing the corresponding weights. The neuron model is hence applied for every neuron in the layer to generate the output vector,

$$\mathbf{a} = f_n(\mathbf{Wp} + \mathbf{b}) \tag{5.30}$$

which is the input to the next layer of the network. The structure of the ANN designed to estimate the function 5.29 is shown in Fig. 5.34. Once the structure is determined, the weights and biases for each neuron must be initialized and training can start. The training process requires a set of input vectors **p** and corresponding objective output vector **t**. During training, the weights and biases are adjusted with the objective of minimising the performance function 5.31. The performance function is defined as the mean of the squared error between network output $\mathbf{a}(k)$ and objective output $\mathbf{t}(k)$ over the length N of one training step. The weights and biases are updated at the end of each training step.

$$V = \frac{1}{N}\sum_{k=1}^{N}(\mathbf{a}(k) - \mathbf{t}(k))^2 \tag{5.31}$$

The backpropagation algorithm [143] is used to train the ANN. The idea of this algorithm is to calculate the partial derivative of the performance function with respect to each weight of the network. Let $W_{i,j}$ be the weight of any neuronal connection i-j of the network, the adjustment $\Delta W_{i,j}$ at the end of every training step is found with

$$\Delta W_{i,j} = -\alpha\frac{\delta V}{\delta W_{i,j}} \tag{5.32}$$

The algorithm calculates then the new value of the connection weight by the following Equation:

$$W_{i,j}(h+1) = W_{i,j}(h) + \Delta W_{i,j}(h) \tag{5.33}$$

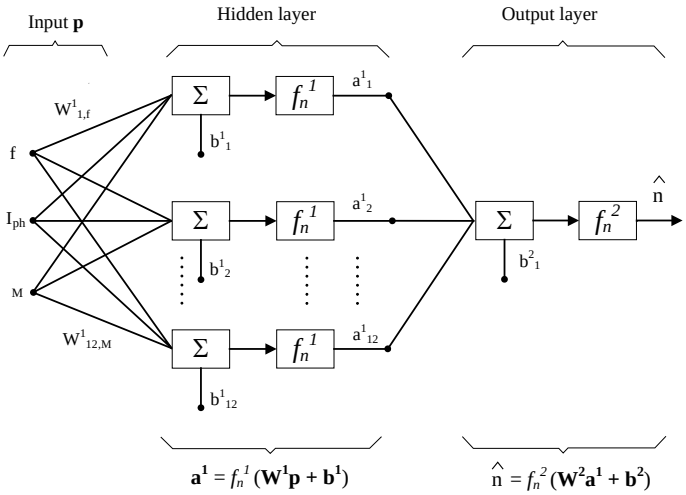

Figure 5.34. *The ANN is composed of a hidden layer with 12 neurons (sigmoid type transfert function) and a output layer with a single linear neuron.*

where h is the h^{th} iteration of the backpropagation algorithm.

To find the minimum of the performance function 5.31, we apply the Levenberg-Marquardt algorithm [8]. The Hessian matrix (second derivatives) is approximated as

$$\nabla^2 V = \mathbf{J}^T \mathbf{J} \tag{5.34}$$

and the gradient can be computed as

$$\nabla V = \mathbf{J}^T \mathbf{e} \tag{5.35}$$

where **J** is the Jacobian matrix that contains first derivatives of the network errors with respect to the weights and biases, and **e** is a vector of network errors. Computing the Jacobian matrix through a standard backpropagation technique is much less complex than computing the Hessian matrix [68].

Finally, with our network structure shown in Fig. 5.34, an analytical approximation of the function 5.29 given by the ANN after being trained, enables speed estimation (Equation 5.36).

$$\widehat{n} = f\,{}^{2}_{n}\left(\mathbf{W^2}\left(f\,{}^{1}_{n}\left(\mathbf{W^1}\,\mathbf{p} + \mathbf{b^1}\right)\right) + \mathbf{b^2}\right) \tag{5.36}$$

Where

$\mathbf{W^1}$ is the weight matrix for the connection between the hidden layer and the input of the network.

$\mathbf{W^2}$ is the weight matrix for the connection between the output layer and the hidden layer of the network.

$\mathbf{b^1}$ is the bias vector of the hidden layer.

$\mathbf{b^2}$ is the bias vector of the output layer.

p is the input vector containing here the values of frequency, phase current and load torque as follows:

$$\mathbf{p} = \begin{pmatrix} f \\ I_{ph} \\ M \end{pmatrix} \tag{5.37}$$

The transfer function of the hidden layer (cf. Equation 5.38) is of sigmoid type, which allows the identification of non-linearities, while the transfer function of the output layer is of linear type, which means that the output may be outside the interval [-1 1].

$$f\,{}^{1}_{n}(x) = \frac{2}{(1 + e^{-2x})} - 1 \tag{5.38}$$

$$f\,{}^{2}_{n}(x) = x \tag{5.39}$$

Experimental Results

The ANN is trained offline with the backpropagation method in 500 epochs using the DoE data. To verify the validity of the proposed speed estimation method, the estimated rotor speed is used as actual speed in the PI speed controller (cf. Fig. 5.32). We compare the predicted motor speed $\widehat{n}$ to the measured motor speed for the transient response (Fig. 5.35) and the steady-state response (Fig. 5.36). While the speed prediction error is below 5% when the temperature remains approximatively constant, the error reaches 10% when the maximal resonance frequency shift due to motor heating is reached.

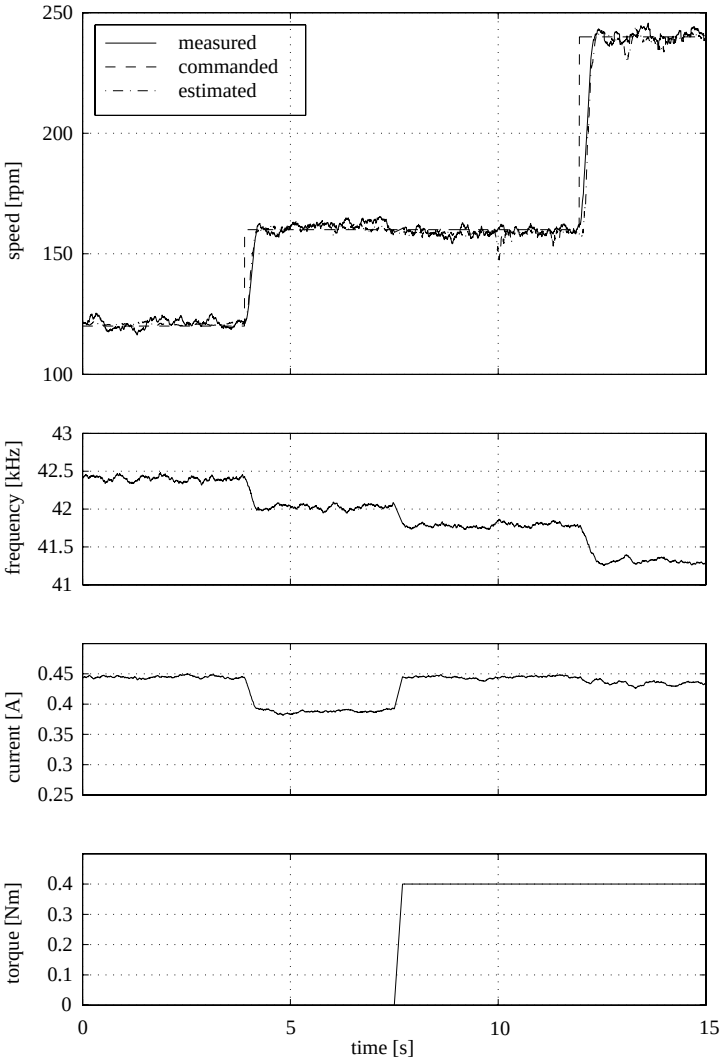

Figure 5.35. *The results of speed estimation: transient response*

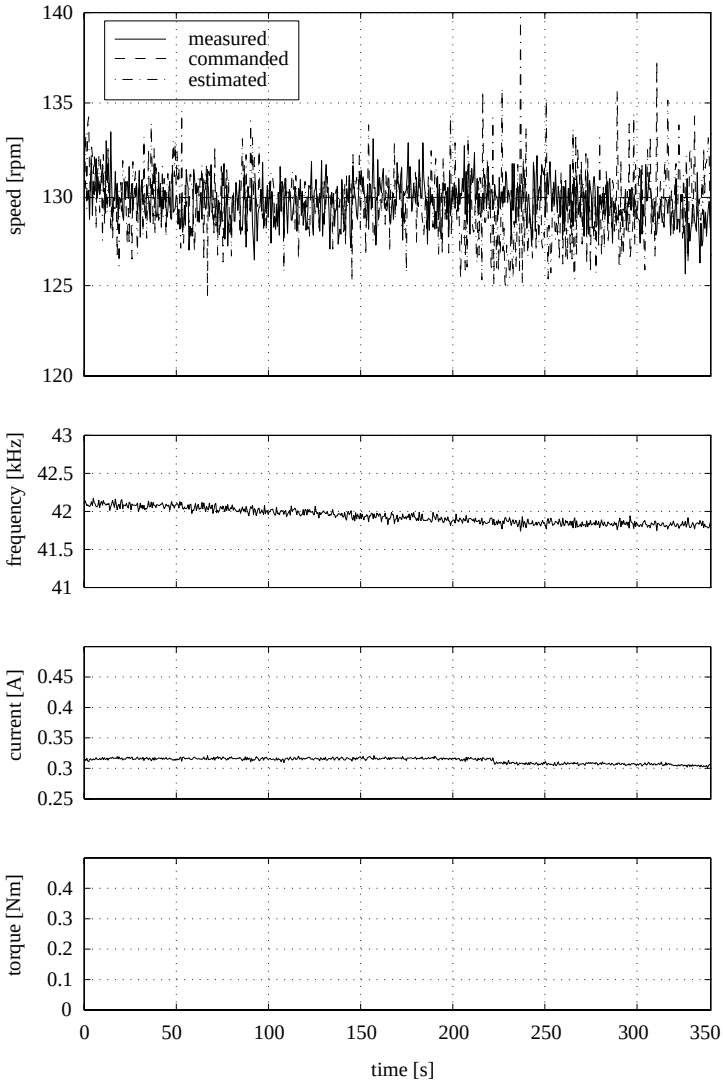

Figure 5.36. *The results of speed estimation: steady-state response*

Hence, the proposed speed estimation method is valid for the application in the haptic feedback device, but is less accurate for continous operation of the PUM. Design of experiments methods make it possible to precisely identify the sensitivity of the speed output on the different input parameters of the PUM. This approach is particularly interesting because significant data can be acquired with a minimal number of experiments. Using this data, we designed an ANN modelling the rotor speed of the PUM based on frequency, phase current and load torque measures. The implemented speed estimation based on this ANN model was tested for its transient and steady state response. However, while the results were good for the presented application, validity for other PUM and different applications is not given.

5.4.3 Motional Admittance Modulation (MAM)

It is possible to split the motional admittance in the electric equivalent model in its stator and rotor components, as seen by the stator (Fig. 5.37). In this control view of the model, the stator terms C_{ms}, L_{ms} and R_{ms} refer to the stator compliance, equivalent mass and losses, whereas C_{mr}, L_{mr} describe compliance and mass of the local rotor section brought into vibration by the stator impact and the losses R_{mr} met thereby. For a given stator configuration, the stator terms vary with temperature and other external influences. The dynamics of these variations being very small in comparison to the dynamics of rotor motion, the stator terms are supposed constant. The same consideration holds for the rotor terms, if the rotor mass and compliance is monotone along the contact region and the contact interface uniform. Here, the motional admittance modulation may be introduced. If one or several of the rotor terms are made dependant of its position with respect to the stator, the motional admittance becomes a function of position. Its variation can then be measured on the drive signals. For the realisation, the following conditions apply.

If a resonance frequency of the rotor matches stator resonance, the method is not valid. This is because then, the displacement in the rotor would not be limited around the contact region as a reaction to the stator impact any more. Instead, the rotor displacement would correspond to the excited Eigen mode independent on the position with respect to the stator.

The MAM is not a standstill position detection method. A certain excitation level must be reached to visualise the effects on motional admittance. Therefore, no detection at low speed is possible, and we encounter similar limitations as in self-commutated PM motors at start-up.

The modifications must match the contact nature. This is, in the case of a standing wave PUM, the number of equally spaced rotor variations must match the number of contact operators of the stator. If this is not the case, the effect is

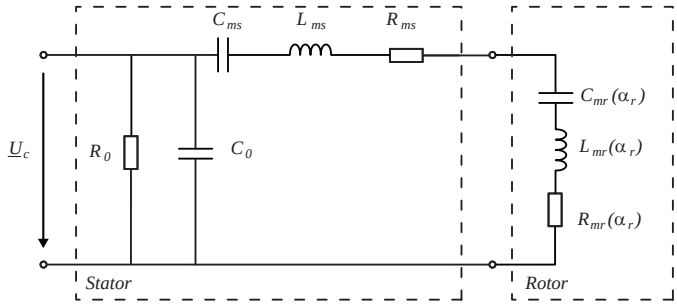

Figure 5.37. *Control view of the equivalent electric model. Indexes s and r designate stator and rotor, respectively*

blurred out and detection made difficult. The methods is therefore not transferable as is to other PUM concepts such as travelling wave motors.

During the design process it must be kept in mind that the considerations on motional admittance modulation are valid only if the above conditions are fulfilled.

Three distinct implementations of the MAM are possible. A local modification of the rotor stiffness will influence C_{mr}. Local mass variations have an effect on L_{mr}. And finally, the introduction of lossy behaviour affects R_{mr}. In reality, however, a mass modification is not obtained without a variation in stiffness and therefore modifications of L_{mr} and C_{mr} are coupled. As efficiency should just not be reduced by the method, a variation of the motional resistance, which would translate to an artificial introduction of losses for instance in the form of a compromised contact interface, is not considered.

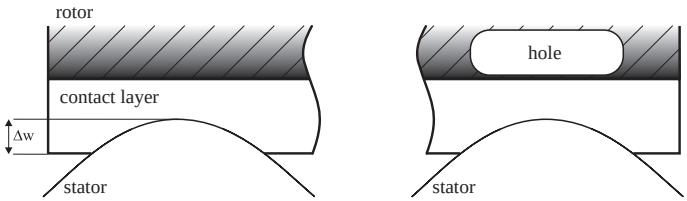

Figure 5.38. *Modulation of the motional admittance by mass and compliance variation of the rotor. Δw is the penetration depth of the stator in the contact layer of the rotor.*

For an analog impplementation of the frequency tracking controller, the control frequency of the PLL is an image of its output frequency and yields therefore

directly some information on the rotor position.

In the case of a digital implementation of the optimal working point tracking controller implemented in a digital signal controller (DSC), the frequency variation of the excitation signal is directly available.

5.4.4 Indirect Position Detection for OEM PUM

Outgoing from the MAM method, another configuration with similar physical implications is imaginable in the case of OEM motors where design for self-sensing is not applicable. When, the rotor impacts to an external mass in the form of a mechanical position reference, the oscillating mass is modified. In this way, an end of motion range detection algorithm may be implemented by analogy.

Detection Principle

In concrete terms, we assume that the piezoelectric element of the motor is fixed at one extremity as it impacts to an external load of mass M as shown in Fig. 5.39. The mass of the piezoelectric element is very large in comparison to the one of the contact setup.

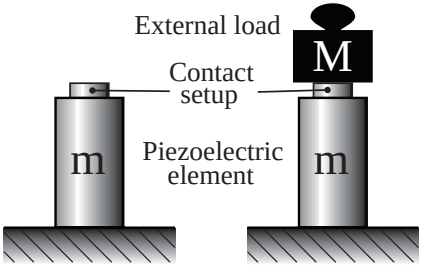

Figure 5.39. *Bumper impact seen as increase of the vibrating mass*

From (4.1) we calculate the effective mass m_e of the piezoelectric element, which is approximately $m/3$. Furthermore, approximating the resonance frequency of the piezoelectric element by an ideal mass and spring system, the resonance frequency is given by:

$$f_r = \frac{1}{2\pi}\sqrt{\frac{1}{m_e C_m}} \tag{5.40}$$

These simplifications are justified, as the quality of the impact phenomenon is well represented. Concerning the quantification of the effect, the precision of the measurement system must be calibrated with the digital controller. The resonance frequency after connection to the rotor with displaced mass m_r is given by f_r'.

$$f_r' = f_r \sqrt{\frac{m_e}{m_e + m_r}} \tag{5.41}$$

Hence, considering a second order system, the consequent phase shift can be approximated as $\Delta\phi$.

$$\Delta\phi = 2arctan\left(\frac{f_r'}{f_r}\right) \tag{5.42}$$

5.5 Summary

Optimal working point tracking and position control techniques were proposed.

Three of the discussed optimal working point tracking methods were thoroughly evaluated. A self-oscillating driver (SOD), a maximum power point tracking (MPPT) approach and a phaselock loop (PLL) circuitry. The SOD can not be implemented in digital control and will therefore not be retained here, where a test bench with maximal flexibility for the evaluation of position controllers is searched. Its potential performance for particular applications in conjunction with integrated drive and control electronics is however uncontested. In a comparison of the MPPT and the PLL controller dynamic responses, the PLL showed a superior performance. A PLL resonance frequency tracker is therefore implemented while considering the basics in sampled signal analysis.

Whereas the PLL could be identified as best practice for the inner control loop, position control must be implemented in accordance with a specific application. Position observation by measuring other motor characteristics such as temperature and torque in conjunction with a ANN motor model is unrewarding. Firstly, the goal to replace direct sensors by simpler ones is reached only for very particular applications and does therefore not satisfy the requirement of a generally applicable method. Secondly, while good results are obtained for speed control, position control is out of reach. Therefore, the discussed indirect measurement techniques based on motional admittance modulation will be evaluated in practice.

CHAPTER 6

Design: Mechatronic Locking Device

Contents

6.1 Introduction

The developped design methodology will be applied to the example of mechatronic locking devices wherein a mechanical locking configuration must be toggled between a locked and an open state at a low response time. The load to be moved is very small and the wanted motion range moderate. Historically, door lock cylinders are operated manually by the user when he rotates a key in a key slot for opening a door. The market which is more interesting to companies in the segment, is however the automated version of door locks. A special product type, that will be addressed here, is a mechatronic lock cylinder which is foreseen for both, traditional mechanical and electronic operation. This configuration adds some specific requirements to the design problem. Namely, a key slot as known from the traditional lock cylinders must still be available.

6.1.1 Mechanical Cylinder Lock

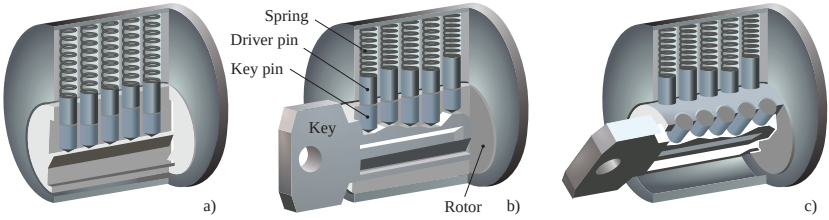

Figure 6.1. *Working principle of the pin tumbler lock mechanism [229].*

The outer lock cylinder casing has a cylindrical hole in which the plug is housed. To open the lock, the plug must rotate. The plug has a straight-shaped slot known as the keyway at one end to allow the key to enter the plug; the other end has a cam or which activates a mechanism to retract the locking bolt. A series of holes are drilled vertically into the plug. These holes contain key pins of various lengths, which are rounded to permit the key to slide over them easily. Above each key pin is a corresponding set of driver pins, which are spring-loaded. The outer casing contains vertical shafts, which hold the spring-loaded pins. The opening mechanism is shown in Fig. 6.1. Without a key in the lock, the driver pins are pushed downwards, preventing the rotor from moving. When the correct key is inserted, the gaps between the key pins and driver pins align with the edge of the plug. With the gaps between the pins aligned with the shear line, the rotor can rotate freely hence enabling opening of the lock.

6.1.2 Piezoelectric Locking Device

Existing mechatronic locking devices are actuated by DC motors. Complex security setups are necessary to prevent the motor to be moved when not supplied or to impede magnetic picking. PUM respond better to the combined challenges of high safety, high efficiency, low cost in mass production, and easy integration into small mechatronic devices. As a considerable holding torque is inherent to PUM, no blocking mechanism is needed. The bolt can be inserted by direct actuation, either with linear or with revolving motion. Existing mechatronic locking device concepts feature or a hand knob for the electronics or place the electronics in a specially arranged slot in the door (Fig. 6.2). The goal to integrate the electronics within the European formfactor dimensions is very central for the search of a new solution. Besides a motor concept designed for easy integration into the device, an important issue is therefore the replacement of the direct position sensors.

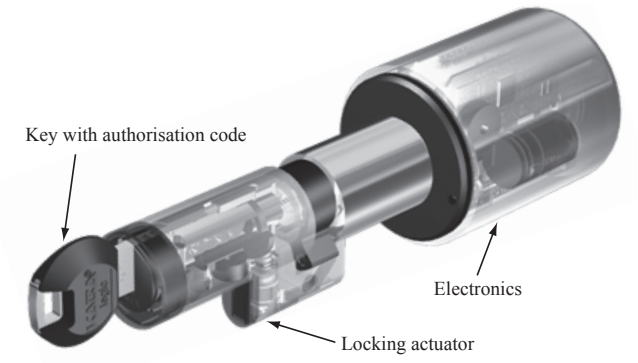

Figure 6.2. *Existing mechatronic locking system*

Outgoing from the piezoelectric actuation principles (Appendix A), linear and rotary concepts are developped to reach this goal.

The flow chart of Fig. 6.3 illustrates the way to the new solution. The main considerations are explained in the following sections. First, the requirement specifications are evaluated and general issues on test benches and digital control are introduced. Section 6.5 treats a custom linear motor design. Because this motor did not satisfy the requirements, in Section 6.5.2 the linear locking device based on a linear OEM PUM is presented. Finally, in Section 6.6 a rotary locking device is proposed.

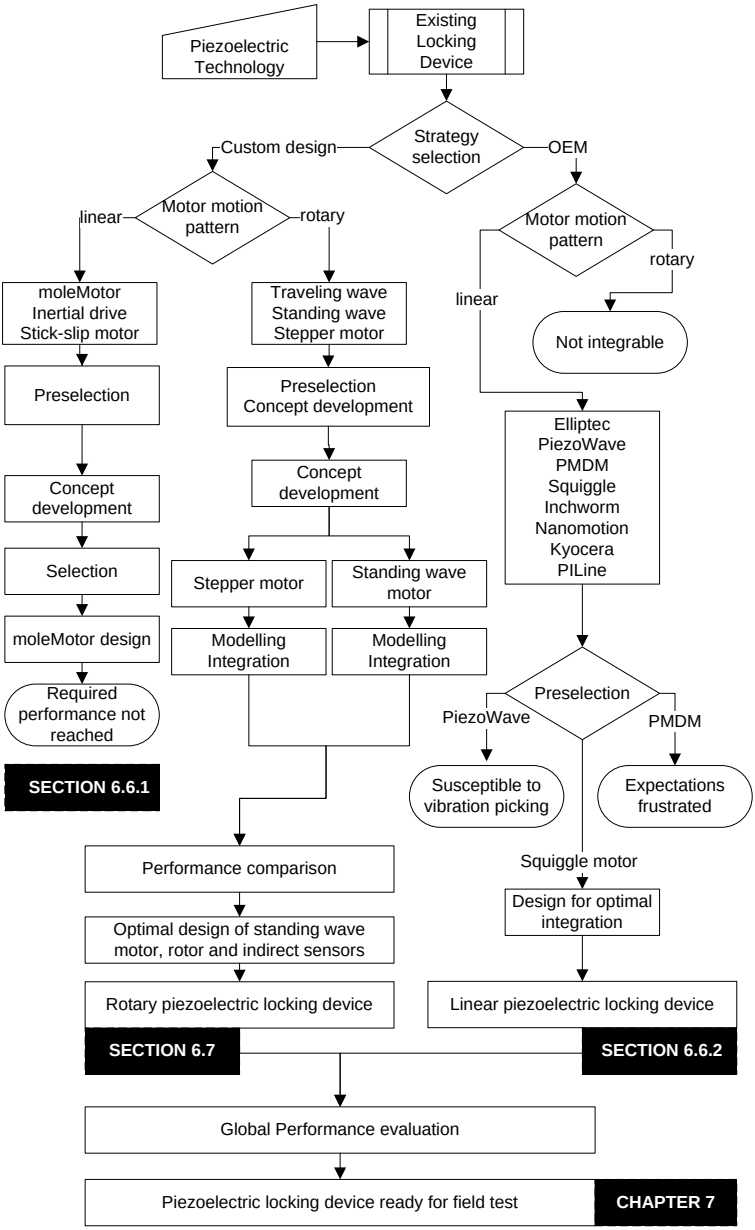

Figure 6.3. *Flow chart of the solution finding process*

Table 6.1. *Requirement specifications*

Functional specifications	
Enable state change ”open/closed”	
Permanent state monitoring	
Compatibility with all form factors	
Release time from wake-up	< 175 ms
Release time from move command	< 30 ms
Torque resistance (applied to cylinder rotor)	10 Nm
Locking bolt active force	4 N
Low power consumption, peak current	< 150 mA
Voltage	2.3 - 5.0 V
Longevity, reliability	100’000 cycles
Self-impeding	yes
Resistance: temperature	-20/+80 $°C$
Resistance: shock attacks	1000 g
Resistance: magnetic picking	yes
Resistance: vibrations	yes
Resistance: chem., therm. Attacks	yes
Resistance: contact discharge	6 kV
Resistance: air discharge	8 kV
Dimensions of electronic circuits	
Max. connection cross-section	1.0 mm^2
Max. driver volume (HxBxL)	18x16x7 mm
Acceptable distance drive-actuator	100 mm
Dimensions of mechanics: Rotating setup	
Max. outer diameter (OD)	15.0 mm
Min. inner diameter (ID)	11.5 mm
Max. overall length (incl. prestressing mechanism) (B)	4.6 mm
Min. rotor length (b)	3.0 mm
Min. blocking surface	2.0 mm^2
Dimensions of mechanics: Linear setup	
Max. length	19.0 mm
Max. breadth	2.3 mm
Max. height	7.4 mm
Min. blocking surface	2.0 mm^2

6.2 Requirement Specifications

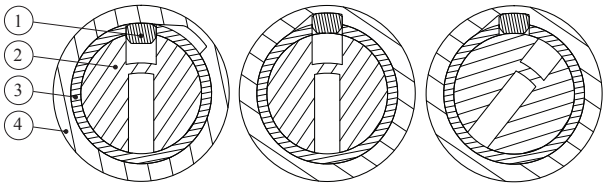

Figure 6.4. *The components of the schematic representation are 1: Locking bolt; 2: Lock cylinder rotor with key slot; 3: Lock cylinder stator; 4: Motor rotor.*

Mechanical-electronic or electronic lock cylinders need some sort of mechanical actuator to change the state of the lock from ”closed” to ”open” and vice-versa depending on whether the authentication is positive or not. Often the lock cylinder features some sort of locking bolt in its stator. To inhibit opening of the lock, this bolt can be moved into an opening in the rotor, blocking its movement. The task of the piezoelectric locking device is to move such a locking bolt to enable changing the locks state. While the motion of this actuator can be either rotational or linear, the bolt's relevant movement will always be translational. The motor must enable the state change ”open / closed” with a 3V battery supply, maintenance cycles being 2 years. The task of an actuator for the piezoelectric locking device is to block and release the lock cylinder as shown in the conceptual study of Fig. 6.4. Three states are distinguished. The locking device may be open or closed. In its open state, the cylinder rotor can be rotated manually by the user with a key or a door knob.

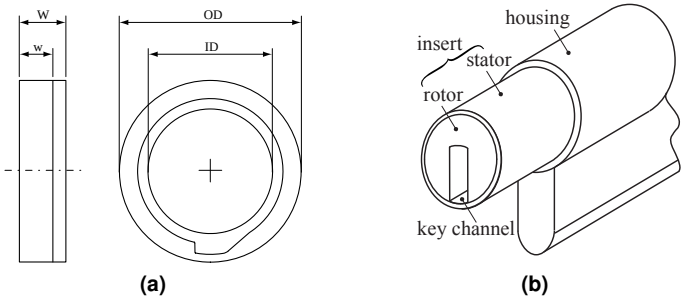

Figure 6.5. *a) Dimension of the rotary piezomotor to fit the European formfactor shown in b)*

The external dimensions of lock cylinders ar standardised. These standards are called formfactors. The objective of using a piezoelectric motor for locking device actuation is to find a solution that suites all formfactors. This goal can be achieved by integrating the actuator to the cylindrical housing of the European formfactor, because the european cylinder has the smallest diameter among all formfactors (Fig. 6.5). The functional specifications are given in Table 6.1.

6.3 Test Bench

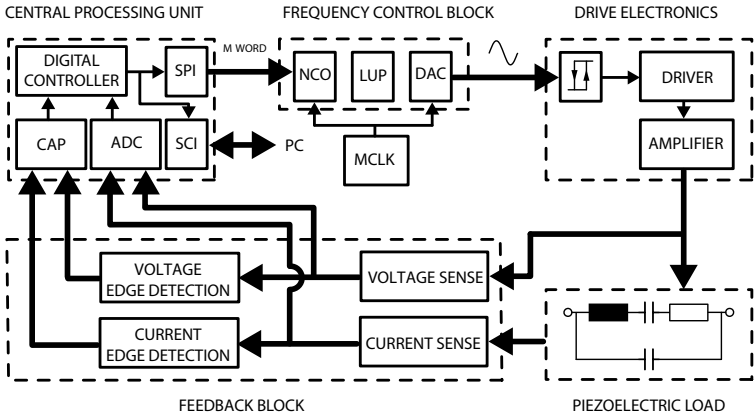

Figure 6.6. *Electronic circuit block diagram*

Motor design, the considerations on drive electronics and the developped control techniques must be integrated as to be able to evaluate their overall performance. In order to fulfil the miniaturisation requirement, the drive and control electronics must be integrated on a single chip, either a digital controller implemented on a DSC with external components or an integrated analog controller. The main constituents will be on the one hand the PLL based frequency adaptive oscillator and on the other hand the integrated CMOS DC-DC step-up converter that boosts the voltage available from battery supply (approximately 2.8 V) to the necessary level to drive the piezoelectric motor. For a realisation example of such an application specific integrated circuit (ASIC) refer to [66]. Here, a fully digital control approach was chosen, instead. The core of this system is the electronics test bench, bringing together the tools for digital control, power

electronics to drive the motor as well as a communication interface for data acquisition and command. An oversight on the test bench is given in Fig. 6.6. The central processing unit is a Texas Instruments 28335 floating point DSC. Fig. 6.7 gives a picture of the complete control electronics configured for the Squiggle motor. The visible part on the top face comprises the frequency control block as well as drive and feedback electronics. The digital signal controller is integrated in the developper kit below.

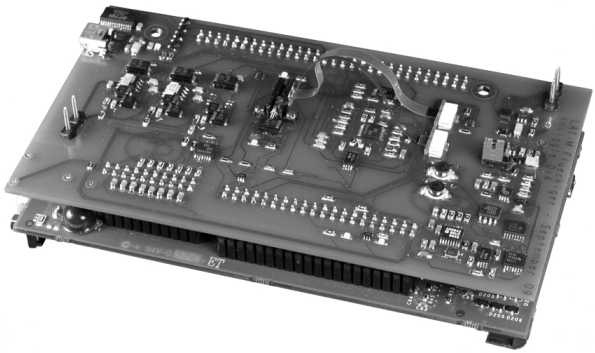

Figure 6.7. *Evaluation electronics*

6.4 Digital Control

The control electronics test bench places at our disposal a complete setup for communication and control. The digital controller implemented on the DSC being its core element, it is here, where information is gathered together and used in a suggestive way.

6.4.1 DSC Programming Fundamentals

The distinction between Low-level programming is fundamentally distinct from software engineering. A neat knowledge of the hardware is indispensible, not only to be able to design high performance code, but for simple security and robustness reasons. Although there are different beliefs as to the best approach to choose for low-level code design, some basic guidelines in digital control system analysis and design are a general imperative.

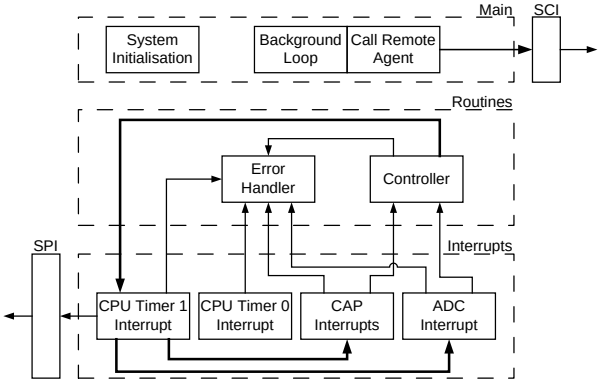

Figure 6.8. *Code Structure*

- Values that are set by background code and evaluated in interrupt handlers must be modified with the corresponding interrupt disabled.
- Checks must be performed to ensure that new control values have been calculated before updates are done to control circuitry.
- Checks must be performed to ensure that new control inputs are not overwriting values that have not been used by the control routines.
- The software stack must be checked for overflows.
- The watchdog timer must always be enabled. The watchdog timer consists of a timer and a register that must be written to before the timer has expired. If the timer expires before the register is strobed, the DSP chip is reset.
- Global and external variables are avoided.

In order to implement a controller, it is necessary to have a basic code framework that allows specific timing and data input/output to be maintained. That is to say that interrupts and tasks should be compact, fast and remain separated by function. The core control, system tasks and user interface are all called from a single background task. What functions these routines perform is based solely on data inputs from interrupt service routines. Basically this means no interrupts, no action. Also of considerable note is the control of data with respect to system inputs as well as control output. Additionally, an error handler concept is adapted from [136].

6.5 Concept 1: Linear Motor

In the first part of this section, the design of an original solution is presented. Alternatively, an OEM motor is evaluated, which will be presented in the second part of this section.

6.5.1 Design of a Linear Tuning Fork Motor

The basic idea is to design a flat single-phase motor which can be integrated along the key slot of the locking cylinder. Fig. 6.9 illustrates the concept.

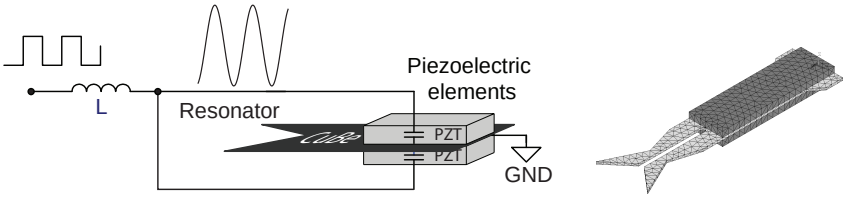

Figure 6.9. *Electric supply configuration of the tuning fork motor and FEM model*

Working principle and modelling

In Fig. 6.10, a functional model of the linear motor is shown. The actuator is placed within a flexible guidance, which at the same time preloads the resonator tips and guides the linear movement of the actuator.

Unlike the motors using the direct working principle [227], the surface points at the resonator tips of the linear motor that are in contact with the guidance do not perform an elliptical movement. Rather, the particular displacement of the resonator corresponds to a pushing or pulling movement respectively. The piezoelectric plates are placed so that the positive potentials are at the exterior surfaces and the negative potential comes into contact with the resonator. This configuration allows for stimulating two of the resonator's Eigen modes at the close by frequencies 84 kHz and 69 kHz and realises hereby a single phase bidirectional motor (Fig. 6.9). The displacement of the Eigen mode at 84 kHz pushes the actuator forward. At the 69 kHz Eigen mode, the actuator is pulled backward. Particularly, in the first part of a displacement cycle, the resonator tips bend toward the contact. Due to the frictional contact between the resonator tips and the guidance a force is created, that causes the actuator to move in linear direction. When the resonator tips bend away from the guidance during the second

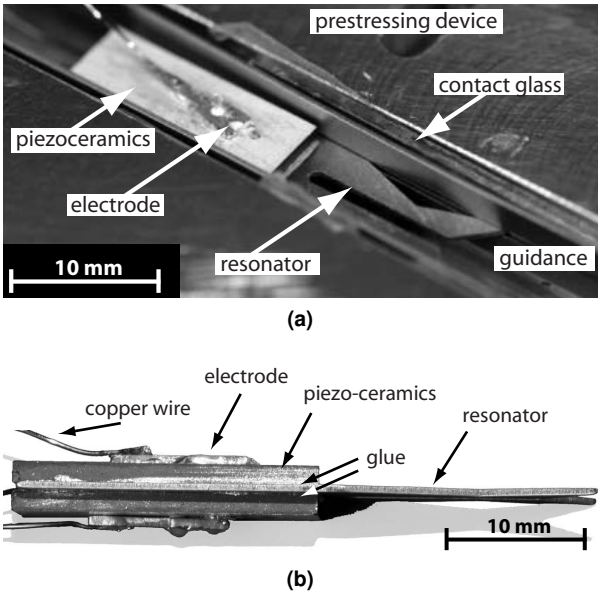

Figure 6.10. *a) Functional model of the linear motor; b) Side view of the actuator.*

part of the displacement cycle, contact is lost. The actuator continues to slide in the same direction because of the relatively high mass of the whole resonator compared to the mass of the tips. This working principle is illustrated in Fig. 6.11. In the simulations that are displayed by these sequences, the contact was not simulated and the resonator was moving freely. To drive the motor, a single sinusoidal signal is applied to both piezoelectric elements simultaneously in order to excite the resonator's Eigen modes. To change direction, the frequency must be switched between 84 kHz for forward motion and 69 kHz for backward motion.

Model validation

Functional models of the linear motor were manufactured at the different stages of the design process for validation purposes. In order to quantify the displacement amplitudes of the resonator tip, interferometrical vibration measurements were done with a Polytec MSA-400 vibrometer mounted on a microscope. In the setup, the resonator was clamped with a piece of foam in order to emulate the closest possible the boundary conditions of the FEM simulation, as can be seen in Fig. 6.16. The vibration amplitudes had to be limited in order that on

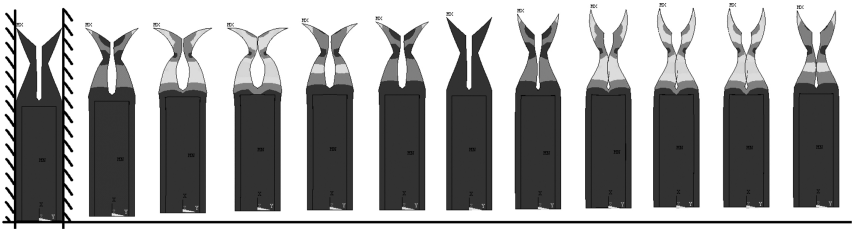

(a) *Eigen mode at 84 kHz corresponding to forward movement*

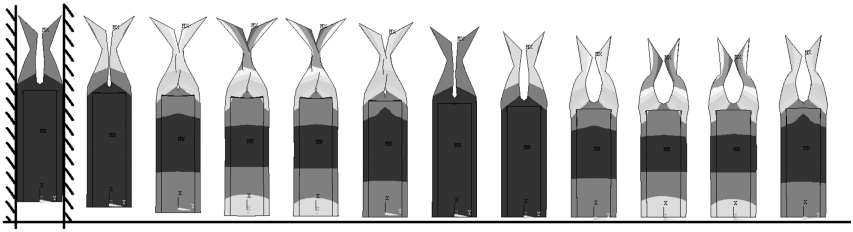

(b) *Eigen mode at 69 kHz corresponding to backward movement*

Figure 6.11. *Motion sequences of the linear motor. The displacement amplitudes are strongly overdrawn.*

the one hand vibration speed does not exceed the bandwith of the measurement instrument and on the other hand the x-component of the movement does not move the resonator out of sight for the measurement of the y-component and vice versa. A frequency sweep from 70 kHz to 110 kHz at a step of 25 Hz allows to identify the Eigen modes of the resonator and compare it to the results obtained with FEM simulation, what validates them as can be seen in Figures 6.12 - 6.15.

Firstly, the comparison of simulation results to experimental measurements allowed for improving the numerical model. Since the motor consists of different materials and interfaces between them, the mechanical damping factor is difficult to determine analytically. Hence we started harmonic calculations on the FEM simulation model with an initial guess of 0.2%. Then we used the experimental results from the functional models to adjust the damping factor accordingly. The final simulations were executed with a damping factor of 0.05%.

Secondly, once the FEM simulation model was accurate, the results obtained from the functional models were compared to it and in this manner used to validate the presented design methodology.

Fig. 6.13 compares the simulated and measured vibration amplitudes:

- Both graphs have qualitatively the same shapes and the same peaks.

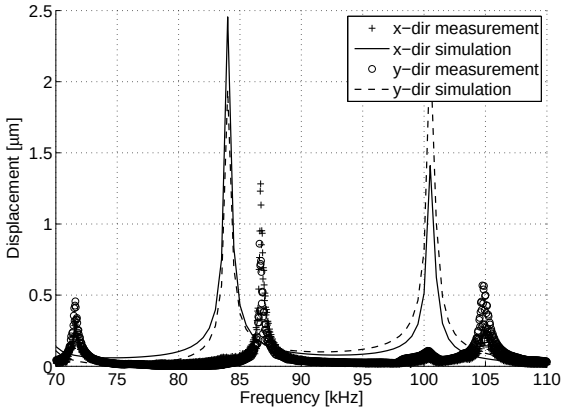

Figure 6.12. *Displacement amplitude in driving direction (x) and perpendicular to the driving direction (y): Comparison of the simulated and measured values for the free resonator in the initial configuration. Supply voltage amplitude is 4.3V.*

- The simulation predicted resonance at about 5% lower frequencies.
- The vibration amplitudes are up to 20% larger in reality.

The observed disparity lies within the expected range and is caused by the following effects:

- Properties of piezoelectric materials are not constant among samples on the one hand and vary with external conditions such as ambient temperature on the other hand.
- Only a simplified actuator was modeled, which can explain some difference in frequency and the maxima of the displacement amplitude.
- The mechanical damping factor varies from model to model due to variable piezoelectric properties and manufacturing tolerances.
- During interferometry the movement of the motor was not absolutely free. A small preload was still applied, in order to keep the motor in position.

These observations lead to the conclusion that the experiments did validate the FEM simulations as the results are qualitatively similar and quantitatively very close. No intermediate functional models will be necessary for future designs.

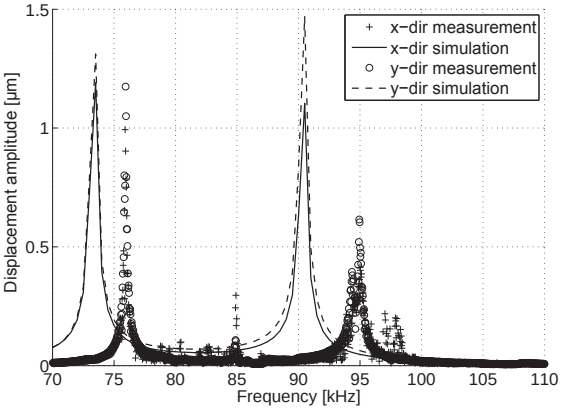

Figure 6.13. *Displacement amplitude in driving direction (x) and perpendicular to the driving direction (y): Comparison of the simulated and measured values for the free resonator as obtained after sensitivity analysis. Supply voltage amplitude is reduced to 1.5V.*

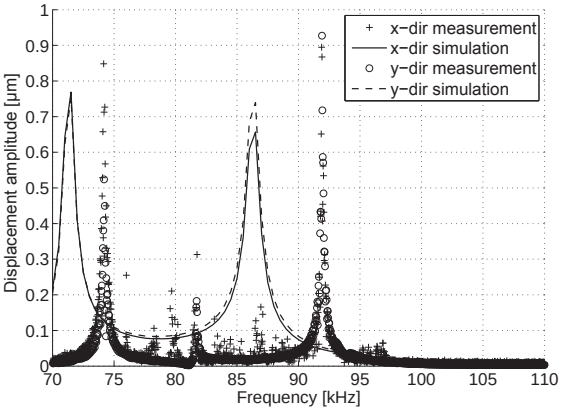

Figure 6.14. *Displacement amplitude in driving direction (x) and perpendicular to the driving direction (y): Comparison of the simulated and measured values for the free resonator as obtained after sensitivity analysis. Damping factor for simulation is reduced to 0.05 percent.*

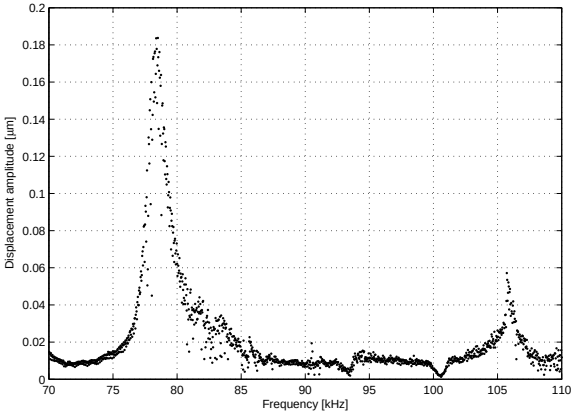

Figure 6.15. *Measurement of the displacement amplitude in driving direction for the mounted but blocked functional motor model. Supply voltage amplitude fixed at 21.5V.*

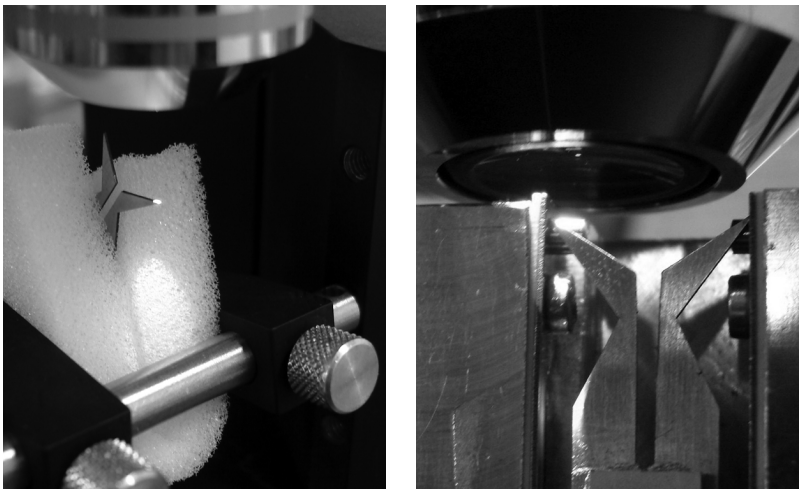

(a) **(b)**

Figure 6.16. *Setup for displacement amplitude measurement: a) Approximated free vibration with a foam fixation; b) Vibration under preload in the testbench (blocked motion).*

Methodology validation

The factors considered for the sensitivity analysis are given in Fig. 6.17 and the corresponding effects in Fig. 6.18. The significance threshold is situated at 8%. The design variables with effects a_3, a_9, a_{10}, a_{12}, a_{13}, a_{14} and a_{15} are free for the FEM optimisation, the others are fixed.

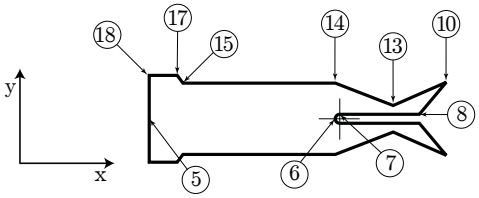

$\mathbf{a_1}$: control	$\mathbf{a_2}$: voltage	$\mathbf{a_3}$: res kx7
$\mathbf{a_4}$: res ky7	$\mathbf{a_5}$: res kx8	$\mathbf{a_6}$: res ky8
$\mathbf{a_7}$: res kx10	$\mathbf{a_8}$: res ky10	$\mathbf{a_9}$: res kx13
$\mathbf{a_{10}}$: res ky13	$\mathbf{a_{11}}$: res kx14	$\mathbf{a_{12}}$: res kx15
$\mathbf{a_{13}}$: res kx17	$\mathbf{a_{14}}$: res ky17	$\mathbf{a_{15}}$: res kx6.

Figure 6.17. *Definition of the resonator shape. The keypoints correspond to the main effects as indicated. "res k(x,y)i" designates the x and y positions respectively of the resonator keypoint i.*

The methodical resonator shape optimisation increased the displacement amplitude of the resonator tips to values up to six times higher compared to the results obtained from the initially guessed resonator shape. Fig. 6.19 compares the vibration amplitudes at three different stages of the design process. The resonator shapes used for the first FEM simulation, and the ones obtained after preoptimisation and after FEM optimisation are shown.

This observations lead to the conclusion that the experiments did validate the FEM simulations and the optimisation process as the results are qualitatively similar and quantitatively very close. No intermediate functional models will be necessary for future designs. However, with respect to the developped linear motor in particular, negative conclusions are drawn. Resonantor shape modifications proved difficult, as the modal characteristics change along with dimensions. Therefore, no functional model with stable drive characteristics could be obtained with the available resources.

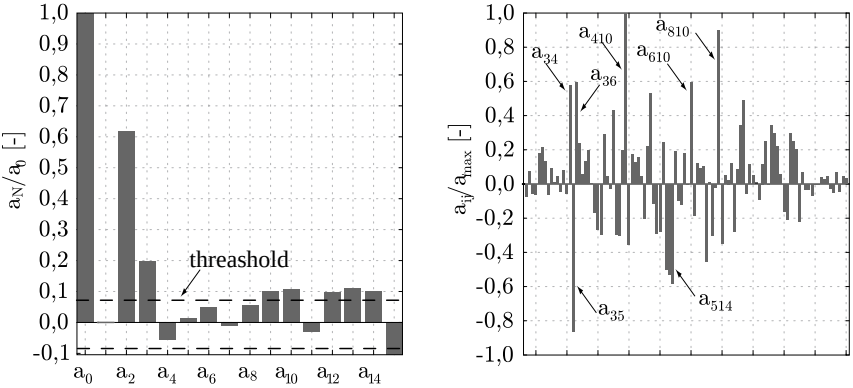

Figure 6.18. *Sensitivity analysis for the displacement amplitude in driving direction. Left: Main effects. Right: Relative effects.*

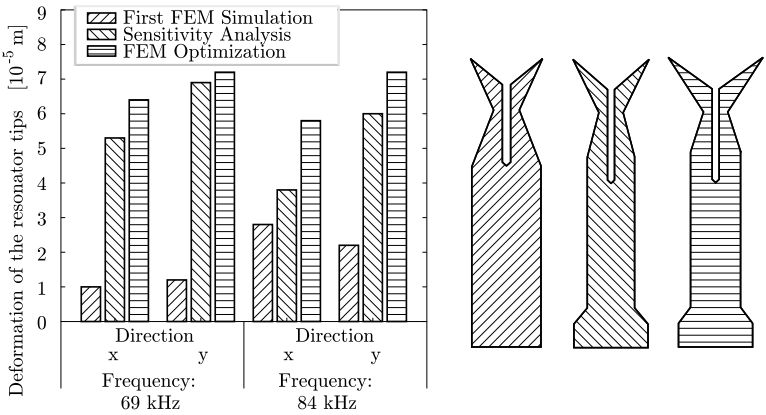

Figure 6.19. *Comparison of the displacement amplitudes and the resonator geometries at the different stages of the optimisation process.*

6.5.2 OEM Linear Locking Module

Instead of the custom made solution, a linear locking device was conceived to be actuated by an OEM motor. A functional model is shown in Fig. 6.20. The linear PUM by Newscale technology was selected. However, the motor selection process with series of test for different candidate motors is beyond the frame of this project. Only the integration of the position controller will be discussed in detail here. Tests were made with the Squiggle motor integrated into the linear locking module as shown in Fig. 6.21.

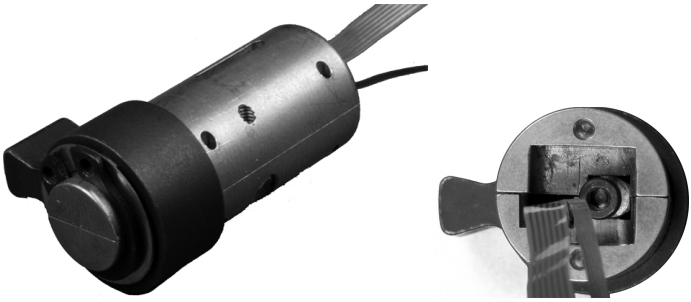

Figure 6.20. *Functional model of the linearly driven locking module*

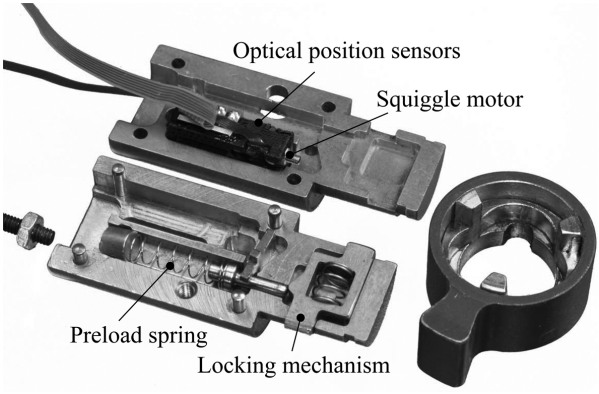

Figure 6.21. *Perspective view of the open locking module*

6.5.3 Characterisation of a Linear OEM Motor

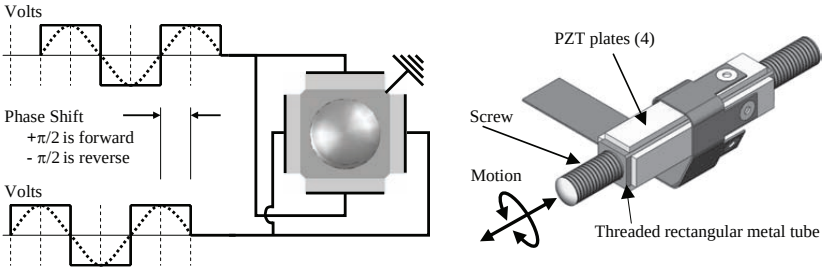

Figure 6.22. *Squiggle motor motor configuration and electric supply signals [76].*

The Squiggle linear PUM is fundamentally a threaded nut and screw (Fig. 6.22). Two-phase drive signals cause piezoelectric actuators to vibrate the nut at a fixed resonance frequency of 171kHz for the selected model. The nut vibrates in a wobbling motion that causes the screw to rotate and translate with sub-micrometer precision. The screw translation is bi-directional, and the position of the tip of the screw is precisely controlled by the driver. A position sensor is required to achieve repeatable steps.

Position Control

A potential solution to this issue will be to block the rotor mechanically at and the start and the end points of its movement in order to create an electrical reaction when the motor reaches these positions. This electrical reaction can be detected by measuring either amplitude or phase of voltages and currents. Fig. 6.23 illustrates the expected consequences of an impact with a bumper. For a few control cycles, the current will lag voltage. This phase shift may be measured by edge detection. Alternatively, when resonance frequency is tracked, the shift induced by the collision with the bumper can be detected.

In order to evaluate the practical feasibility, first, the impedance characteristics of the Squiggle motor at the different conditions were measured. Fig. 6.24a shows the admittance and phase of the Squiggle motor around the working point of $171kHz$. This measurement is repeated with removed rotor (Fig. 6.24c) and with blocked rotor (Fig. 6.24b). Fig. 6.24d compares the characteristics of these three conditions.

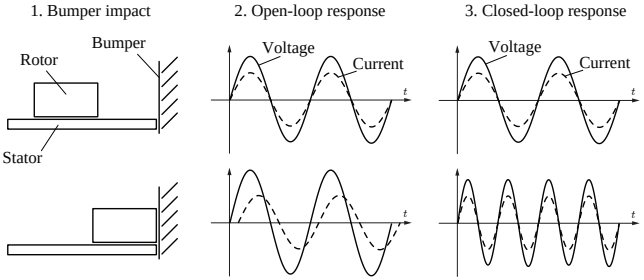

Figure 6.23. *Bumper impact*

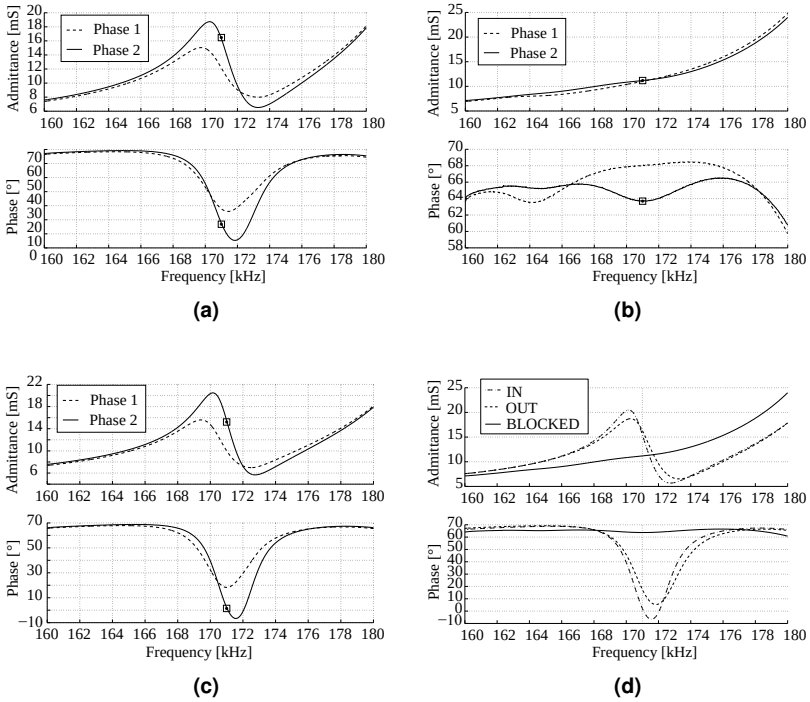

Figure 6.24. *Impedance characteristic of the Squiggle motor: a) Normal configuration; b) Blocked at bumper; c) Stator without rotor; d) Comparison of the different configurations in one plot for the first phase.*

6.6 Concept 2: Rotary Motor

6.6.1 State of the Art

Concurrently to the linear solution, an implementation with a rotary PUM was searched for. Fig. 6.25 illustrates the concept of the rotary locking device with the piezoelectric motor integrated around the lock cylinder.

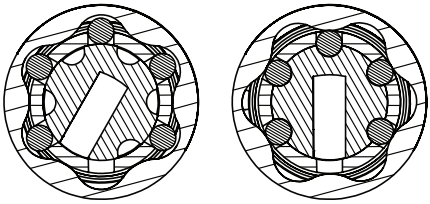

Figure 6.25. *Concept of the piezoelectric locking device using balls as locking bolts [241]*

After preliminary evaluations, two motor concepts were selected for FEM analysis. The two single phase motors are a bidimensional mode standing wave PUM and a standing wave stepper PUM, referred to as standing wave and stepper motor, respectively.

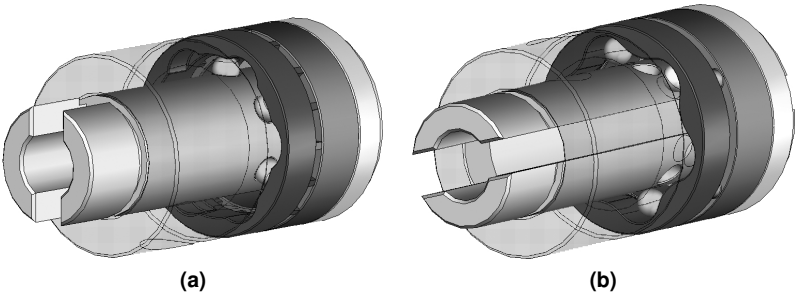

Figure 6.26. *3D CAD representation of the lock cylinder with rotational piezoelectric motor and locking bolts: a) Stepper motor; b) Standing wave motor.*

6.6.2 Standing Wave PUM

A standing wave rotary PUM is the first of two motor concepts selected for further evaluation. The development will be based on an original motor concept

first proposed by Wischnewskiy [231].

The ingenuity of the motor lies in the fact that in a single piezoelectric hollow cylinder, a standing wave of two coupled orthogonal vibration components is excited. This results in a bidimensional axial-tangential displacement by simply applying an excitation signal between the outer and inner surface of the radially poled cylinder. Furthermore, whereas the sweeping majority of known PUM use piezoelectric ceramics to excite some mechanical oscillator, in the case of this motor, the piezoelectric element is itself the oscillator, which is thus active in its entity. So far unmatched efficiency can therefore be reached [222] and manufacturing is simplified. Fig. 6.27 illustrates the electrode placement and the excited mode of this PUM.

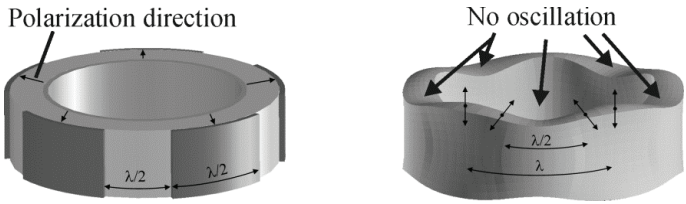

Figure 6.27. *Electrode arrangement, polarisation and corresponding displacement of the 5th coupled axial-tangential mode [221].*

More specifically, the spacing of the electrodes as well as their extension is half a wavelength of the excited mode. Hence, two groups, shifted by half a wave length, are composed of as many segments as wavelength are present in the cylinder, each. Only one electrode group is active at a time. At the central points of the active electrode sections, the axial displacement is maximal and tangential displacement is zero. At the equivalent point for the passive electrode sections, no displacement occurs. The tangential displacement is maximal at the interfaces of the electrodes. There, a surface point of the cylinder moves on a straight line trajectory at an angle of $45°$ or $135°$ with respect to the cylinder face, respectively. This configuration enables rotation in one direction when the first electrode group is supplied and the second is allowed to float. Commuting the role of the electrode groups shifts the standing wave by half a wavelength around the cylinder and thus toggles the rotation direction.

Simulation results

First of all, a modal analysis has been carried out to find out the different vibration modes of the stator, including the pushers. After this modal analysis, it has

been possible to determine the resonance frequency of the 5th degenerate coupled tangential-axial as well as the 3rd mode when a structure with three pushers is considered. Once the resonance frequencies of the interesting modes determined, harmonic responses for the two different stator configurations have been obtained.

Fig. 6.28 shows the displacements obtained for the 3rd vibration mode to obtain counterclockwise and clockwise rotations of the rotor. The resonance frequency for this specific mode is $313.61\,kHz$. Then, Fig. 6.29 shows the displacements obtained with a stator composed of 5 pushers (5th vibration mode) to obtain counterclockwise and clockwise rotations of the rotor. The resonance frequency for this specific mode is $333.15\,kHz$.

After the harmonic analysis, the transient response has been calculated. A sinusoidal AC voltage of $100\,V$ (RMS) has been applied to the set of active electrodes of the piezoelectric cylinder. For the simulations, a damping coefficient of 0.5% has been taken into account. This value is approximative and would need experimental validation.

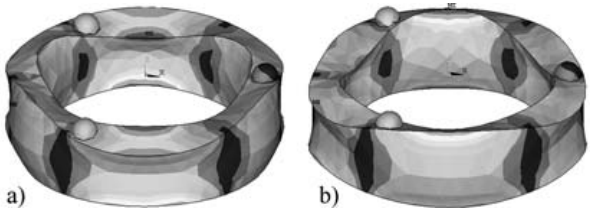

Figure 6.28. *Displacement of the stator for the 3rd mode: a) for counterclockwise rotation of the rotor, b) for clockwise rotation of the rotor*

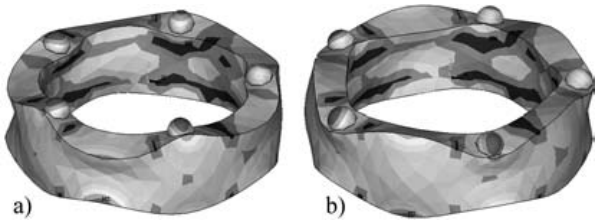

Figure 6.29. *Displacement of the stator for the 5th mode: a) for counterclockwise rotation of the rotor, b) for clockwise rotation of the rotor*

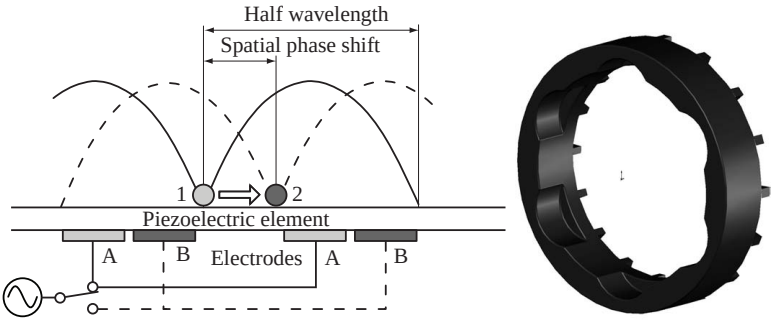

Figure 6.30. *Working principle of the stepping motor and rotor design*

6.6.3 Stepper PUM

Fig. 6.30 shows the configuration adopted for the realisation of a stepper PUM using spatially shifted standing waves. Several phases, one supplied at a time, around the annular stator allow for rotating a standing wave. When all the phase A electrodes are simultaneously excited, the standing-wave vibration shown by the solid curves can be created. Since the 8th vibration mode is adopted, there are 16 nodal lines along the annular stator. Now, if the excitation is switched to all the phase B, the resulting standing-wave vibration will be indicated by the dashed curves. Thus, by pressing a rotor with teeth, which is in contact with the stator surface thanks to a pre-stressing force, initially located at position 1, will move to a new nodal line 2, and take a rest until the next phase is turned on. The displacement between two consecutive nodal lines corresponds to the step size. By exciting the phases in sequences, the rotor will rotate step-by-step along the annular stator surface. Moreover, the direction of the stepping motion can be easily controlled by changing the sequence of the exciting phases. The 8th vibration mode was demonstrated by [27] and has been adopted for the FE simulations. Other configurations are obviously possible but for a first case study, this one has been chosen.

Simulation results

First of all, a modal analysis has been carried out to find out the different vibration modes of the stator. After this modal analysis, it has been possible to determine the resonance frequency of the 8th vibration mode. Then, the harmonic response has been obtained by applying an AC voltage of $100\,V$ (RMS)

to phase A as described in Fig. 6.30. Fig. 6.31 shows the displacement obtained. The resonance frequency for this specific mode is $354.14\,kHz$.

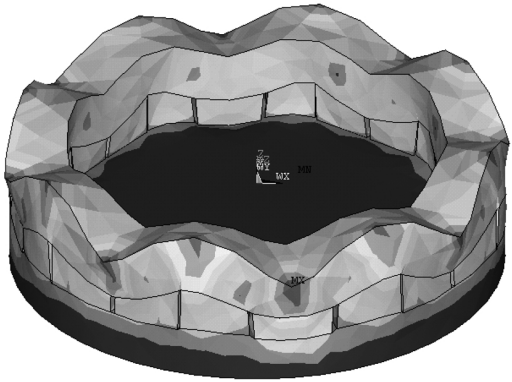

Figure 6.31. *Displacement of the stator for the 8th mode*

After the harmonic analysis, the transient response has been calculated. A sinusoidal AC voltage of $100\,V$ (RMS) has been applied to the set of active electrodes (4 electrodes of phase A for example). For the simulations, the same value of damping coefficient as previously has been considered (0.5%).

6.6.4 Selection

The first results obtained with the three different structures have demonstrated that it is possible to obtain axial and tangential oscillation components in the stator. The same conditions have been used for the three structures: applied voltage, damping coefficient, materials, mesh size. It is hence possible to directly compare the results. Table 6.2 shows this comparison in terms of the maximum amplitudes obtained at the circumference of the stator cylinder.

Table 6.2. *Comparison of the simulated vibrating structures*

Stator structure (and f_r)	Amplitudes (axial/tang.)
Standing 3rd mode ($f_r = 313.61\,kHz$)	0.12 μm / 0.034 μm
Standing 5th mode ($f_r = 333.15\,kHz$)	0.06 μm/ 0.031 μm
Stepping 8th mode ($f_r = 354.14\,kHz$)	0.09 μm / 0.015 μm

As it can be seen, the structure using the 3rd vibration mode of the standing type ultrasonic motor gives the maximum amplitudes for the lowest resonance frequency. Furthermore, the results obtained are quite similar, as well from the point of view of the resonance frequencies as of the displacement amplitudes. Moreover, these displacement amplitudes are not very high (less than $1\,\mu m$ for an applied voltage of $100\,V$) but the damping coefficient taken into account during the simulations has not been validated and may be adjustted for later designs.

Nevertheless, these first results allow us to say that these three different configurations of stators are interesting and possible solutions for the rotating setup of the locking system studied. No sensitivity analysis has been carried out yet. It would give us more information on how to modify these structures (geometry, materials, number of pushers, etc.) to obtain higher displacement amplitudes for better characteristics of the motor (speed/ torque).

6.6.5 Optimal Design of a Standing Wave PUM

We applied the FEM based optimisation methodology to the standing wave PUM.

(a) *The vibration mode at the resonance frequency of $411kHz$ for the 3^{rd} mode and the corresponding rotor motion is shown; the graphs at the bottom show the corresponding displacement. Left: first electrode group active. Right: second electrode group active.*

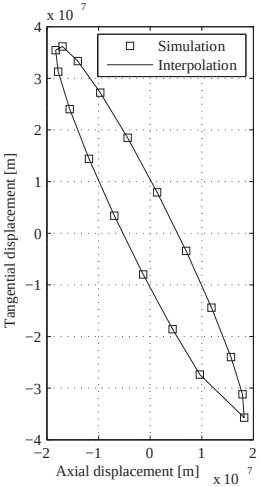

(b) *Motion path of a surface point at the interface of two electrode portions*

Figure 6.32. *Working principle of the rotory motor.*

Two designs, one with 3 wavelengths, the second with 5 wavelengths along the circumference of the stator were evaluated with initial FEM simulations The rotor motion was also simulated, but this model could not be sufficiently simplified in order to use it for the optimisation, where every iteration step involves several simulations depending on the optimisation method. Therefore, we suggest an approach, where only the stator was simulated and a quantitative and qualitative appreciation of the displacement is used to predict the rotor motion. Furthermore, it showed out that for the given dimension the 3^{rd} order mode presented bigger displacement amplitudes, why this variant is selected for the optimisation study.

Prediction of motor characteristics

It was explained that the displacement of a pusher surface point induces the motion of the rotor when a continuous pre-stressing force between the rotor and stator is applied. Due to the non-continuous nature of the contact and the non-linearities in the physics of the frictional contact, an optimisation procedure based on a complete FEM model is not practicable. Existing intermittent contact models for FEM analysis [42] are used for the design of new motors [43], [174], but their computational cost does not recommend them for optimisation. Therefore, the stator is evaluated quantitatively with a FEM model and then, for the characteristic analysis of the motor, the displacement of the surface points is analysed qualitatively. The elliptical motions at all pusher surface points have to be considered for the exact characteristic analysis of the rotary motor. The displacement to the x-, y-, and z-directions is simulated at these specific nodes using the 3D FEM model. Then, the rotary speed of the motor is determined by the velocities of the displacements, especially by the tangential ones. Hence, to simulate the number of revolutions per minute of the motor, the original coordinate axis of each elliptical motion must be transformed to a new coordinate axis. Then, the transformed elliptical motion of which the coordinate axis is rotated to the tangential direction of a circle can be calculated as shown in Fig. 6.33. The elliptical motions presented in Fig. 6.32b has been calculated in this way from the FEM simulation results to find axial and tangential displacements of a pusher surface point. Motor motion can be predicted by considering the following factors [170]:

- The displacement amplitudes of the free stator need to be of several hundreds of nanometers for a proper operation of the motor. Otherwise, a sufficiently high preload cannot be applied to the rotor.
- The tangential direction displacement component of the elliptical motion has mainly an effect on the velocity of the motor and the axial direction

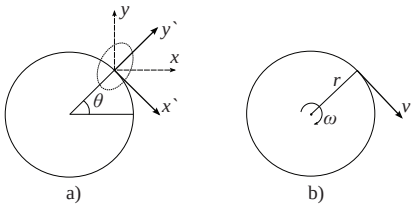

Figure 6.33. *a) rotation of the original coordinate axis to the tangential direction of a circle, b) scheme of the velocity at the rotating circle*

displacement component on the torque. It means that both need to be sufficiently high to reach a good compromise between speed and torque of the rotary motor.

- Rotation direction of the elliptical motion at all surface points must be the same for efficient operation of the motor. If not, then they cancel out each other so that the motor does not operate or the performance of the motor is decreased.

Optimisation

The system variables considered for the sensitivity analysis are given in Fig. 6.34:

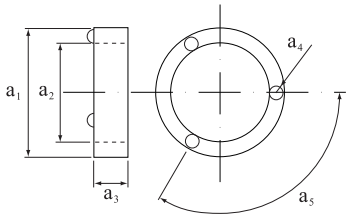

Figure 6.34. *Definition of system variables*

a_0 Mean

a_1 Outer diameter of the stator

a_2 Inner diameter of the stator

a_3 Height of the stator

a_4 Radius of pusher

a_5 Angle between pushers

a_6 Excitation voltage amplitude

a_7 Resonance frequency

Fig. 6.35 shows the normalised main effects corresponding to the Taylor series approximation of the response function. A positive effect signifies that the related factor must be increased in order to maximise the objective function, whereas when the effect is negative, the factor must be decreased.

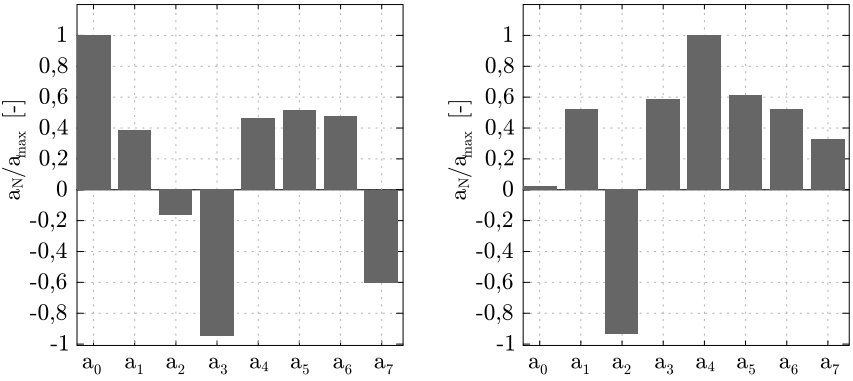

Figure 6.35. *Main effects for the rotary motor. Left: tangential displacement. Right: axial displacement.*

A larger outer diameter and a smaller inner diameter lead to higher vibration amplitudes. A bigger pusher diameter and a larger angle between them result in higher axial and tangential vibrations, as it is obviously true for a higher excitation voltage. However, the conclusion for the material thickness is more difficult. The tangential displacement is bigger for a thinner piezoceramic, whereas the axial displacement is bigger for a thicker piezoceramic. It becomes apparent that we must find a trade-off between optimal axial and optimal tangential displacement to get an optimal overall behaviour. In this case, the interactions must be considered. In Fig. 6.36, the relative effects are shown with a threshold of $\pm 20\%$ as indicated. Looking at the effects which are higher than the threshold for both, axial and tangential displacements, we see that the previous observation is confirmed: increasing outer diameter (relative effects a_{14}, a_{15}, a_{16}) and decreasing inner diameter (a_{24}) leads to higher vibrations, whereas the thickness of the ring may be fixed for optimisation.

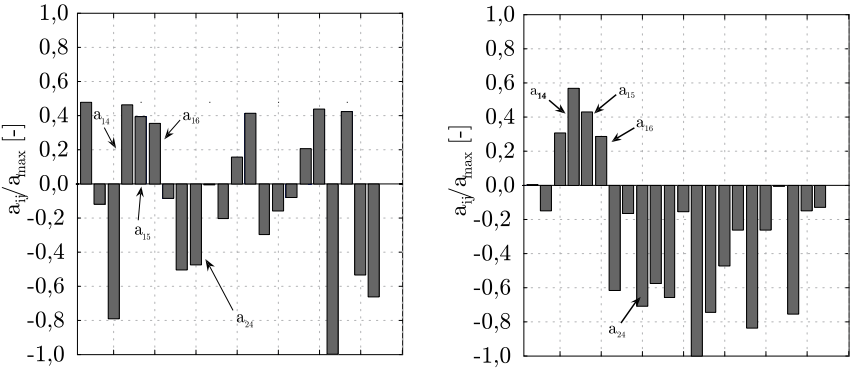

Figure 6.36. *Relative effects for the rotary motor. Left: tangential displacement. Right: axial displacement.*

The variation ranges of the free system variables could be narrowed during preoptimisation (Table 6.3).

Table 6.3. *Narrowed design variable ranges after preoptimisation*

Initial guess	Lower limit		Design variable		Upper limit
18 mm	15 mm	$\leq$	Outer diameter	$\leq$	16.75 mm
12 mm	10.75 mm	$\leq$	Inner diameter	$\leq$	11.5 mm
1.5 mm	1.5 mm	$\leq$	Pusher diameter	$\leq$	1.575 mm

The FEM optimisation resulted in an increase in axial and tangential vibration amplitudes as illustrated in Fig. 6.37. First, the geometric mean of the axial and tangential displacement amplitudes was defined as objective function. However, this solution proofed to result in a poor compromise of both. Therefore, two optimisation processes were executed, the first for maximal axial displacement amplitude and the second for the tangential one. This approach allowed for finding a first stator intended for maximal torque and a second one for maximal rotational speed. Because both amplitudes are directly linked, a maximal tangential displacement also results in big axial displacement and vice versa. As speed was the main issue, the stator with maximal tangential displacement was retained, manufactured and tested. The final design variable values are listed in Table 6.4.

The design resulting from the optimisation was tested experimentally with a functional model. The improvement in terms of displacement amplitudes with

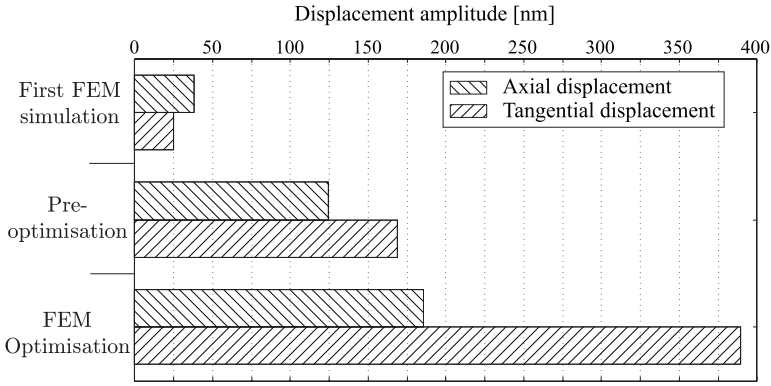

Figure 6.37. *Evolution of vibration amplitudes during the optimisation process for the rotary motor.*

Table 6.4. *Design variables after optimisation*

		Objective function	
		Axial displacement	Tangential displacement
Design variables	Ceramic outer diameter	16.27 mm	15.52 mm
	Ceramic inner diameter	10.87 mm	10.96 mm
	Pusher radius	0.78 mm	0.76 mm
Fixed variables	Angle between pushers	$\pi/3$ rad	$\pi/3$ rad
	Height of the stator	4 mm	4 mm
	Applied voltage	30 V	30 V
Results	Max axial displacement	458.63 nm	181.7 nm
	Max tangential displacement	157.9 nm	382.52 nm
	Resonance frequency	398 kHz	421 kHz

respect to the results presented in [45] could well be achieved by optimising the stator geometry (Figures 6.38 and 6.39). This validates the way of proceeding without intermediate functional models for intermediate model verification purposes.

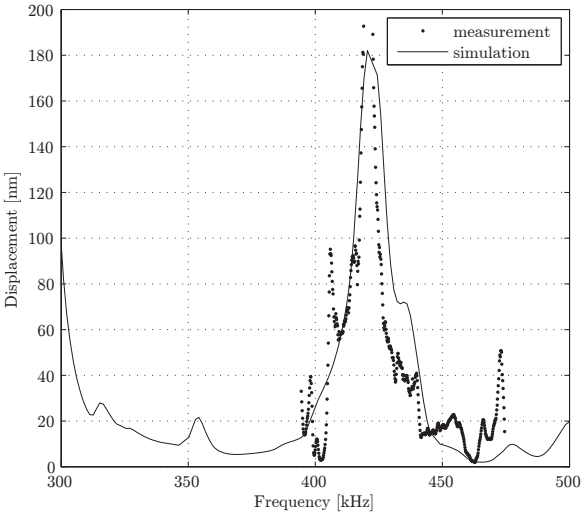

Figure 6.38. *Axial displacement of a surface point at the interface of two electrode portions*

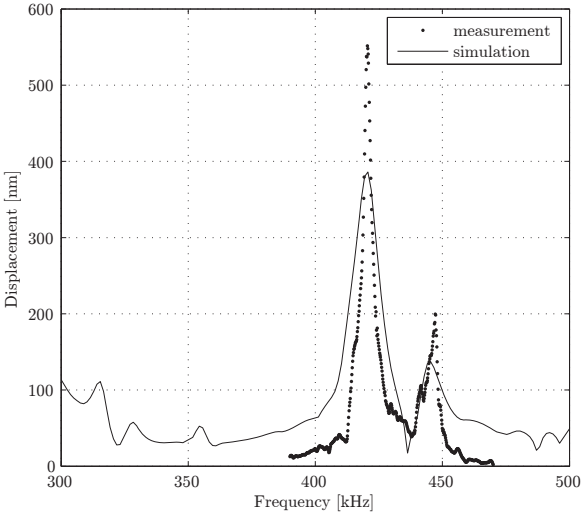

Figure 6.39. *Tangential displacement of a surface point at the interface of two electrode portions*

6.6.6 Position Sensor

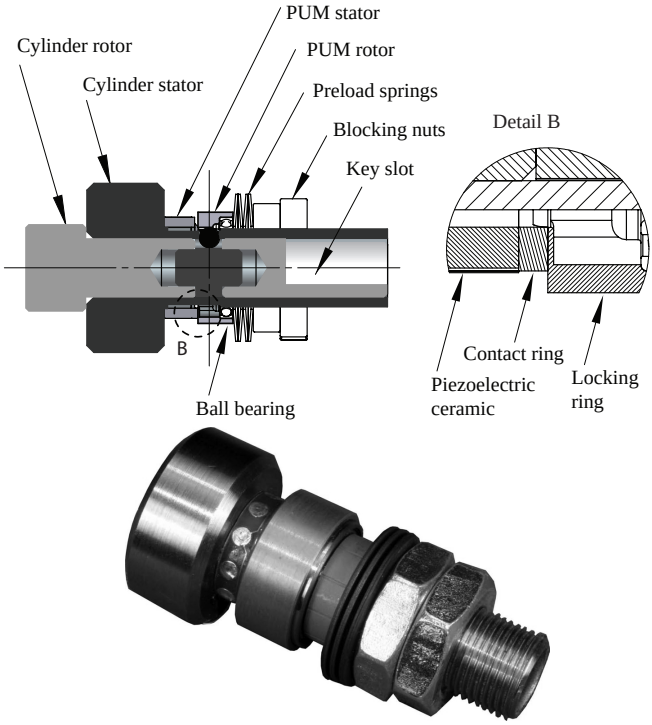

Figure 6.40. *Configuration of the piezoelectric locking device. Top: CAD model with steering curve for the locking bolts. Bottom: Functional model*

As shown in Fig. 6.40 the rotor structure inhibits a steering curve designed to move the locking bolts. This steering curve presents angular variations depending on the number of locking bolts it is designed for. It may now be conceived in a way that the resulting motional admittance modulation which is an image of the steering curve can be sensed by the drive electronics. In concrete terms, it was explained that the vibratory motion of the stator is transformed to a continuous rotor motion by frictional coupling at the contact points. During this process, the rotor material is displaced by the stator impact around the contact points. Because the resonance frequency of the rotor is distinct from the one of the stator, no Eigen mode is excited in the rotor. Therefore, the moving mass seen by the piezoelectric element depends on the position.

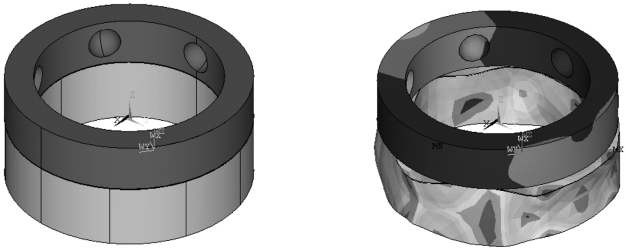

(a) *Contact model*

(b) *Displacement of stator and rotor*

Figure 6.41. *Displacement of the standing wave PUM in FEM simulation*

The conditions for motional admittance modulation have been verified. First, a FEM analysis was used to show that no Eigen mode of the rotor is not excited when driven by the stator (Fig. 6.41). Hence, an effect as illustrated in Fig. 6.42 is expected and position detection resumes to measuring the admittance variation caused by the steering curve.

6.7 Conclusion

Concerning the FEM based optimisation methodology, the complementary design approach, using design of experiments in a preoptimisation stage before applying FEM optimisation algorithms to the motor model enables vibration amplitude maximisation. Calculation time of the optimisation process is considerably reduced as only significant parameters are used for optimisation and others excluded during preoptimisation. Furthermore, the variation range of the significant parameters can be narrowed. Functional models of linear motors corresponding to the initial, the preoptimised and the optimised geometry have been built and tested on an experimental stage. The comparison of their characteristics to the predictions from the FEM model validated the design methodology. It was then successfully applied to a rotary piezoelectric motor with a different working principle. In this case, implementing a model of the contact phenomenon between stator and rotor is not advisable for optimisation because of the important cost in calculation time for every optimisation iteration. Maximising directly output force or speed is therefore not possible with the chosen approach. Observing the vibration characteristics, however, enables us to find pertinent conclusions on the output characteristics of the motor. Once the optimal solution found, the simulation of the full model validates the optimisation

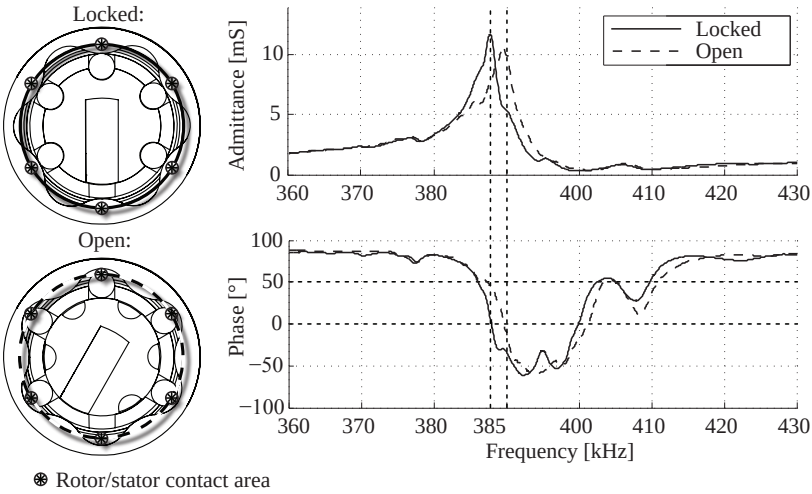

Figure 6.42. *Variation of the impedance characteristics as a function of the local moving mass*

results.

An attractive extension of the presented work will be to use the full 3D FEM model, taking into account the contact phenomenon between stator and rotor, in order to validate the optimisation results by a force and torque output as well as speed simulation. In concrete terms, the assumption that bigger axial and tangential displacement amplitudes mean higher torque and speed, respectively, does not take into account that output depends not only on the amplitude. The quality of the contact is indeed very important. Hence, the trajectory of a surface point of the stator under preload, as well as stick and slip phenomena would be interesting to investigate.

Because at the decisive level of the design process, not enough information was available in order to proceed with one single concept, two piezoelectric locking devices were designed. One is based on a linear OEM PUM, the Squiggle motor, the other is an original rotary design, where the developped PUM is based on an existing motor concept. Sensorless position controllers for both, the linear and the rotary locking device will be evaluated.

CHAPTER 7

Performance Evaluation and Validation

Contents

7.1 Motor Performance

An important design parameter for PUM is the preload wherewith the rotor is pressed against the stator. Although contact characteristics vary considerably

among the different PUM concepts (cf. Appendix A), some principal issues are of general validity.

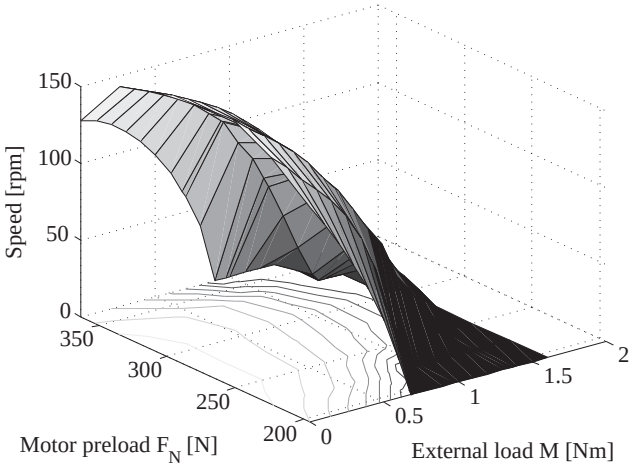

Figure 7.1. *Measurement of the mechanical output speed as a function of applied external load M for different preload conditions F_N [18].*

Figures 7.1 and 7.2 show the characteristics of the traveling wave ultrasonic motor. An optimal preload exists for every motor, depending on the working principle, the mechanical configuration, its dimensions, the contact materials and other factors. For the linear and rotary PUM developped in the frame of this project, no detailed preload analysis was performed. Firstly, an theoretical search of the optimal preload is not at reach, because it was not an intention of this thesis to obtain an analytical model of the contact phenomena. Secondly, at the functional model stage, it can not be expected to validate the optimal performances of the motor experimentally. The preload was therefore fixed experimentally for maximal speed.

7.2 Standing Wave Rotary PUM

Four series of 10 samples, 3^{rd} and 5^{th} mode types of each, the small and the large dimension, hence a total of 40 functional motor models were fabricated. Admittance analysis and interferometrical vibration measurements are compared to the FEM simulation results. Hereby we will be able to validate on the one hand the FEM models and on the other hand we will gain an insight into the importance of each fabrication step and the repeatability of the motor characteristics.

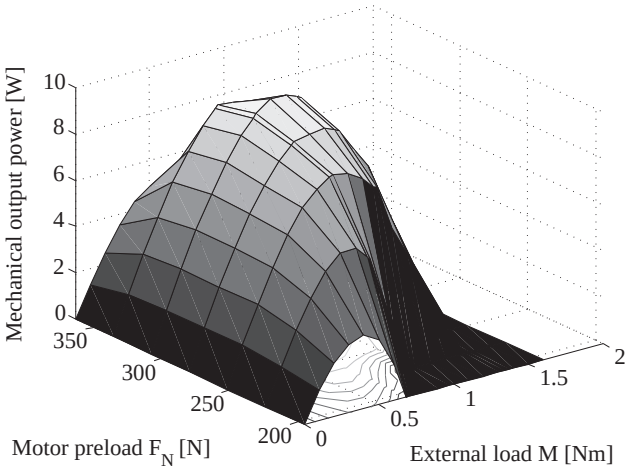

Figure 7.2. *Measurement of the mechanical output power as a function of applied external load M for different preload conditions F_N [18].*

7.2.1 Fabrication and Characterisation of Stators

In this section, the fabrication and characterisation of the stators is explained. A stator consists of a piezoceramic ring with an electrode for electric connectivity on its surface and a contact ring on its top plane for enhancing the properties of the friction contact with the rotor.

7.2.2 Electrodes

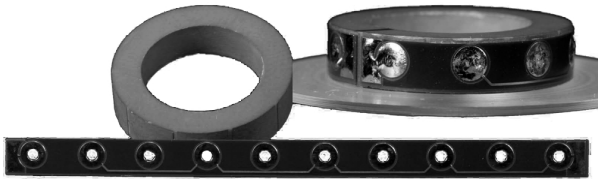

Figure 7.3. *The electrode is soldered to the Zn-Ni surface of the piezoceramic.*

Electrodes were brought onto the piezoelectric ceramic hollow cylinders by Zn-Ni flash coating. The division of the outer electrode groups was then achieved by milling. The inner surface is uniform and used as ground. The outer

surface is diveded into 6 or 10 sectors for the 3^{rd} mode and 5^{th} mode motors respectively. Then, two sets of 3 and 5 sectors respectively must be interconnected to form two phases. This is done soldering a flexible printed circuit board on the Zn-Ni surface as shown in Fig. 7.3.

7.2.3 Contact Rings

The contact rings must be connected to the piezoceramics in a virtually everlasting way. This connection must therefore be mechanical and thermic shock resistant and hazard persistent. Furthermore the connection must be as rigid as possible to reduce losses within the piezoceramic-metal interface at most. Because the piezoceramics must neither be machined nor heated above their Curie temperature, in order to preserve their piezoelectric properties, and cannott be constrained in any direction apart from the axial proload, bonding with adhesives is the natural selection.

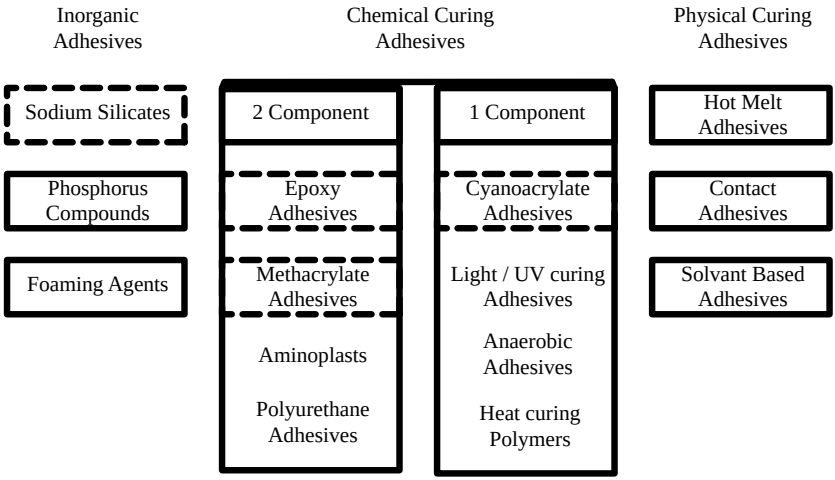

Figure 7.4. *Adhesive Classification. The dashed framed adhesives are tested.*

Yet, bonding metal to piezoceramics is a particularly challenging task because of the very different surface properties of these two material classes. There are two main criteria for adhesive selection. Firstly, the glue must connect the piezoceramic to the contact ring such that the vibrations are transmitted to the contact points with smallest possible losses. This may be expressed as lowest possible elasticity of the cured bond combined with sufficient resistance to the

stress induced by the high frequency vibrations. Secondly, the glue must resist to the hazards specified in the requirement specifications. The combination of the smooth metal surface to the porous piezoelectric ceramic presents a particular challenge. Among the tested products (Fig. 7.4), dedicated epoxies show the best results.

7.2.4 Stator Admittance Measurement

In order to identify eventual deterioration of the actuator properties during the manufacturing process, the admittance of each phase was measured after every production step. The setup to measure admittance between the inner surface and an electrode pattern consisting of three and five sectors respectively is shown in Fig. 7.5

Figure 7.5. *Admittance measurement setup with the Agilent 4294A Precision Impedance Analyzer (http://www.agilent.com) for the preloaded actuator.*

The electric connection was assured by spring mounted testing contacts in order to simulate a free piezoceramic ring.

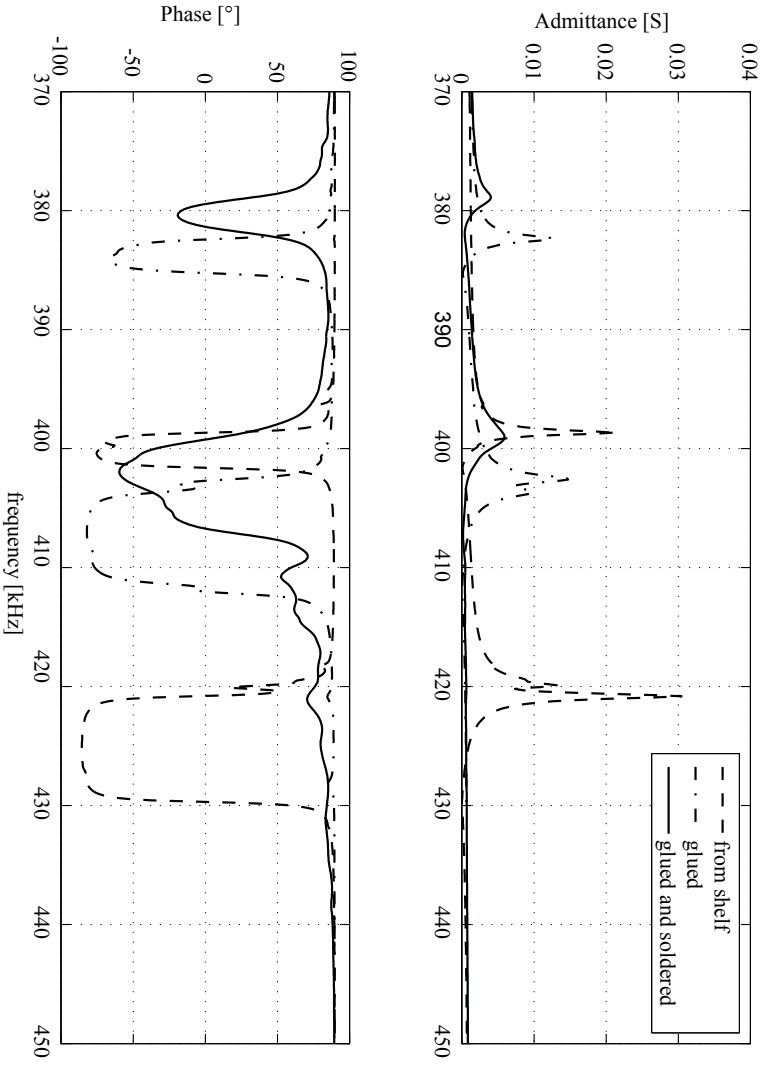

Figure 7.6. *Admittance evolution during the manufacturing process of the OD 18 3rd mode stators*

Measurement results

Fig. 7.6 shows the evolution of the admittance versus frequency during the manufacturing process (glueing and soldering) for a representative stator (OD18 3^{rd} mode). This representation shows clearly the influence of bonding the contact ring on the top plane and soldering the electrode around the surface of the piezoceramic tube. Through each of the steps, rigidity is increased and therefore the resonance frequency decreased. However, the influence of soldering to the frequency is minor. We can hence conclude that the electrode only negligibly deteriorates the piezoelectric characteristics of the ceramic hollow cylinders.

7.3 Driver

It has been shown that a minimised ripple or in other words minimal deviation from the ideal sinusoid of the drive voltage minimises wear and tear in the piezoelectric motor [235]. Besides the strive for maximal efficiency and miniaturisation, the sinusoidal nature of drive voltage and current were a central design criterion.

For validation, a LLCC configuration is implemented for the rotary motor, and a LC configuration for the Squiggle motor driver. Beeing arbitrary in fact, this choice has some justification, as the rotary motor operates with a single drive signal, whereas the Squiggle motor comes in a dual-phase configuration. The number of inductors is hence the same for both implementations and therefore the size of the driver is comparable.

A block diagram of the designed drive circuit representing the piezoelectric element with this electric equivalent circuit and indicating the values for the components is shown in Fig. 7.7.

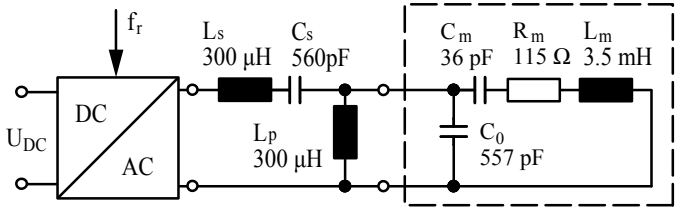

Figure 7.7. *Supply diagram with electric equivalent circuit for the piezoelectric element*

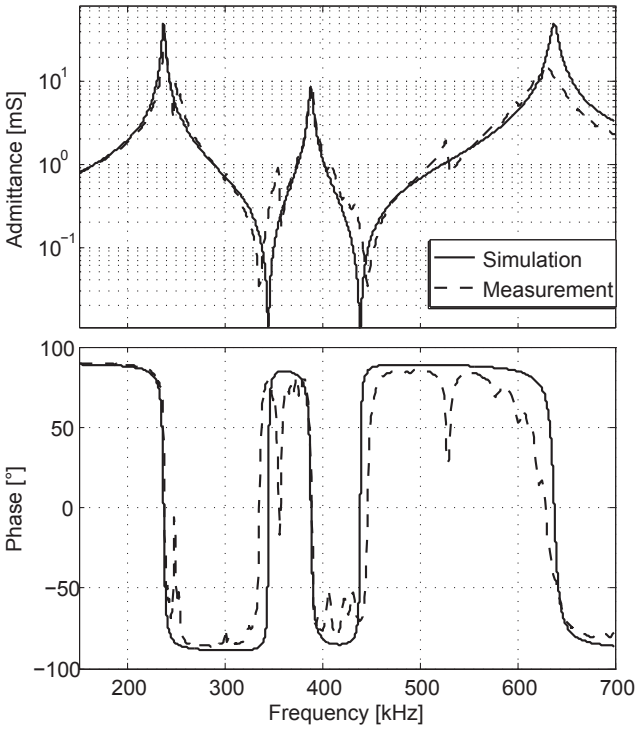

(a)

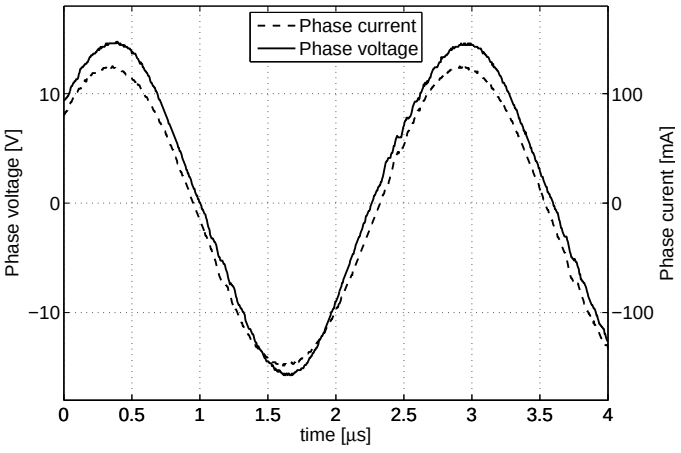

(b)

Figure 7.8. *a) Impedance characteristics of the standing wave PUM with LLCC resonant converter and b) the corresponding drive signals*

For model verification, the equivalent model parameters were measured. The corresponding plot in Fig. 7.8a compares the PSpice simulation of the electric equivalent circuit and the results of impedance analysis with an Agilent 4294A precision impedance analyzer. The measured steady state drive signals of the rotary motor are shown in Fig. 7.8b. These measurements correspond to the configuration illustrated with the electric equivalent model of Fig. 7.7 with the respective filter component and equivalent model values.

7.4 Sensorless Position Control

As we have seen, for an ultrasonic motor that is driven by a resonant converter, the electric resonance frequency of the drive circuit must match mechanical resonance of the piezoelectric actuator. In this case and with constant load and ambient conditions, power transmission to the piezoelectric element is maximal at the resonance frequency of the motor. Therefore, resonance frequency tracking is necessary when piezoelectric motors are used in harsh environment with large thermal gradients and important load variations, that modify the resonance frequency [50], [48].

Signal period and phase difference, voltage and current amplitude are detectable with the developped electronics setup which is explained in Fig. 6.6. Analyzing impedance characteristics and the mechanical resonance frequency of the motor, we see that an electrical resonance occurs at the same frequency as the mechanical resonance. It stands to reason that the proper drive frequency can be obtained by closing the control loop using the impedance phase angle. Also of importance is the actual phase angle that will produce the maximum amplitude. As we have seen, thanks to the resonance matching design, antiresonance disappears and the maximal vibration amplitude coincides with a phase angle of zero. We may therefore command the phase to zero in a feedback controller, which implies also, that the controller will naturally correct for the temperature and load effects because the impedance characteristics will follow the resonance frequency as it shifts.

Measuring the transient response of the controller, we see that the system is over-damped, stable and has zero steady state error due to the integration of the frequency signal. Even with a very high noise level, the system remains stable. This is a very useful feature of the controller because, due to the low drive signal levels, the phase measurement results indeed in a distorted and somewhat noisy signal.

In this way, the detected variation translates to an angular position dependant variation of the excitation frequency. At constant rotation speed, this variation becomes a time dependant signal close to a sinusoid as shown with the measure-

ment in Fig. 7.9. All indirect sensors were detected, which was checked with a Braun moviport C118 tachometer.

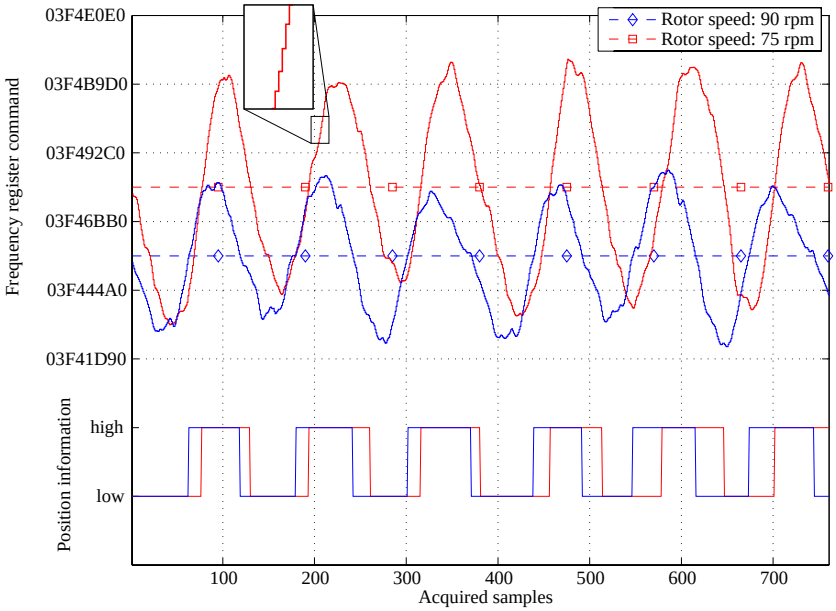

Figure 7.9. *Signal of the indirect position sensor.*

These results indicate the detectability of the locking position without direct position sensor. With an adaptive frequency controller, the variations of the admittance are detectable through distortion in excitation frequency. As seen from the practical test, the position detection method works for different rotation speeds. The hysteresis is fairly low. Indeed, the advantage of the method is that the evaluation is done entirely in the microprocessor implemented control loop and therefore the very small frequency variation of about 300 Hz at a resonance frequency of 386 kHz can be detected, which would be hardly possible with DAC and ADC interfaces.

7.4.1 Limitation

The MAM is not a standstill position detection method. A certain excitation level must be reached to visualise the effects on motional admittance. Therefore, no detection at low speed is possible, and we encounter similar limitations as in auto-commutated PM motors at start-up. Furthermore, the modifications

must match the contact nature. This is, in the case of a standing wave PUM, the number of equally spaced rotor variations must match the number of contact operators of the stator. If this is not the case, the effect is blurred out and detection made difficult. The method is therefore not transferable as is to other PUM concepts such as travelling wave motors.

7.5 Position Sensor for OEM PUM

The bumper impact detection was evaluated with the Squiggle motor. It must be ensured, that a bumper detection corresponds to a real bumper impact event. In other words, when the motor is blocked without having reached the bumper, the feedback to the door lock control must be failure instead of bumper impact. Reasons for blocking without having reached the bumper may be, first, malfunction due to electronics or connectivity problems. In this case, no signal indicating a bumper impact can be detected. Second, wear and tear may lead to a blocking of the motor. Third, external polluting agents may lead to a blocking of the motor. Assuming, that pollution that enters the lock housing is only in the size of dust and no large polluting materials may enter the lock housing, none of these events can lead to a condition creating bumper condition electric signals which may be misinterpreted. These considerations are true by analogy for the alternative solution where the thread is removed at the end of the rotor to indicate the end point (Fig. 7.10).

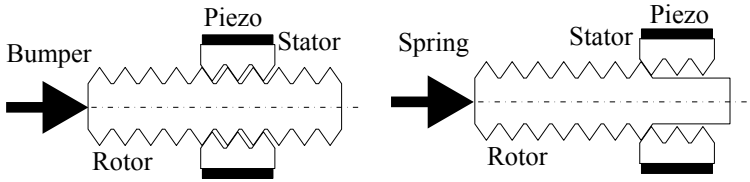

Figure 7.10. *Squiggle motor blocked due to a bumper or thread stop*

Then, the time variable signals were evaluated using the test bench. The variation of the phase shift between current and voltage, voltage amplitude and current amplitude are mesured (Fig. 7.11). In this way, end of motion range detection was demonstrated for the linear locking device.

The time constants of amplitudes on the one hand and phase shifts on the other hand differ in the measurements. This is explained by the fact that the phase shift is detected by the capture module of the DSC, whereas the amplitude

values are filtered before being fed to the ADC, and the filter time constant is therefore added to voltage and current amplitude.

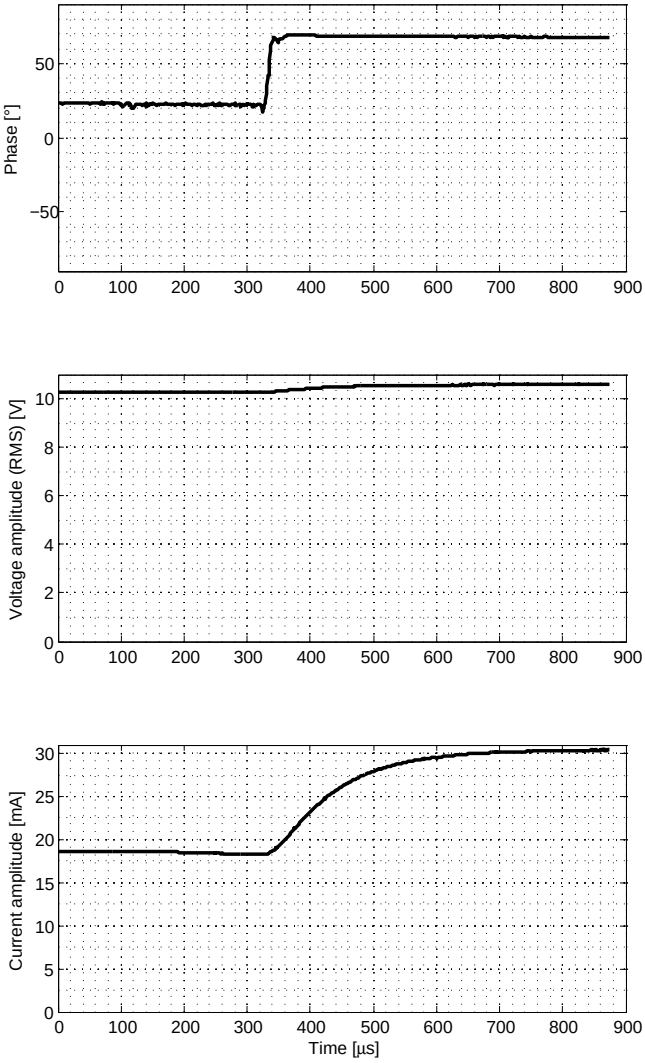

Figure 7.11. *End of motion range detection for the Squiggle motor*

The detected variations are equivalent for forward and reverse motion. Not only the collision with the bumper, but also the blocking of motion when moving in the wrong direction at the bumper is detectable. This may be helpful for designing a robust controller. Besides the results presented in this report, tests over 100'000 cycles indicate that life time of the motor is not reduced significantly by running it against a bumper. Furthermore, the proposed method also applies when the rotor is running against a spring or an equivalent shock absorbing equipment.

7.5.1 Limitations

First, it must be noted that the presented measurement results are obtained with very sensible measurement equipment. With respect to voltage, equivalent measurement results are possible with onboard components on a miniaturised driver card. However, the current measurement might be less accurate when miniaturised. Second, the indirect bumper sensor based on phase voltage and current measurements is applicable only in the case of the locking device and similar applications where the slider changes position without moving a high load. If high loads close to the nominal load of the motor or variable loads must be moved, the proposed method does not apply. Fig. 7.12 compares phase shift and current amplitude measurements.

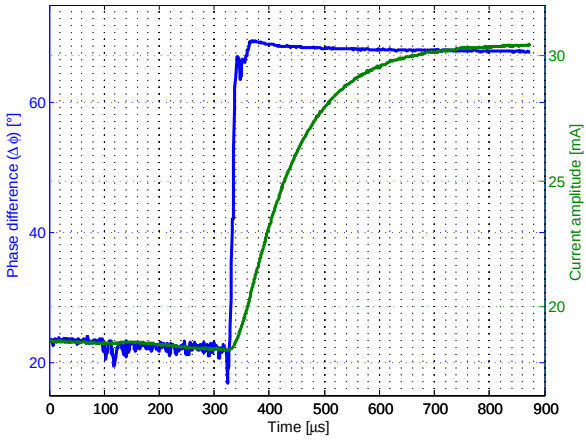

Figure 7.12. *Comparison of phase current amplitude and phase shift*

7.6 Conclusion

Both locking device concepts showed potential as sensors were replaced by indirect position detection methods and the integration of the system was improved. Concerning the industrial aspect of the work, the linear system was selected for commercialisation. The decisive criterion was risk management. The chance of success is much higher and the risk of premature failure after sale is considerably lower when relying on an existing product rather than developping a fundamentally new solution.

A limitation of the rotary motor is the involved wear and tear, due to the intrinsic friction drive characteristics, but also because of the locking concept. The torque could be increased by placing the pushers adequately as had been shown during the FEM based design process. Indeed, the angle between the pushers was fixed, hence placing them exactly at the interface of two electrode sections. This is because for a unidirectional motor, the new factor of axial and tangential displacement due to a slight radial dislocation of the pusher may be interesting. However, for bidirectional operation, an obtained positive effect for clockwise rotation would prove negative during counterclockwise rotation and symmetry would be lost. For the locking device application, the loss of bidirectionality is not necessarily a problem in the current design, because the rotor can rotate always in the same direction, stopping at the right (locked/closed) position without reversing its direction of rotation.

CHAPTER 8

Conclusion

This thesis addressed the research of indirect frequency tracking and position control methods for PUM. The current state of the art in sensorless control for PUM was evaluated in terms of the research objectives, indirect sensors as well as mechatronic system design. As a response to the three main issues identified in this process, geometrically simple, single phase PUM drivable from battery supply and featuring sensorless position control were developed.

Choosing a mechatronic conception of the problem, design models for the electromechanical conversion, the drive and control electronics, the mechanics and finally the implementation of digital control were put into relation with an equivalent electric model. Thereby, the latter one served as core model for the global design process, developping a particular view for every individual function, most notably:

- A FEM based methodology for the optimal design of piezoelectric stators,
- Numerical models of the drive electronics with a detailed load representation to find the most favourable drive configuration,
- A simplified analytical representation of integrated indirect position sensors, which was exploited in digital control for closed-loop position control.

Finally, optimal working point tracking and position controllers were tested along with the performance of functional models of linear and rotary PUM. The comprehensive analysis of design issues along with the test results provided a thoroughgoing understanding of the crucial elements in sensorless PUM control. A number of conclusions can be drawn.

A complete FEM model including the stator, rotor and the integrated sensors of a PUM turned out to be too complex for optimisation. All the more, the proposed combination of the quantitative approach with a qualitative evaluation of the contact phenomena at the stator/rotor interface allows to design PUM without referring to functional models in an iterative design process.

Digital control enables the succesful implementation of sensorless control strategies presented earlier [148], which at that time were judged difficult to implement in analog control.

Best position control results are obtained when the PUM is designed for self-sensing. Yet, indirect sensors also enable good position control results for OEM motors within some clearly defined boundary conditions and for well defined applications. In concrete terms, some specific issues such as indirect end range bumper detection can be achieved. However, position detection with very high resolution may not be obtained using the suggested methods.

Batch fabrication is a very delicate procedure and multitudinous factors influence the performance of the final product. In order to evaluate this, test series of functional models were produced. The results highlighted that, even with tight process control, standard deviation of performance of the PUM is considerable. Therefore, optimal working point tracking is necessary for efficient and reliable PUM operation.

8.1 Contributions

The multidisciplinar system approach is the strength of this thesis. A global view, aiming for coherence and covering the entire set of technologies involved in a mechatronic device driven by PUM was established. This chosen strategy responds to a demand of mechatronic industry which strives for integrated solutions bluring the borders between mechanics, electronics and information technology.

The particular contributions are:

- The design process is based on a core model, that develops simplified views of the involved techniques in order to interrelate all functions of a mechatronic system. Sensorless position controller design on this basis is shown to be possible.

- Integration of optimal working point tracking controllers with position controllers was achieved without compromising the efficiency and other properties of the PUM. Resonance frequency is tracked and position is sensed by interpreting the frequency command variable within the digital control loop.

- However, for these solutions, design for self-sensing is necessary and rather complex. Therefore, alternative approaches applicable to OEM motors were evaluated. Blocking at the desired position by a flexible bumper is detected via the control electronics by using simply a shunt resistor and comparator for current sensing. Unreliable end-range detection sensors can be replaced thereby.

- A FEM based optimisation methodology was successfully applied to new and existing motor concepts. The combination of numerical stator models and simplified analytical contact models allows for predicting correctly the qualitative output characteristics of the PUM.

- Digital control techniques enabled the successful implementation of indirect position detection methods, which were considered unreliable in earlier work, where analog electronics were used for the purpose.

8.2 Further Research

Certainly, the universal discourse, which is the strength of this thesis work, has the reverse side that no in-depth study of the particular technologies is provided. Thus, it is judicious to enlarge upon various aspects of the technologies that were treated.

Concerning sensorless control of PUM, the final aim clearly must be a linearised analytical model of the the stator/rotor contact phenomena. With respect to the rotary PUM, modelling precisely the local admittance modulation through mass and rigidity variations of the rotor used as indirect sensors, for instance, would lay the basis for a position observer using Kalman filters alike the acquired methods in the field of stepper motor control [154]. Furthermore, a linearised analytical model of the admittance modulation, would allow for implementing advanced optimal and robust controllers. Additionally, standstill position detection is an unsolved issue.

An extension would be to develop an optimisation and control model on the basis of existing analytical design models in order to obtain a core model, which is developable to an optimisation model and a control model at the same time. In

this way a continuous and really integrated approach to design for self-sensing would come into reach.

Another related route present FEM contact models of PUM. The existing models are too complex to be used for motor optimisation.

An interesting direction for further investigation would be to develop an analytical model of the stator for optimisation. The procedure could be similar to what is done with the numerical model in this work, with a qualitative consideration of the complete motor, by approximating the contact phenomena in a similar way as has been presented.

Beyond the application to conventional mechatronic systems, sensorless position control could open new perspectives in neuroscience studies. Haptic interfaces employed in this research field use PUM because of their non-magnetic nature. However, for force-feedback control, PUM [49] or hybrid ultrasonic motor clutch actuators need sophisticated magnetic resonance imaging compatible position sensors [25]. These could be replaced by customised sensorless position controllers.

APPENDIX A

PUM classification

A.1 Piezoelectric Actuation Principles

Piezoelectric motors convert electric energy to continuous motion by two stages. Based on the converse piezoelectric effect, electric energy in converted to strain energy in the piezoelectric element, where time changing electric fields initiate vibration. The unidirectional movement is then induced to the rotor by frictional coupling [53]. As the piezoelectric coupling is well understood, the main challenge in designing a piezoelectric motor is to find a way to effectively exploit the vibrations generated by the active element [147]. The bibliographic study of the subject presented in this chapter contains a description of the various approaches to fulfil this function. The review is limited to the most current or most significant solutions and contains, in addition to a classification of piezoelectric motors, the elements necessary to compare the essential characteristics of each solution. A classification is given in Fig. A.1.

Because virtually every motor class shown therein can be implemented as linear or as rotary motor, in a first part, we will not explicit the form of output motion. The static part of the motor will be called stator, the moving part we call rotor, even if a translatory moving component is considered. Every piezoelectric ceramic element inherits a particular elastic vibration frequency depending on its shape and material properties. By applying an electric signal that alternates at a frequency corresponding to such an eigen mode, the piezoelectric element res-

Table A.1. *PUM classification by working principle. Φ: Number of phases (total, active); F: Holding force (+ high, = moderate, - small); S: Speed (+ fast, = moderate, - slow)*

Working principle		Geometric configuration	Drive type	Φ	Contact type	F	S	Pioneering contributions rotary	linear
Standing wave	disc flexure	Disc with projections	intermittent	2,1	continuous	=	=	1986[82], '92[197]	1998[73]
	Phase Shift Stepping	Disc with projections	intermittent	x,1	continuous	=	=	1997 [138]	do
	Interrupted contact Stepping	Disc with projections	intermittent	2,1	continuous	=	-	1990[213]	none
	Bidimensional mode	Hollow cylinder	intermittent	2,1	continuous	=	+	1996[231]	2003[222]
Travelling wave	Surface	ring	continuous	2	continuous	+	=	1980[178], [177]	1998[77]
	Periphery	disc/ring	continuous	2	continuous	+	=	1986[88]	none
					regional	=	-	1986[88]	none
					local	-	-	1989[196]	none
Surface acoustic wave		surface/manifold	continuous	2	continuous	-	+	1995 [195]	do
Multimode	longitudinal-torsional	cylinder	intermittent	2	continuous	+	-	1989[142]	none
	longitudinal-bending	plate or cylinder	intermittent	2	local	-	+	1976[216], '08 [40]	1993[242]
Mode Conversion	longitudinal-torsional	cylinder	intermittent	1	regional	+	-	1985[106]	none
	longitudinal-bending	rod/manifold	intermittent	1	local	-	+	1990[141]	do
Elastic joint (metallic laminae) coupling		joint rings/plates	intermittent	1	local	-	+	1984 [218], '98[105]	1984[218]

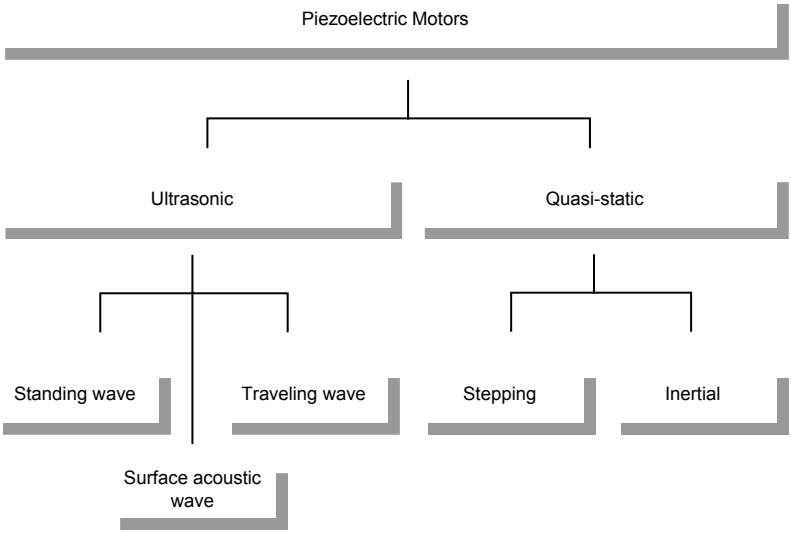

Figure A.1. *Classification of piezoelectric motors*

onates. This phenomenon is taken advantage of in many piezoelectric actuation devices, because at resonance the electro-mechanical coupling factor is maximal. The resonant modes may be classified as shown in Fig. A.2 for the shapes commonly used in piezoelectric actuators.

A.1.1 Ultrasonic Piezoelectric Actuation

Standing wave

The motion of standing wave motors is generated, as the designation indicates, by a wave which is stationary in the stator plane. The position of the wave nodes is determined by the position of the electrodes used to excite the piezoelectric element. Two fundamentally different ways to excite the stator motion are possible. The first concept, a bimodal piezoelectric ultrasonic resonator, is excited so as to create simultaneous longitudinal and bending standing waves. For instance, the first longitudinal mode and the second bending (flexural) mode combine to an elliptical motion of the surface points of a piezoelectric plate [216]. The second concept consists in exciting a single Eigen mode of a piezoelectric element in order to create translatory motions at one of its exterior surfaces. Often, the contact to the rotor is realised with pushers (Fig. A.3). When the stator is ex-

Vibration mode	Vibration mode associated to the shape
Radial	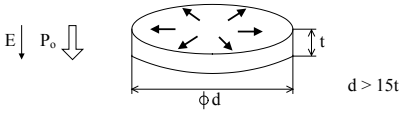 P_o : Polarisation direction E : Direction of the electric field
Transverse	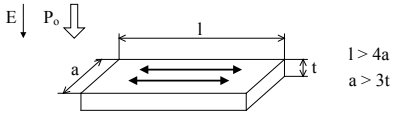
Longitudinal	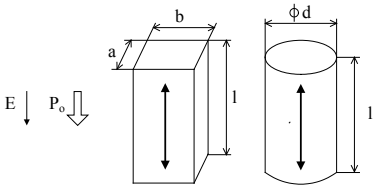 l > 2.5a, 2.5b, 2.5d
Thickness	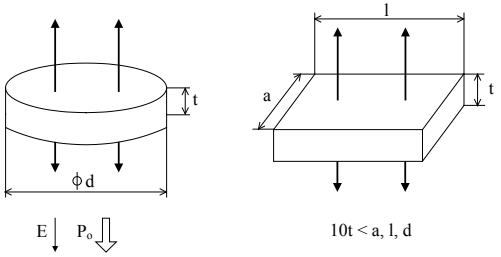
Shear	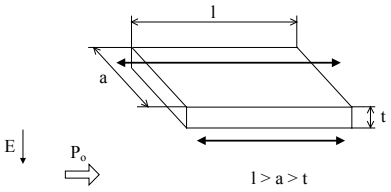

Figure A.2. *Typical vibration modes associated to the shape of piezoelectric ceramic elements [18].*

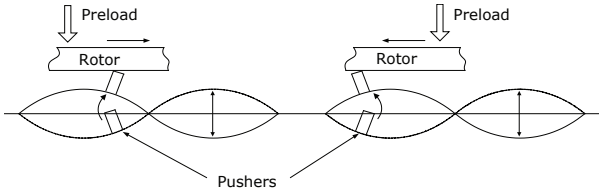

Figure A.3. *Working principle of a standing wave ultrasonic motor [73]*

cited, the vibration of the pushers actuates the rotor. The position of the pushers with respect to the nodes of the standing wave determines the direction of the movement. The speed of the moving part is proportional to the frequency of the eigen mode and the length of the pushers.

Travelling wave

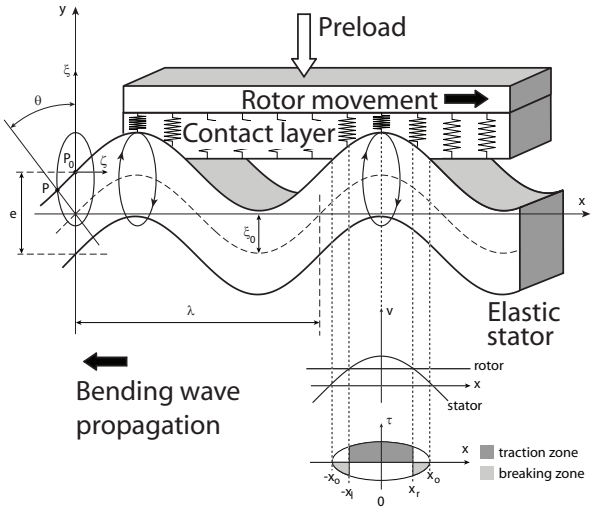

Figure A.4. *Working principle of a travelling wave ultrasonic motor [147]*

Driving a vibration source at one position of a closed ring excites a standing wave, because the displacements induced symmetrically on both sides of the excitation position interfere with each other. A travelling wave may therefore be generated by adding a second vibration source whose excitation is phase shifted

with respect to the first one. In this case, the two waves are superimposed and the wave pattern propagates around the ring. Fig. A.4 depicts schematically the operating principle of the travelling wave ultrasonic motor. The horizontal displacement ζ of a surface point P is approximatively given:

$$\zeta = -\pi\xi_0(\frac{e}{\lambda})\cos(\frac{2\pi x}{\lambda} - \omega_0 t) \tag{A.1}$$

where λ is the wave length of the progressive wave, e the stator height and ξ_0 the perpendicular displacement amplitude [147]. Thereby, the surface points of the stator follow an elliptical locus, being free in the direction of wave propagation and in contact with the rotor surface when propagating in the opposite sense (traction zone). This induces the rotor to move in the inverse direction with respect to the traveling wave.

Surface acoustic wave

The motion of the Rayleigh wave, a kind of surface acoustic wave, is illustrated in Fig. A.5. Each surface point in the elastic medium moves along an elliptical locus, because the Rayleigh wave is a coupled wave of the longitudinal wave and the shear wave which has normal displacement component to a boundary. The motion of the surface is similar to the flexural wave, therefore the Rayleigh wave is suitable for an ultrasonic motor. Conveniently, the wave motion is attenuated in the thickness direction, hence permitting rigid mounting at the bottom of the substrate [107].

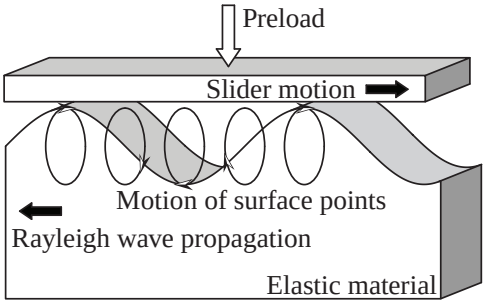

Figure A.5. *Working principle of a surface acoustic wave motor*

A.1.2 Quasistatic Actuation

Quasistatic piezoelectric motors operate below the resonance frequency of their piezoceramic actuators.

Inertial drives

Inertial drives use the difference between the static and dynamic friction coefficient at the stator-rotor contact interface. During the slower displacement of the actuator in the drive direction, the rotor follows the actuator with no slippage. Then, the actuator moves in the opposite direction rapidly enough to overcome friction and hence slips back beneath the rotor without moving it. This impulse principle combines high resolution with large strokes through the repetition of many small steps of a short range actuator. Generally inertial drives are divided into *stick-slip drives* and *impact drives*. They are both driven with an asymmetric - typically a sawtooth - signal, which causes their motion to consist of a *stick* and a *slip* phase. The fundamental difference between these two driving principles is that the rotor mass is very small for stick-slip drives and rather big for impact drives [16].

Stepping drives

In stepping drives, the rotor is passed hand-over-hand between either clamping and driving actuators or the teeth of a solid stator [193].

APPENDIX B

Fundamentals of Piezoelectricity

B.1 Symmetric Tensors in Crystallography

Using the Voigt notation we are able to simplify considerably the constitutive equations of piezoelectricity by exploiting symmetry.

Generally D and E are vectors, that is, Cartesian tensors of rank 1; and permittivity ϵ is a Cartesian tensor of rank 2. Strain and stress are, in principle, also rank 2 tensors. Exploiting symmetry of the strain tensor

$$\boldsymbol{\varepsilon} = \begin{pmatrix} \varepsilon_{xx} & \varepsilon_{xy} & \varepsilon_{xz} \\ \varepsilon_{yx} & \varepsilon_{yy} & \varepsilon_{yz} \\ \varepsilon_{zx} & \varepsilon_{zy} & \varepsilon_{zz} \end{pmatrix} \tag{B.1}$$

define

$$\boldsymbol{S} = (\varepsilon_{xx}, \varepsilon_{yy}, \varepsilon_{zz}, 2\varepsilon_{yz}, 2\varepsilon_{xz}, 2\varepsilon_{xy}). \tag{B.2}$$

For the stress tensor

$$\boldsymbol{\sigma} = \begin{pmatrix} \sigma_{xx} & \sigma_{xy} & \sigma_{xz} \\ \sigma_{yx} & \sigma_{yy} & \sigma_{yz} \\ \sigma_{zx} & \sigma_{zy} & \sigma_{zz} \end{pmatrix} \tag{B.3}$$

$$\boldsymbol{T} = (\sigma_{xx}, \sigma_{yy}, \sigma_{zz}, \sigma_{yz}, \sigma_{xz}, \sigma_{xy}). \tag{B.4}$$

The factor 2 is due to the fact that the scalar product equals the inner product of stress and strain tensors:

$$\boldsymbol{S} \cdot \boldsymbol{T} = \boldsymbol{\varepsilon} \cdot \boldsymbol{\sigma} = \varepsilon_{ij}\sigma_{ij} \quad \text{with} \quad i, j = x, y, z. \tag{B.5}$$

That is why $\boldsymbol{S}$ and $\boldsymbol{T}$ appear as 6 element vectors. Consequently, s is written as a 6x6 matrix in place of a rank 4 tensor.

The constitutive equations write therefore in the Voigt notation

$$\begin{pmatrix} S_1 \\ S_2 \\ S_3 \\ S_4 \\ S_5 \\ S_6 \end{pmatrix} = \begin{pmatrix} s_{11}^E & s_{12}^E & s_{13}^E & 0 & 0 & 0 \\ s_{21}^E & s_{22}^E & s_{23}^E & 0 & 0 & 0 \\ s_{31}^E & s_{32}^E & s_{33}^E & 0 & 0 & 0 \\ 0 & 0 & 0 & s_{44}^E & 0 & 0 \\ 0 & 0 & 0 & 0 & s_{55}^E & 0 \\ 0 & 0 & 0 & 0 & 0 & s_{66}^E \end{pmatrix} \begin{pmatrix} T_1 \\ T_2 \\ T_3 \\ T_4 \\ T_5 \\ T_6 \end{pmatrix} + \tag{B.6}$$

$$+ \begin{pmatrix} 0 & 0 & d_{31} \\ 0 & 0 & d_{32} \\ 0 & 0 & d_{33} \\ 0 & d_{24} & 0 \\ d_{15} & 0 & 0 \\ 0 & 0 & 0 \end{pmatrix} \begin{pmatrix} E_1 \\ E_2 \\ E_3 \end{pmatrix} \tag{B.7}$$

$$\begin{pmatrix} D_1 \\ D_2 \\ D_3 \end{pmatrix} = \begin{pmatrix} 0 & 0 & 0 & 0 & d_{15} & 0 \\ 0 & 0 & 0 & d_{24} & 0 & 0 \\ d_{31} & d_{32} & d_{33} & 0 & 0 & 0 \end{pmatrix} \begin{pmatrix} T_1 \\ T_2 \\ T_3 \\ T_4 \\ T_5 \\ T_6 \end{pmatrix} + \tag{B.8}$$

$$+ \begin{pmatrix} \varepsilon_{11} & 0 & 0 \\ 0 & \varepsilon_{22} & 0 \\ 0 & 0 & \varepsilon_{33} \end{pmatrix} \begin{pmatrix} E_1 \\ E_2 \\ E_3 \end{pmatrix} \tag{B.9}$$

where $s_{66}^E = 2\left(s_{11}^E - s_{12}^E\right)$ and the symmetric tensor $\boldsymbol{T}$ is defined with $\boldsymbol{V}$ a vector space and

$$T \in V^{\otimes r} \tag{B.10}$$

a tensor of order r. Then $\boldsymbol{T}$ is a symmetric tensor if

$$\tau_\sigma \boldsymbol{T} = \boldsymbol{T} \tag{B.11}$$

for the braiding maps associated to every permutation σ on the symbols $1, 2, ..., r$ or equivalently for every transposition on these symbols.

Given a basis e^i of $\boldsymbol{V}$, any symmetric tensor $\boldsymbol{T}$ of rank r can be written as

$$T = \sum_{i_1,...,i_r=1}^{N} T_{i_1 i_2 ... i_r} e^{i_1} \otimes e^{i_2} \otimes \cdots \otimes e^{i_r} \tag{B.12}$$

for some unique list of coefficients $\boldsymbol{T_{i_1 i_2 ... i_r}}$ (the components of the tensor in the basis) that are symmetric on the indices. That is to say

$T_{i_{\sigma 1} i_{\sigma 2} ... i_{\sigma r}} = T_{i_1 i_2 ... i_r}$

for every permutation σ [108] [84] [205].

B.2 Formulation of Piezoelectricity for FEM

The differential equations describing the piezoelectric effect are solved numerically in this work using Ansys. The solution for nodal displacement is obtained with Ansys. In concrete terms, a voltage is applied as constraint to the nodes of the FEM model of the piezoelectric element. Defining a set of coupled degrees of freedom using the *CP* command and the electric label *VOLT* does this. An amplitude value is then attributed to the voltage variable.

To model a PUM, the following assumptions are made:

- The piezoceramic actuator is in direct contact and immobile in reference to the resonator. The glue is taken into account by adjusting the damping factor of the resonator system.

- The electrodes glued or soldered on the piezoceramics are not modeled physically. It is supposed that the outer surfaces of the piezoceramic are on positive and that the inner surface is on negative electrical potential.

- The surface points of the resonator that are in contact with the rotor are supposed to move freely.

B.2.1 Modal Analysis

Modal analysis is the study of the dynamic properties of structures under vibrational excitation. From the numerical point of view, it consists in solving the equation of eigenvalues (B.13). This is done using the Householder-bisection-inverse iteration. Because near resonance, damping can be neglected, the system is considered undamped for the modal analysis.

$$\boldsymbol{K}_{\xi\xi}\boldsymbol{\Phi}_i = \omega_i^2 \boldsymbol{M}\boldsymbol{\Phi}_i \tag{B.13}$$

The unknown variables in this problem formulation are the Eigenwert ω_i and the Eigen vector Φ_i.

B.2.2 Static Analysis

The static analysis is not approached directly with Ansys, but by applying potentials and forces to selected nodes of the numerical model. The software rearranges these electromechanical boundary conditions and solves the linear equation of statics (B.14).

$$\boldsymbol{K}_{\xi\xi}\boldsymbol{\xi} = \boldsymbol{F} \tag{B.14}$$

B.2.3 Harmonic Response Analysis

Any sustained cyclic load will produce a sustained cyclic response in a structural system. The harmonic response analysis predicts the sustained dynamic behaviour of the system, which is the steady-state response to loads that vary sinusoidally with time. The idea of the FEM based approach is to calculate the structure's response at several frequencies and obtain a graph of displacements versus frequency. Response maxima are then identified on the graph and stresses reviewed at those peak frequencies.

Starting from the general equation of motion for the structural system (B.15)

$$\boldsymbol{M}\ddot{\boldsymbol{\xi}} + \boldsymbol{C}\dot{\boldsymbol{\xi}} + \boldsymbol{K}\boldsymbol{\xi} = \boldsymbol{F}(\boldsymbol{t}) \tag{B.15}$$

and assuming that all points in the structure move at the same known frequency, however, not necessarily in phase, the displacements are defined as:

$$\boldsymbol{\xi} = \boldsymbol{\xi}_{max} e^{j\phi} e^{j\Omega t} \tag{B.16}$$

The force vector is defined analogously to the displacement:

$$\boldsymbol{F} = \boldsymbol{F}_{max} e^{j\psi} e^{j\Omega t} \tag{B.17}$$

Plugging Equations (B.16) and (B.17) into (B.15) yields:

$$\left(\boldsymbol{K} - \Omega^2 \boldsymbol{M} + j\Omega \boldsymbol{C}\right) \left(\boldsymbol{\xi}_{max}(\cos\phi + j\sin\phi)\right) = \boldsymbol{F}_{max}(\cos\psi + j\sin\psi) \tag{B.18}$$

A wavefront algorithm is used to solve these equations.

B.2.4 Transient Analysis

The harmonic analysis calculating only the steady-state, forced vibrations of a structure, the transient vibrations, which occur at the beginning of the excitation, must be evaluated seperately.

APPENDIX C

Material Data

C.1 Pz26 by Ferroperm

Stiffness matrix:

$$c^E = \begin{bmatrix} 16.8 & 11.0 & 9.99 & 0 & 0 & 0 \\ & 16.8 & 11.0 & 0 & 0 & 0 \\ & & 12.3 & 0 & 0 & 0 \\ & & & 3.01 & 0 & 0 \\ & & & & 3.01 & 0 \\ & & & & & 2.88 \end{bmatrix} \cdot 10^{10} N/m^2 \quad \text{(C.1)}$$

Piezoelectric charge constants:

$$d = \begin{bmatrix} 0 & 0 & 0 & 0 & 3.27 & 0 \\ 0 & 0 & 0 & 3.27 & 0 & 0 \\ -1.28 & -1.28 & 3.28 & 0 & 0 & 0 \end{bmatrix} \cdot 10^{-10} C/m^2 \quad \text{(C.2)}$$

Permittivity:

$$\epsilon^S_{1,r}, \epsilon^S_{2,r} = 8.28 \cdot 10^2 \quad \textbf{[-]} \quad \text{(C.3)}$$

$$\epsilon^S_{3,r} = 7.00 \cdot 10^2 \quad \textbf{[-]} \tag{C.4}$$

Curie Temperature: $T_c > 330°$

Density: $\rho = 7700\ kg/m^3$

C.2 PZT-8 Corresponding to EBL Piezoceramics

Stiffness matrix:

$$c^E = \begin{bmatrix} 14.7 & 8.11 & 8.11 & 0 & 0 & 0 \\ & 14.7 & 8.11 & 0 & 0 & 0 \\ & & 13.2 & 0 & 0 & 0 \\ & & & 3.13 & 0 & 0 \\ & & & & 3.13 & 0 \\ & & & & & 3.29 \end{bmatrix} \cdot 10^{10}\ N/m^2.$$

Piezoelectric constants:

$$e = \begin{bmatrix} 0 & 0 & 0 & 0 & 10.34 & 0 \\ 0 & 0 & 0 & 10.34 & 0 & 0 \\ -3.87 & -3.87 & 13.91 & 0 & 0 & 0 \end{bmatrix}\ As/m^2.$$

Dielectric constants:

$$\epsilon^T = \begin{bmatrix} 1.14 & 0 & 0 \\ 0 & 1.14 & 0 \\ 0 & 0 & 0.89 \end{bmatrix} \cdot 10^{-8}\ As/Vm.$$

Density: $\rho = 7600\ kg/m^3$.

APPENDIX D

Mechanical Drawing

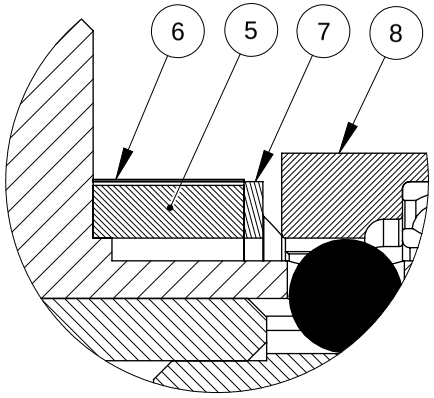

DETAIL C
(5:1)

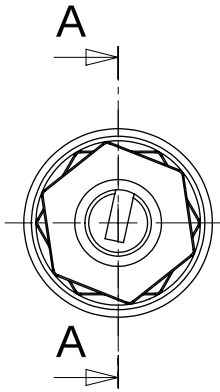

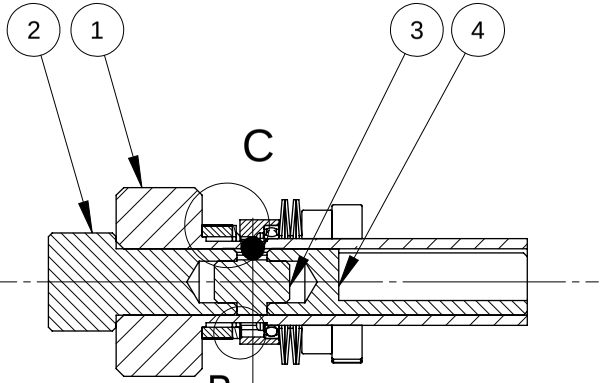

A-A

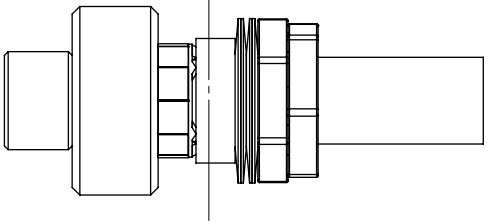

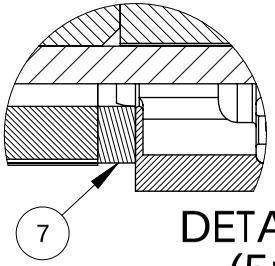

DETAIL B
(5:1)

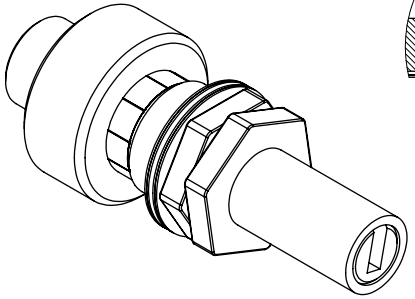

-	-	Piezoelectric locking device	-
Pos	Nb	Denomination	Material

Without seperate denomination		Nom	Date	Project	Scale
Denomination with same nb.	Drawing	M. Flückiger	22-10-2008	8821.1 EPRP-IW	1:1
Denomination with de: erent nb.	Controlled				
EPFL ÉCOLE POLYTECHNIQUE FÉDÉRALE DE LAUSANNE — Integrated Actuators Laboratory (LAI)			Paper A5	Drawing number 1000	

Bibliography

[1] K. Agbossou, J.-L. Dion, S. Carignan, M. Abdelkrim, and A. Cheriti. Class D amplifier for a power piezoelectric load. *Ultrasonics, Ferroelectrics and Frequency Control, IEEE Transactions on*, 47(4):1036 – 1041, jul 2000.

[2] Y. Ang, M. Foster, H. Sewell, C. Bingham, and D. Stone. Stress analysis of fourth-order LLCC resonant converters. *Electronics Letters*, 38(24):1585 – 1586, nov 2002.

[3] Ansys Inc., Canonsburg, PA. *Theory Reference for ANSYS and ANSYS Workbench*, ANSYS Release 11.0 edition, 2007. User manual.

[4] L. Antognini. *Réglage et commande de moteurs pas à pas*. PhD thesis, Ecole Polytechnique Fédérale de Lausanne, 1984.

[5] J. Aragones and J. Robineau. Method and control device for the speed of rotation of a piezoelectric motor rotor, 2008. International patent.

[6] Arndt. Piezoelectric transducer, 1947. US Patent 2423922.

[7] H. V. Barth. Ultrasonic driven motor. *IBM Technical Disclosure Bulletin 16*, 7, 1973.

[8] D. M. Bates and D. G. Watts. *Nonlinear Regression and Its Applications*. Wiley, New York, 1988.

[9] S. Ben-Yaakov and M. Peretz. A self-adjusting sinusoidal power source suitable for driving capacitive loads. *Power Electronics, IEEE Transactions on*, 21(4):890–898, July 2006.

[10] S. Ben-Yaakov, E. Rozanov, T. Wasserman, T. Rafaeli, L. Shiv, and G. Ivensky. A resonant driver for a piezoelectric motor with single transistor direction switches. In *Applied Power Electronics Conference and Exposition, 2000. APEC 2000. Fifteenth Annual IEEE*, volume 2, pages 1037–1043 vol.2, 2000.

[11] M. Berg, P. Hagedorn, and S. Gutschmidt. On the dynamics of piezoelectric cylindrical shells. *Journal of Sound and Vibration*, 274(1-2):91 – 109, 2004.

[12] H. Bühler. *Convertisseurs Statiques*. Presses Polytechniques et Universitaires Romandes, 1991.

[13] M. Boukhnifer, A. Chaibet, and C. Larouci. Fault tolerant control of piezoelectric traveling wave ultrasonic motor. In *Control Applications, (CCA) & Intelligent Control, (ISIC), 2009 IEEE*, pages 1350–1355, July 2009.

[14] M. Boukhnifer, A. Chaibet, and C. Larouci. A robust speed control architecture for ultrasonic motor. In *Industrial Electronics, 2009. IECON '09. 35th Annual Conference of IEEE*, pages 1409 –1414, nov. 2009.

[15] G. Box, W. Hunter, and J. Hunter. *Statistics for Experimenters, An introduction to design, data analysis and model building*. Wiley, 1978.

[16] J.-M. Breguet. *Actionneurs "stick and slip" pour micro-manipulateurs*. PhD thesis, Ecole Polytechnique Fédérale de Lausanne, 1998.

[17] R. Briot, M. M. Guillemot-Amadei, A. Pelourson, and C. Garabedian. Generators for piezoelectric motors. *Measurement Science and Technology*, 4(9):938, 1993.

[18] M. Bullo. *Modélisation et commande du moteur piézoélectrique à onde progressive*. PhD thesis, Ecole Polytechnique Fédérale de Lausanne, Switzerland, September 2005.

[19] W. G. Cady. *Piezoelectricity : an introduction to the theory and applications of electromechanical phenomena in crystals*, volume XXIII of *International series in pure and applied physics*. McGraw-Hill, New York, first edition, 1946.

[20] J. Callahan and H. Baruh. Modal sensing of circular cylindrical shells using segmented piezoelectric elements. *Smart Materials and Structures*, 8(1):125–135, 1999.

[21] R. Canfield, C. Henderson Jr., D. Cory-Slechta, C. Cox, T. Jusko, and B. Lanphear. Intellectual impairment in children with blood lead concentrations below 10 μg per deciliter. *New England Journal of Medicine*, 348(16):1517–1526, 2003.

[22] S. Canfield and M. Frecker. Topology optimization of compliant mechanical amplifiers for piezoelectric actuators. *Structural and Multidisciplinary Optimization*, 20(4):269–279, Dec. 2000.

[23] K. Carazo, A.V.adn Uchino. Novel piezoelectric-based power supply for driving piezoelectric actuators designed for active vibration damping applications. *Journal of Electroceramics*, 7(3):197–210, 2001.

[24] A. Cassat. *Etude numérique des caractéristiques statiques et du comportement dynamique des moteurs pas à pas polyphasés*. PhD thesis, Ecole Polytéchnique Fédérale de Lausanne, 1977.

[25] D. Chapuis. *Application of ultrasonic motors to MR-compatible haptic interfaces.* PhD thesis, Ecole Polytechnique Fédérale de Lausanne, 2009.

[26] J.-D. Chatelain and R. Dessoulavy. *Electronique*, volume VIII of *Traité d'Electricité*. Presses Polytechniques et Universitaires Romandes, 1995.

[27] K. Chau, B. Shi, and M.-Q. Hu. A new design method and half-step operation for ultrasonic stepping motors. *Industry Applications, IEEE Transactions on*, 39(4):953–960, 2003.

[28] C.-T. Chen. Extensions of the topsis for group decision-making under fuzzy environment. *Fuzzy Sets and Systems*, 114(1):1 – 9, 2000.

[29] S. Chevailler. *Comparative study and selection criteria of linear motors*. PhD thesis, Ecole Polytechnique Fédérale de Lausanne (EPFL), Lausanne, 2006.

[30] G. S. Choi, Y. A. Lim, and G. H. Choi. Tracking position control of piezoelectric actuators for periodic reference inputs. *Mechatronics*, 12(5):669 – 684, 2002.

[31] C.-L. Chu and S.-H. Fan. A novel long-travel piezoelectric-driven linear nanopositioning stage. *Precision Engineering*, 30(1):85 – 95, 2006.

[32] X.-c. Chu, J.-f. Wu, L.-t. Li, L. Zhong, and S.-x. Zhao. Preparation of lead free KNLNTS piezoelectric ceramics by molten salt synthesis and its application. In *Piezoelectricity, Acoustic Waves, and Device Applications, 2008. SPAWDA 2008. Symposium on*, pages 519–523, Dec. 2008.

[33] M. Crivii and M. Jufer. DC to AC converters for piezoelectric motors. In *Proceedings of EPE'99*, 1999.

[34] J. Curie and P. Curie. Développement, par pression, de l'électricité polaire dans les cristaux hémièdres à faces inclinées. *Comptes rendus hebdomadaires des séances de l'Académie des sciences*, 91:294–295, 1880.

[35] J. Curie and P. Curie. Contractions et dilatations produites par des tensions électriques dans les cristaux hémièdres à faces inclinées. *Comptes rendus hebdomadaires des séances de l'Académie des sciences*, 93:1137–1140, 1881.

[36] B. M. F. V. Dehez. *Elaboration et application d'une approche multidisciplinaire pour la conception d'un actionneur électrique à rotor sphérique*. PhD thesis, Université catholique de Louvain, 2004.

[37] A. Delehelle. *Etude d'un concept innovant d'actionneur électromécanique linéaire à effets magnétiques et piézoélectrique en vue d'applications dans le domaine des commandes de vol*. PhD thesis, Université de Toulouse, 2008.

[38] E. Dieulesaint, D. Royer, D. Mazeroue, and P. Nowak. Piezoelectric transformers. *Electronics Letters*, 24(7):444–445, Mar 1988.

[39] Y. Doshida, H. Kishi, A. Makiya, S. Tanaka, K. Uematsu, and T. Kimura. Crystal-oriented La-substituted $Sr_2NaNb_5O_{15}$ ceramics fabricated using high-magnetic-field method. *Japanese Journal of Applied Physics*, 45(9B):7460–7464, 2006.

[40] Y. Doshida, S. Kishimoto, T. Irieda, H. Tamura, Y. Tomikawa, and S. Hirose. Double-mode miniature cantilever-type ultrasonic motor using lead-free array-type multilayer piezoelectric ceramics. *Japanese Journal of Applied Physics*, 47(5):4242–4247, 2008.

[41] Y. Doshida, S. Kishimoto, K. Ishii, H. Kishi, H. Tamura, Y. Tomikawa, and S. Hirose. Miniature cantilever-type ultrasonic motor using pb-free multilayer piezoelectric ceramics. *Japanese Journal of Applied Physics*, 46(7B):4921–4925, 2007.

[42] W. H. Duan, S. T. Quek, and S. P. Lim. Finite element solution for intermittent-contact problem with piezoelectric actuation in ring type USM. *Finite Elem. Anal. Des.*, 43(3):193–205, 2007.

[43] W. H. Duan, S. T. Quek, and Q. Wang. A novel ring type ultrasonic motor with multiple wavenumbers: design, fabrication and characterization. *Smart Materials and Structures*, 18(12):125025, 2009.

[44] J. Fernandez and Y. Perriard. Optimization methodology for piezoelectric transformers design. In *Ultrasonics Symposium, 2007. IEEE*, pages 2539–2542, Oct. 2007.

[45] J. M. Fernandez, M. Flueckiger, and Y. Perriard. Study of a hollow ultrasonic rotary motor. In *2008 IEEE International Ultrasonics Symposium Proceedings*, pages 1449–1452, 2008.

[46] J. M. Fernandez and Y. Perriard. Optimization of a new type of ultrasonic linear motor. *Ultrasonics, Ferroelectrics and Frequency Control, IEEE Transactions on*, 55(3):659–667, 2008.

[47] J. Fernandez-Lopez. *Modeling and optimization of ultrasonic linear motors*. PhD thesis, EPFL, 2006.

[48] A. Ferreira. Optimized friction drive controller for a multi-dof ultrasonic nanopositioner. *Mechatronics, IEEE/ASME Transactions on*, 9(3):481–490, Sept. 2004.

[49] M. Flueckiger, M. Bullo, D. Chapuis, R. Gassert, and Y. Perriard. fmri compatible haptic interface actuated with traveling wave ultrasonic motor. In *Industry Applications Conference, 2005. Fourtieth IAS Annual Meeting. Conference Record of the 2005*, volume 3, pages 2075–2082 Vol. 3, 2005.

[50] M. Flueckiger, J. M. Fernandez, and Y. Perriard. Adaptive control of ultrasonic motors using the maximum power point tracking method. In *2008 IEEE International Ultrasonics Symposium Proceedings*, pages 1823 – 1826, 2008.

[51] A. Flynn and S. Sanders. Fundamental limits on energy transfer and circuit considerations for piezoelectric transformers. *Power Electronics, IEEE Transactions on*, 17(1):8–14, Jan 2002.

[52] A. Flynn, L. Tavrow, S. Bart, R. Brooks, D. Ehrlich, K. Udayakumar, and L. Cross. Piezoelectric micromotors for microrobots. In *Ultrasonics*

Symposium, 1990. Proceedings., IEEE 1990, pages 1163 –1172 vol.3, dec 1990.

[53] A. M. Flynn. *Piezoelectric Ultrasonic Micromotors*. PhD thesis, MIT Artificial Intelligence Laboratory, 1995.

[54] S. Furuya, T. Maruhashi, Y. Izuno, and M. Nakaoka. Load-adaptive frequency tracking control implementation of two-phase resonant inverter for ultrasonic motor. In *21st Annual IEEE Power Electronics Specialists Conference, 1990. PESC '90 Record.*, pages 17 –24, jun 1990.

[55] S.-i. Furuya, T. Maruhashi, Y. Izuno, and M. Nakaoka. Load-adaptive frequency tracking control implementation of two-phase resonant inverter for ultrasonic motor. *Power Electronics, IEEE Transactions on*, 7(3):542–550, 1992.

[56] C. F. Gallmeyer and L. G. Waterfield. Method and apparatus for controlling position and velocity of a piezoelectric device, 2001. US Patent 6285115.

[57] F. M. Gardner. *Phaselock Techniques*. Wiley, Hoboken, New Jersey, third edition, 2005.

[58] P. Germano and M. Jufer. Contactless power transmission : Frequency tuning by a maximum power tracking method. In *EPE'97 Trondheim*, volume 4, pages 693–697, 1997.

[59] F. Giraud and B. Lemaire-Semail. Causal modeling and identification of a travelling wave ultrasonic motor. *EPJ Applied Physics*, 21(2):151–159, 2003.

[60] F. Giraud and B. Semail. A torque estimator for a traveling wave ultrasonic motor - application to an active claw. *Ultrasonics, Ferroelectrics and Frequency Control, IEEE Transactions on*, 53:1468–1477, 2006.

[61] T. S. Glenn, K. Ghandi, M. J. Atalla, and N. W. Hagood. Mixed-domain traveling-wave motor model with lossy (complex) material properties. In V. S. Rao, editor, *Proc. SPIE*, volume 4326, pages 525–537. SPIE, 2001.

[62] J. Gouatarbes, M. Boukhnifer, A. Ferreira, D. Aubry, and P. Magnan. Robust control for ultrasonic motor operating within harsh environments. In *Advanced intelligent mechatronics, 2007 ieee/asme international conference on*, pages 1–6, Sept. 2007.

[63] R. B. Gray. Transducer and method making the same, 1946. US Patent 2486560.

[64] M. Guo, D. M. Lin, K. H. Lam, S. Wang, H. L. W. Chan, and X. Z. Zhao. A lead-free piezoelectric transformer in radial vibration modes. *Review of Scientific Instruments*, 78(3):035102, 2007.

[65] S. Gutschmidt and P. Hagedorn. A mathematical model for the start-up of an ultrasonic bar-type motor. In *Advanced Intelligent Mechatronics, 2003. AIM 2003. Proceedings. 2003 IEEE/ASME International Conference on*, volume 2, pages 1304 – 1308 vol.2, july 2003.

[66] C. W. Ha, B. W. Min, and Y. J. Jang. The resonance frequency automatic adjustment drive IC for piezo ultrasonic motor. In *ACTUATOR 2006*, 2006.

[67] G. H. Haertling. Ferroelectric ceramics: History and technology. *Journal of the American Ceramic Society*, 82(4):797–818, 1999.

[68] M. T. Hagan and M. B. Menhaj. Training feedforward networks with the marquardt algorithm. *IEEE Transactions on Neural Networks*, 5(6):989 – 993, 1994.

[69] P. Hagedorn, T. Sattel, D. Speziari, J. Schmidt, and G. Diana. The importance of rotor flexibility in ultrasonic traveling wave motors. *Smart Materials and Structures*, 7(3):352–68, June 1998.

[70] I. Hagood, N.W. and A. McFarland. Modeling of a piezoelectric rotary ultrasonic motor. *Ultrasonics, Ferroelectrics and Frequency Control, IEEE Transactions on*, 42(2):210–224, 1995.

[71] W. G. Hankel. Ueber die actino- und piëzoelectrischen Eigenschaften des Bergkrystalles und ihre Beziehung zu den thermoelectrischen. *Wiedemann'sche Annalen*, 17:163–175, 1882.

[72] Y. Hara. Driving device, position controller provided with driving device, and camera provided with position controller, 2004. US Patent 20040013420.

[73] S. He, W. Chen, X. Tao, and Z. Chen. Standing wave bi-directional linearly moving ultrasonic motor. *Ultrasonics, Ferroelectrics and Frequency Control, IEEE Transactions on*, 45(5):1133–1139, 1998.

[74] A. Heinzmann, E. Hennig, D. Kopsch, P. Pertsch, S. Richter, and E. Wehrsdorfer. Method for the production of monolithic multilayer actuator monolithic multilayer actuator made of a piezoceramic or electrostrictive material and external electrical contact for a monolithic multilayer actuator, 2006. US Patent 2006055288.

[75] T. Hemsel and S. Priya. Model based analysis of piezoelectric transformers. *Ultrasonics*, 44(Supplement 1):e741 – e745, 2006. Proceedings of Ultrasonics International (UI'05) and World Congress on Ultrasonics (WCU).

[76] D. Henderson. Simple ceramic motor. . . inspiring smaller products. In *Actuator 2006*, 2006.

[77] M. Hermann. *Entwicklung und Untersuchung piezoelektrisch erregter Wanderwellenmotoren für lineare Bewegungen*. PhD thesis, Universität Stuttgart, 1998. IKFF Institutsbericht Nr. 14, Dissertation 1998.

[78] C. Hills and G. Payne. System and method for tracking drive frequency of piezoelectric motor, 2009. US 7545076.

[79] Y. Hiruma, T. Watanabe, H. Nagata, and T. Takenaka. Piezoelectric properties of $(Bi_{1/2}Na_{1/2})TiO_3$-based solid solution for lead-free high-power applications. *Japanese Journal of Applied Physics*, 47(9):7659–7663, 2008.

[80] E. Hollenstein, M. Davis, D. Damjanovic, and N. Setter. Piezoelectric properties of li- and ta-modified $(K_{0.5}Na_{0.5})NbO_3$ ceramics. *Applied Physics Letters*, 87(18):182905, 2005.

[81] E. Horsley, M. Foster, and D. Stone. State-of-the-art piezoelectric transformer technology. In *Power Electronics and Applications, 2007 European Conference on*, pages 1–10, Sept. 2007.

[82] T. Iijima, M. Wada, Y. Nakagawa, and H. Itoh. Ultrasonic motor using flexural standing wave. *Japanese Journal of Applied Physics*, 26S1(Supplement 26-1):191–193, 1987.

[83] A. Iino, K. Suzuki, M. Kasuga, M. Suzuki, and T. Yamanaka. Development of a self-oscillating ultrasonic micro-motor and its application to a watch. *Ultrasonics*, 38(1-8):54–59, Mar. 2000.

[84] T. Ikeda. *Fundamentals of piezoelectricity*. Oxford science publications, 1996.

[85] R. Inaba, A. Tokushima, O. Kawasaki, Y. Ise, and H. Yoneno. Piezoelectric ultrasonic motor. In *IEEE 1987 Ultrasonics Symposium*, pages 747 – 756, 1987.

[86] R. Isermann. On the design and control of mechatronic systems-a survey. *Industrial Electronics, IEEE Transactions on*, 43(1):4 –15, feb 1996.

[87] H. Ishihara, F. Arai, and T. Fukuda. Micro mechatronics and micro actuators. *Mechatronics, IEEE/ASME Transactions on*, 1(1):68 –79, march 1996.

[88] S. Iwamatsu, S. Ueha, M. Kuribayashi, and E. Mori. Rotary ultrasonic motor using extensional vibration of a ring. *Japanese Journal of Applied Physics*, 25S1(Supplement 25-1):174–176, 1986.

[89] Y. Izuno, T. Izumi, H. Yasutsune, E. Hiraki, and M. Nakaoka. Speed tracking servo control system incorporating traveling-wave-type ultrasonic motor and feasible evaluations. *Industry Applications, IEEE Transactions on*, 34(1):126–132, 1998.

[90] B. Jaffe, R. S. Roth, and S. Marzullo. Piezoelectric properties of lead zirconate-lead titanate solid-solution ceramics. *Journal of Applied Physics*, 25(6):809–810, 1954.

[91] M. Jufer. *Electromécanique*, volume IX of *Traité d'Electricité*. Presses Polytechniques et Universitaires Romandes, 3rd edition, 1995.

[92] M. Jufer and F. Coulon. *Introduction à l'électrotechnique*, volume I of *Traité d'Electricité*. Presses Polytechniques et Universitaires Romandes, 7th, 1995.

[93] G. Kandare and J. Wallaschek. Derivation and validation of a mathematical model for traveling wave ultrasonic motors. *Smart Materials and Structures*, 11(4):565–74, Aug. 2002.

[94] I. Kartashev and T. Vontz. Regimes of piezoelectric transformer operation II. *Measurement Science and Technology*, 20(5):055108 (14pp), 2009.

[95] K. Kataoka. Control apparatus for vibration driven motor, 1991. US Patent 5004964.

[96] S. Katzir. Measuring constants of nature: confirmation and determination in piezoelectricity. *Studies In History and Philosophy of Science Part B: Studies In History and Philosophy of Modern Physics*, 34(4):579 – 606, 2003.

[97] C. Kauczor. *Entwurf schwach gedämpfter piezoelektrischer Ultraschallsysteme*. PhD thesis, Universität Paderborn, 2009.

[98] C. Kauczor and N. Fröhleke. Inverter topologies for ultrasonic piezoelectric transducers with high mechanical q-factor. In *Power Electronics Specialists Conference (PESC), Aachen, 2004*, Piscateway, 2004. ISBN 07803-8400-8.

[99] C. Kauczor, T. Schulte, and N. Fröhleke. Resonant power converter for ultrasonic piezoelectric converter. In *Proceedings of the ACTUATOR 2002, 8th International Conference on New Actuators, Bremen 2002*, pages 485–488, Bremen, 2002. Messe Bremen GmbH.

[100] C. Kauczor, T. Schulte, and H. Grotstollen. Piezoelektrische Transformatoren - Schaltungen und Anwendungen. In *47. Internationales Wissenschaftliches Kolloquium TU Illmenau*, 2002.

[101] S. Kawada, H. Ogawa, M. Kimura, K. Shiratsuyu, and H. Niimi. High-power piezoelectric vibration characteristics of textured $SrBi_2Nb_2O_9$ ceramics. *Japanese Journal of Applied Physics*, 45(9B):7455–7459, 2006.

[102] S. Kawashima, O. Ohnishi, H. Hakamata, S. Tagami, A. Fukuoka, T. Inoue, and S. Hirose. Third order longitudinal mode piezoelectric ceramic transformer and its application to high-voltage power inverter. In *Ultrasonics Symposium, 1994. Proceedings., 1994 IEEE*, volume 1, pages 525–530 vol.1, Nov 1994.

[103] K. Kühnen and H. Janocha. Integrated measurement and power electronics for piezoelectrical self-sensing actuators. In *Mechatronik 2005 VDI-Berichte 1892.2*, pages 1137 – 1156, Wiesloch, June 2005.

[104] H. W. Kim, S. Dong, P. Laoratanakul, K. Uchino, and T. G. Park. Novel method for driving the ultrasonic motor. *Ultrasonics, Ferroelectrics and Frequency Control, IEEE Transactions on*, 49(10):1356–1362, 2002.

[105] B. Koc, P. Bouchilloux, and K. Uchino. Piezoelectric micromotor using a metal-ceramic composite structure. *Ultrasonics, Ferroelectrics and Frequency Control, IEEE Transactions on*, 47(4):836–843, 2000.

[106] A. Kumada. A piezoelectric ultrasonic motor. *Japanese Journal of Applied Physics*, 24S2(Supplement 24-2):739–739, 1985.

[107] M. Kurosawa, M. Takahashi, and T. Higuchi. Ultrasonic linear motor using surface acoustic waves. *Ultrasonics, Ferroelectrics and Frequency Control, IEEE Transactions on*, 43(5):901–906, 1996.

[108] S. Lang. *Algebra*. Springer, January 2002.

[109] K. K. Leang and S. Devasia. Design of hysteresis-compensating iterative learning control for piezo-positioners: Application to atomic force microscopes. *Mechatronics*, 16(3-4):141 – 158, 2006.

[110] R. Lerch. Simulation of piezoelectric devices by two- and three-dimensional finite elements. *Ultrasonics, Ferroelectrics and Frequency Control, IEEE Transactions on*, 37(3):233–247, 1990.

[111] H. Leuthold. *Modélisation et intégration de la commande de moteurs à courant-continu sans collecteurs*. PhD thesis, Ecole Polytechnique Fédérale de Lausanne (EPFL), Lausanne, 1991.

[112] E. Li, H. Kakemoto, T. Hoshina, and T. Tsurumi. A shear-mode ultrasonic motor using potassium sodium niobate-based ceramics with high mechanical quality factor. *Japanese Journal of Applied Physics*, 47(9):7702–7706, 2008.

[113] E. Li, R. Sasaki, T. Hoshina, H. Takeda, and T. Tsurumi. Miniature ultrasonic motor using shear mode of potassium sodium niobate-based lead-free piezoelectric ceramics. *Japanese Journal of Applied Physics*, 48(9):09KD11, 2009.

[114] R. Li, N. Frohleke, and J. Bocker. Llcc-pwm inverter for driving high-power piezoelectric actuators. In *Power Electronics and Motion Control Conference, 2008. EPE-PEMC 2008. 13th*, pages 159–164, Sept. 2008.

[115] R. Li, N. Froleke, and J. Bocker. Analysis and design of a novel three-level llcc inverter supplying an airborne piezoelectric brake actuator. In *Power Electronics Specialists Conference, 2007. PESC 2007. IEEE*, pages 2155–2161, June 2007.

[116] R. Li, M. Loenneker, N. Froehleke, and J. Boecker. Design of power supply for driving high power piezoelectric actuators. In *Industry Applications Society Annual Meeting, 2008. IAS '08. IEEE*, pages 1–6, Oct. 2008.

[117] C. Lin and F. Lee. Design of a piezoelectric transformer converter and its matching networks. In *Power Electronics Specialists Conference, PESC '94 Record., 25th Annual IEEE*, pages 607–612 vol.1, Jun 1994.

[118] C.-H. Lin, Y. Lu, H.-J. Chiu, and C.-L. Ou. Eliminating the temperature effect of piezoelectric transformer in backlight electronic ballast by

applying the digital phase-locked-loop technique. *Industrial Electronics, IEEE Transactions on*, 54(2):1024–1031, April 2007.

[119] C.-H. Lin, Y. Lu, K.-J. Pai, and Y.-Q. Chen. Achieving maximum-efficiency tracking control for backlight electronic ballast with phase-locked loop techniques. In *Control Applications, 2004. Proceedings of the 2004 IEEE International Conference on*, volume 2, pages 1651–1656 Vol.2, Sept. 2004.

[120] C. W. Lin. *The waveform detection of permanent magnet step motors and its application to closed-loop control*. PhD thesis, Illinois University, Urbana-Champaign, 1979.

[121] D. Lin, M. S. Guo, K. H. Lam, K. W. Kwok, and H. L. W. Chan. Lead-free piezoelectric ceramic $(K_{0.5}Na_{0.5})NbO_3$ with MnO_2 and $K_{5.4}Cu_{1.3}Ta_{10}O_{29}$ doping for piezoelectric transformer application. *Smart Materials and Structures*, 17(3):035002 (6pp), 2008.

[122] F.-J. Lin, R.-Y. Duan, and H.-H. Lin. An ultrasonic motor drive using llcc resonant technique. In *Power Electronics Specialists Conference, 1999. PESC 99. 30th Annual IEEE*, volume 2, pages 947–952 vol.2, 1999.

[123] F.-J. Lin, R.-Y. Duan, and J.-C. Yu. An ultrasonic motor drive using a current-source parallel-resonant inverter with energy feedback. *Power Electronics, IEEE Transactions on*, 14(1):31–42, Jan 1999.

[124] G. Lippmann. Extension du principe de carnot à la théorie des phénomènes électriques. Equations différentielles générales de l'équilibre et du mouvement d'un système électrique réversible quelconque. *Comptes rendus hebdomadaires des séances de l'Académie des sciences*, T82:1425–1428, 1876.

[125] G. Lippmann. Sur le principe de la conservation de l'électricité, ou second principe de la théorie des phénomènes. *Comptes rendus hebdomadaires des séances de l'Académie des sciences*, T92:1049–1051 and 1149–1152, 1881.

[126] R. Longchamp. *Commande numérique de systèmes dynamiques*. Presses Polytechniques et Universitaires Romandes, 1995.

[127] J. Maas and T. Schulte. High performance speed control for ultrasonic motors. In *Advanced Intelligent Mechatronics, 1999. Proceedings. 1999 IEEE/ASME International Conference on*, pages 91–96, 1999.

[128] J. Maas, T. Schulte, and N. Froehleke. Model-based control for ultrasonic motors. *Mechatronics, IEEE/ASME Transactions on*, 5(2):165–180, 2000.

[129] T. Maeno. Recent progress of ultrasonic motors in Japan. In *The First International Workshop on Ultrasonic Motors and Actuators*, Yokohama, Japan, November 2005.

[130] T. Maeno, T. Tsukimoto, and A. Miyake. Finite-element analysis of the rotor/stator contact in a ring-type ultrasonic motor. *Ultrasonics, Ferroelectrics and Frequency Control, IEEE Transactions on*, 39(6):668–674, 1992.

[131] K. Makihara, J. Onoda, and K. Minesugi. Novel approach to self-sensing actuation for semi-active vibration suppression. *AIAA Journal*, 44(7):1445–1453, 2006. cited By (since 1996) 5.

[132] S. Manuspiya, P. Laoratanakul, and K. Uchino. Integration of a piezoelectric transformer and an ultrasonic motor. *Ultrasonics*, 41(2):83–87, Mar. 2003.

[133] R. M. Martin. Piezoelectricity. *Phys. Rev. B*, 5(4):1607–1613, Feb 1972.

[134] W. G. May. Piezoelectric electomechanical translation apparatus, 1975. US Patent 3902084.

[135] R. Moroney, R. White, and R. Howe. Ultrasonic micromotors. In *Ultrasonics Symposium, 1989. Proceedings., IEEE 1989*, pages 745 –748 vol.2, oct 1989.

[136] J. M. Murphy. *Analytical design and optimization of ultrasonic vibrational transducers for spinal surgery*. PhD thesis, Ecole Polytechnique Fédérale de Lausanne, Lausanne, 2007.

[137] Y. Nakagawa, Y. Nakagawa, A. Saito, and T. Maeno. Nonlinear dynamic analysis of traveling wave-type ultrasonic motors. *Ultrasonics, Ferroelectrics and Frequency Control, IEEE Transactions on*, 55(3):717–725, 2008.

[138] K. Nakamura, J. Margairaz, T. Ishii, and S. Ueha. Ultrasonic stepping motor using spatially shifted standing vibrations. *Ultrasonics, Ferroelectrics and Frequency Control, IEEE Transactions on*, 44(4):823–828, 1997.

[139] T. T. Nguyen. Self-oscillating switching amplifier, 2006.

[140] D. W. Noren. high temperature, high vacuum, diffusion bonded piezoelectric motor sandwich, utilizing intermediate wafflelike layers, 1969. US Patent 3573511.

[141] K. Ohnishi. A novel ultrasonic linear actuator. In *Applications of Ferroelectrics, 1990., IEEE 7th International Symposium on*, pages 206 –212, jun 1990.

[142] O. Ohnishi, O. Myohga, T. Uchikawa, M. Tamegai, T. Inoue, and S. Takahashi. Piezoelectric ultrasonic motor using longitudinal-torsional composite vibration of a cylindrical resonator. In *Ultrasonics Symposium, 1989. Proceedings., IEEE 1989*, pages 739 –743 vol.2, oct 1989.

[143] S. Omatu, M. Khalid, and R. R. Yusof. *Neuro-control and its applications*. Advances in industrial control. Springer, 1996.

[144] S. Opricovic and G.-H. Tzeng. Compromise solution by MCDM methods: A comparative analysis of vikor and topsis. *European Journal of Operational Research*, 156(2):445 – 455, 2004.

[145] G. Pahl, W. Beitz, J. Feldhusen, and K.-H. Grote. *Engineering Design: A Systematic Approach*. Springer, 3rd edition, 2007.

[146] S. K. Parashar, U. von Wagner, and P. Hagedorn. Nonlinear shear-induced flexural vibrations of piezoceramic actuators: experiments and modeling. *Journal of Sound and Vibration*, 285(4-5):989 – 1014, 2005.

[147] C. Péclat. *Conception et réalisation d'un micromoteur piézoélectrique*. PhD thesis, Département d'électricité, Ecole Polytechnique Fédérale de Lausanne, Lausanne, Switzerland, 1995.

[148] C. Péclat and K. Trümpy. Piezoelectric motor having an anrrangement which provides information relative to the rotor position and/or the rotor's number of revolutions, 1998. United States Patent 5,719,461.

[149] F. Pellicano, M. Amabili, and M. P. Païdoussis. Effect of the geometry on the non-linear vibration of circular cylindrical shells. *International Journal of Non-Linear Mechanics*, 37(7):1181 – 1198, 2002.

[150] Y.-F. Peng, R.-J. Wai, and C.-M. Lin. Implementation of llcc-resonant driving circuit and adaptive cmac neural network control for linear piezoelectric ceramic motor. *Industrial Electronics, IEEE Transactions on*, 51(1):35–48, Feb. 2004.

[151] R. Perez Suarez. *Analysis of monolithic piezoceramic structures for micro and nano-positioning*. PhD thesis, Ecole Polytechnique Fédérale de Lausanne, 2002.

[152] Y. Perriard. *Méthodologie de conception d'activateurs pour ventricule d'assistance cardiaque implantable*. PhD thesis, Ecole Polytechnique Fédérale de Lausanne (EPFL), Lausanne, 1992.

[153] J. Persson. *Innovative Standstill Position Detection Combined With Sensorless Control of Synchronous Motors*. PhD thesis, Ecole Polytechnique Fédérale de Lausanne, 2005.

[154] J. Persson and Y. Perriard. An optimized extended Kalman filter algorithm for hybrid stepper motors. In *Industrial Electronics Society, 2003. IECON '03. The 29th Annual Conference of the IEEE*, volume 1, pages 297–300 vol.1, 2003.

[155] P. D. Pfister. *Very high-speed slotless permanent-magnet motors : theory, design and validation.* PhD thesis, Ecole Polytechnique Fédérale de Lausanne (EPFL), 2009.

[156] S. Pirrotta, R. Sinatra, and A. Meschini. A novel simulation model for ring type ultrasonic motor. *Meccanica*, 42(2):127–139, 2007.

[157] J. Pons, H. Rodriguez, R. Ceres, and L. Calderon. Novel modeling technique for the stator of traveling wave ultrasonic motors. *Ultrasonics, Ferroelectrics and Frequency Control, IEEE Transactions on*, 50(11):1429 – 1435, nov 2003.

[158] J. L. Pons, H. Rodríguez, J. F. Fernández, M. Villegas, and F. Seco. Parametrical optimisation of ultrasonic motors. *Sensors and Actuators A: Physical*, 107(2):169 – 182, 2003.

[159] J. L. Pons, H. Rodriguez, F. Seco, R. Ceres, and L. Calderon. Modelling of piezoelectric transducers applied to piezoelectric motors: a comparative study and new perspective. *Sensors and Actuators A: Physical*, 110(1-3):336 – 343, 2004. Selected Papers from Eurosensors XVI Prague, Czech Republic.

[160] S. Priya. High power universal piezoelectric transformer. *Ultrasonics, Ferroelectrics and Frequency Control, IEEE Transactions on*, 53(1):23–29, Jan. 2006.

[161] A. Qamar, C. During, and J. Wikander. Designing mechatronic systems, a model-based perspective, an attempt to achieve sysml-matlab/simulink model integration. In *Proceedings of the IEEE/ASME International Conference on Advanced Intelligent Mechatronics 2009. AIM 2009.*, pages 1306 –1311, july 2009.

[162] G.-A. Racine, C. Beuret, R. Luthier, and N. de Rooij. Speed control of elastic force motors by means of integrated piezoelectric sensors. In *Micro Electro Mechanical Systems, 1994, MEMS '94, Proceedings, IEEE Workshop on*, pages 124–129, 1994.

[163] G.-A. Racine, R. Luthier, and N. de Rooij. Hybrid ultrasonic micromachined motors. In *Micro Electro Mechanical Systems, 1993, MEMS '93, Proceedings An Investigation of Micro Structures, Sensors, Actuators, Machines and Systems. IEEE.*, pages 128–132, Feb 1993.

[164] G.-A. Racine, R. Luthier, and N. de Rooij. Piezoelectric position sensor for ultrasonic efm motors. *Sensors and Actuators A: Physical*, 42(1-3):661 – 665, 1994. Proceedings of Eurosensors VIII.

[165] G.-A. Racine, P. Muralt, and M.-A. Dubois. Flexural-standing-wave elastic force motor using zno and pzt thin film on micromachined silicon membranes for wristwatch applications. *Smart Materials and Structures*, 7(3):404–416, 1998.

[166] P. Ragot. *Modélisation analytique multiphysique pour la conception optimale de moteurs synchrones à aimants permanents*. PhD thesis, Ecole Polytechnique Fédérale de Lausanne (EPFL), Lausanne, 2008.

[167] K. M. Ragulskis, R. Bansevicius, R. A. Barauskas, and G. Kulvietis. *Vibromotors for Precision Microrobots*. Hemisphere Publishing Co., 1988.

[168] L. R. Ray, A. Ramasubramanian, and J. Townsend. Adaptive friction compensation using extended kalman-bucy filter friction estimation. *Control Engineering Practice*, 9(2):169 – 179, 2001.

[169] J. Rödel, W. Jo, K. T. P. Seifert, E.-M. Anton, T. Granzow, and D. Damjanovic. Perspective on the development of lead-free piezoceramics. *Journal of the American Ceramic Society*, 92(6):1153–1177, 2009.

[170] J.-S. Rho, K.-I. Oh, H.-S. Kim, and H.-K. Jung. Characteristic analysis and design of a b14 rotary ultrasonic motor for a robot arm taking the contact mechanism into consideration. *Ultrasonics, Ferroelectrics and Frequency Control, IEEE Transactions on*, 54(4):715–728, April 2007.

[171] F. Roos, H. Johansson, and J. Wikander. Optimal selection of motor and gearhead in mechatronic applications. *Mechatronics*, 16(1):63 – 72, 2006.

[172] C. A. Rosen. *Ceramic transformers and filters*. PhD thesis, Syracuse University, 1956.

[173] M. Rossi. *Audio*. Presses Polytechniques et Universitaires Romandes, 2007.

[174] E. Rothenhöfer. *Entwicklungsgrundlagen für piezoelektrische Ultraschallmotoren am Beispiel eines linearen Antriebs mit gekoppelten Moden*. PhD thesis, Universität Stuttgart, 2010.

[175] K. Ruschmeyer. *Piezokeramik : Grundlagen, Werkstoffe, Applikationen*, volume 460 of *Kontakt & Studium. Werkstoffe*. Expert, Renningen-Malmsheim, 1995.

[176] Y. Saito, H. Takao, T. Tani, T. Nonoyama, K. Takatori, T. Homma, T. Nagaya, and M. Nakamura. Lead-free piezoceramics. *Nature*, 432(7013):84–87, Nov. 2004.

[177] T. Sashida. Trial construction and operation of an ultrasonic vibration drive motor: Theoretical and experimental inverstigation of its performances. *Oyo Butsuri*, 51:713–720, 1982.

[178] T. Sashida. Motor device utilizing ultrasonic oscillation, 1985. US Patent 4562374.

[179] T. Sashida. *An introduction to ultrasonic motors*. Number 28 in Monographs in Electrical and Electronic Engineering. Clarendon Press, 1993.

[180] T. Sattel, P. Hagedorn, and J. Schmidt. The contact problem in ultrasonic traveling-wave motors. *Journal of Applied Mechanics*, 77(3):031014, 2010.

[181] G. Schweitzer. Mechatronics-a concept with examples in active magnetic bearings. *Mechatronics*, 2(1):65 – 74, 1992.

[182] Seiko. *Technical Guide Caliber 8F32A*.

[183] T. Senjyu, T. Kashiwagi, and K. Uezato. Position control of ultrasonic motors using mrac with dead-zone compensation. *Industrial Electronics, IEEE Transactions on*, 48(6):1278–1285, 2001.

[184] T. Senjyu, H. Miyazato, S. Yokoda, and K. Uezato. Speed control of ultrasonic motors using neural network. *Power Electronics, IEEE Transactions on*, 13(3):381–387, 1998.

[185] T. Senjyu, M. Nakamura, N. Urasaki, H. Sekine, and T. Funabashi. Mathematical model of ultrasonic motors for speed control. page 6 pp., march 2006.

[186] T. Senjyu, Y. Ochi, Y. Kikunaga, M. Tokudome, A. Yona, E. B. Muhando, N. Urasaki, and T. Funabashi. Sensor-less maximum power point tracking control for wind generation system with squirrel cage induction generator. *Renewable Energy*, 34(4):994–999, Apr. 2009.

[187] T. Senjyu, T. Senjyu, K. Uezato, and H. Miyazato. Adjustable speed control of ultrasonic motors by adaptive control. *Power Electronics, IEEE Transactions on*, 10(5):532–538, 1995.

[188] T. Senjyu, S. Yokoda, and K. Uezato. A study on high-efficiency drive of ultrasonic motors. *Electric Power Components and Systems*, 29(3):179–189, 2001.

[189] T. Senjyu, T. Yoshida, M. Nakamura, N. Urasaki, T. Funabashi, and H. Sekine. Position sensorless control for ultrasonic motors based on input voltage information. *Electrical Engineering in Japan*, 163(1):57–64, 2008.

[190] T. Senjyu, T. Yoshida, K. Uezato, N. Urasaki, and S. Panda. Speed sensorless control of ultrasonic motors using neural network. In *Industrial Electronics Society, 2003. IECON '03. The 29th Annual Conference of the IEEE*, volume 1, pages 335–340 vol.1, 2003.

[191] E. Silva and N. Kikuchi. Design of piezoelectric transducers using topology optimization. *Smart Materials and Structures*, 8(3):350–364, 1999.

[192] J. Simmers, Garnett E., J. R. Hodgkins, D. D. Mascarenas, G. Park, and H. Sohn. Improved piezoelectric self-sensing actuation. *Journal of Intelligent Material Systems and Structures*, 15(12):941–953, 2004.

[193] K. Spanner. Survey of the various operating principles of ultrasonic piezomotors. In *ACTUATOR 2006, 10th International Conference on New Actuators*, 2006.

[194] R. Steigerwald. A comparison of half-bridge resonant converter topologies. *Power Electronics, IEEE Transactions on*, 3(2):174 –182, apr 1988.

[195] M. Takahashi, M. Kurosawa, and T. Higuchi. Direct frictional driven surface acoustic wave motor. In *Solid-State Sensors and Actuators, 1995 and Eurosensors IX.. Transducers '95. The 8th International Conference on*, volume 1, pages 401 –404, jun 1995.

[196] T. Takano, H. Hirata, and Y. Tomikawa. Analysis of nonaxisymmetric vibration mode piezoelectric annular plate and its application to an ultrasonic motor. *Ultrasonics, Ferroelectrics and Frequency Control, IEEE Transactions on*, 37(6):558 –565, nov 1990.

[197] T. Takano, Y. Tomikawa, and C. Kusakabe. Same phase drive-type ultrasonic motors using two degenerate bending vibration modes of a disk. *Ultrasonics, Ferroelectrics and Frequency Control, IEEE Transactions on*, 39(2):180–186, 1992.

[198] K. Takemura, Y. Ohno, and T. Maeno. Design of a plate type multi-dof ultrasonic motor and its self-oscillation driving circuit. *Mechatronics, IEEE/ASME Transactions on*, 9(3):474 –480, sept. 2004.

[199] T. Takenaka, H. Nagata, and Y. Hiruma. Current developments and prospective of lead-free piezoelectric ceramics. *Japanese Journal of Applied Physics*, 47(5):3787–3801, 2008.

[200] H. Tamura, M. Iwase, S. Hirose, M. Aoyagi, T. Takano, and Y. Tomikawa. Measurement of $LiNbO_3$ rectangular plate under large vibration velocity of the first longitudinal and second flexural modes. *Japanese Journal of Applied Physics*, 47(5):4034–4040, 2008.

[201] H. Tamura, K. Kawai, T. Takano, Y. Tomikawa, S. Hirose, and M. Aoyagi. Diagonally symmetric form ultrasonic motor using $linbo_3$ plate. *Japanese Journal of Applied Physics*, 46(7B):4698–4703, 2007.

[202] H. Tamura, K. Shibata, M. Aoyagi, T. Takano, Y. Tomikawa, and S. Hirose. Single phase drive ultrasonic motor using $LiNbO_3$ rectangular vibrator. *Japanese Journal of Applied Physics*, 47(5):4015–4020, 2008.

[203] K. Tani, M. Suzuki, K. Furuta, T. Sakuhara, and T. Ataka. Development of a new type piezoelectric micromotor. In *Proceedings of the Eleventh Annual International Workshop on Micro Electro Mechanical Systems, 1998. MEMS 98.*, pages 396–401, Jan 1998.

[204] G. C. Tibbetts. Transducer leads, 1959. US Patent 2877363.

[205] J. Tichy and G. H. Gautschi. *Piezoelektrische Messtechnik*. Springer, 1980.

[206] H. Tiersten. Hamilton's principle for linear piezoelectric media. *Proceedings of the IEEE*, 55(8):1523 – 1524, aug. 1967.

[207] F. Torfi, R. Z. Farahani, and S. Rezapour. Fuzzy ahp to determine the relative weights of evaluation criteria and fuzzy topsis to rank the alternatives. *Applied Soft Computing*, 10(2):520 – 528, 2010.

[208] C. Touzé, O. Thomas, and A. Chaigne. Hardening/softening behaviour in non-linear oscillations of structural systems using non-linear normal modes. *Journal of Sound and Vibration*, 273(1-2):77 – 101, 2004.

[209] M.-S. Tsai, C.-H. Lee, and S.-H. Hwang. Dynamic modeling and analysis of a bimodal ultrasonic motor. *Ultrasonics, Ferroelectrics and Frequency Control, IEEE Transactions on*, 50(3):245–256, 2003.

[210] T. Tsuchiya, Y. Kagawa, N. Wakatsuki, and H. Okamura. Finite element simulation of piezoelectric transformers. *Ultrasonics, Ferroelectrics and Frequency Control, IEEE Transactions on*, 48(4):872–878, Jul 2001.

[211] K. Uchino. Piezoelectric ultrasonic motors: overview. *Smart Materials and Structures*, 7(3):273, 1998.

[212] K. Uchino, S. Cagatay, B. Koc, S. Dong, P. Bouchilloux, and M. Strauss. Micro piezoelectric ultrasonic motors. *Journal of Electroceramics*, 13(1):393–401, July 2004.

[213] T. Ueda, O. Miyahara, J. Kitahara, and T. Furukawa. Ultrasonic motor, 1991. EP0447172.

[214] S. Ueha and Y. Tomikawa. *Ultrasonic Motors Theory and Applications*. Monographs in Electrical and Electrnoic Engineering. Clarendon Press, 1993.

[215] P. E. Vasiliev. Vibration motor control, 1979. UK Patent 2020857.

[216] V. S. Vishnevskij, L. G. gultyaeva, I. A. Kartashev, and V. V. Lavrinenko. Piezoelectric motor, 1976. SU851560.

[217] V. S. Vishnevsky. Piezoelectric motor structures, 1977. US Patent 4019073.

[218] V. S. Vishnevsky, I. A. Kartashev, V. V. Lavrinenko, O. L. Boichenko, V. S. Koval, J. V. Golovyashin, N. F. Serov, L. I. Shinkarenko, and O. G. Jurash. Piezoelectric motor, 1984. US Patent 4453103.

[219] W. Voigt. *Lehrbuch der Kristallphysik (mit Ausschluss der Kristalloptik)*, volume 34 of *B. G. Teubners Sammlung von Lehrbüchern auf dem Gebiete der mathematischen Wissenschaften mit Einschluss ihrer Anwendungen*. Teubner, Leipzig, 1910.

[220] A. von Hippel, R. G. Breckenridge, F. G. Chesley, and L. Tisza. High dielectric constant ceramics. *Industrial & Engineering Chemistry*, 38(11):1097–1109, Nov. 1946.

[221] O. Vyshnevskyy, S. Kovalev, and W. Wischnewskiy. New type of piezoelectric standing wave ultrasonic motors with cylindrical actuators. In *ACTUATOR 2004, 9th International Conference on New Actuators*, June 2004.

[222] O. Vyshnevskyy, S. Kovalev, and W. Wischnewskiy. A novel, single-mode piezoceramic plate actuator for ultrasonic linear motors. *Ultrasonics, Ferroelectrics and Frequency Control, IEEE Transactions on*, 52(11):2047–2053, 2005.

[223] R.-J. Wai and J.-D. Lee. Comparison of voltage-source resonant driving schemes for a linear piezoelectric ceramic motor. *Industrial Electronics, IEEE Transactions on*, 55(2):871–879, Feb. 2008.

[224] R.-J. Wai and K.-H. Su. Supervisory control for linear piezoelectric ceramic motor drive using genetic algorithm. *Industrial Electronics, IEEE Transactions on*, 53(2):657–673, April 2006.

[225] R.-J. Wai and C.-H. Tu. Design of total sliding-mode-based genetic algorithm control for hybrid resonant-driven linear piezoelectric ceramic motor. *Power Electronics, IEEE Transactions on*, 22(2):563–575, March 2007.

[226] S. H. Walker, M. G. Lagally, and R. D. Lorenz. Method and apparatus for improved control of piezoelectric positioners, 1998. US 5714831.

[227] J. Wallaschek. Piezoelectric ultrasonic motors. *Journal of Intelligent Material Systems and Structures*, 6(1):71–83, 1995.

[228] J. Wallaschek. Contact mechanics of piezoelectric ultrasonic motors. *Smart Materials and Structures*, 7(3):369–381, 1998.

[229] Wikipedia. Pin tumbler lock. In Wikipedia: The Free Encyclopedia. Internet., September 8 2009.

[230] A. L. W. Williams and W. J. Brown. Piezoelectric motor, 1948. United States Patent US 2439499.

[231] W. Wischnewskiy. Piezoelectric miniature motor e.g. for photographic and cinematographic equipment drives, printers, tape-recorders and CD devices, 1996. German Patent 4438876.

[232] R.-J. Xie and Y. Akimune. Lead-free piezoelectric ceramics in the (1 -x)sr2nanb5o15-xca2nanb5o15(0.05 [less-than-or-equal]x[less-than-or-equal] 0.35) system. *Journal of Materials Chemistry*, 12(10):3156–3161, 2002.

[233] X. Xu, Y. C. Liang, H. P. Lee, W. Z. Lin, S. P. Lim, K. H. Lee, and X. H. Shi. Identification and speed control of ultrasonic motors based on neural networks. *Journal of Micromechanics and Microengineering*, 13(1):104–114, 2003.

[234] A. Yabuki, M. Aoyagi, Y. Tomikawa, and T. Takano. Piezoelectric linear motors for driving head element of cd-rom. *Japanese Journal of Applied Physics*, 33(Part 1, No. 9B):5365–5369, 1994.

[235] T. Yamaguchi, K. Adachi, Y. Ishimine, and K. Kato. Wear mode control of drive tip of ultrasonic motor for precision positioning. *Wear*, 256(1-2):145 – 152, 2004.

[236] Y. Yang, F. Bisogno, A. Schittler, S. Nittayarumphong, M. Radecker, W.-J. Fischer, and M. Fahlenkamp. Comparison of inductor-half-bridge and class-e resonant topologies for piezoelectric transformer applications. In *Energy Conversion Congress and Exposition, 2009. ECCE 2009. IEEE*, pages 776–782, Sept. 2009.

[237] T.-H. Yu and C.-C. Yin. A self-sensing wedge-wave ultrasonic motor using modal sensors. In *Proceedings of the 3rd International Conference on Smart Materials, Structures and Systems - CIMTEC 2008*, 2008.

[238] Z. Yu, K. C. Chan, J. Guo, J. Y. Dai, B. Wang, X. P. Jiang, and K. W. Kwok. Lead free bnt ceramics as driving element in traveling wave type ultrasonic motor. In S. Du, J. Leng, and A. K. Asundi, editors, *Proc. SPIE, Vol. 6423, 642325 (2007)*, volume 6423, page 642325. SPIE, 2007.

[239] O. Zharii. An exact mathematical model of a travelling wave ultrasonic motor. volume 1, pages 545 –548 vol.1, nov 1994.

[240] M. Zhu. Contact analysis and mathematical modeling of traveling wave ultrasonic motors. *Ultrasonics, Ferroelectrics and Frequency Control, IEEE Transactions on*, 51(6):668 – 679, june 2004.

[241] W. Zogg and T. Burger. Locking device, 2008. International Patent 2008058415.

[242] J. Zumeris. Ceramic motor, 1993. US Patent 5453653.

List of Symbols

Symbol	Description	Units
Latin letters		
a	Width	$[m]$
A	Surface	$[m^2]$
$\boldsymbol{A}$	Vector of coefficients	[–]
A_C	Surface where charges are applied	$[m^2]$
A_F	Surface where forces are applied	$[m^2]$
b	Height	$[m]$
$\boldsymbol{b}$	Bias vector	[–]
C	Elastic compliance	$[m^2/N]$
$\boldsymbol{C}$	Rayleigh damping matrix	$[kg/s]$
C_0	Static capacitance	$[F]$
C_m	Motional capacitance	$[F]$
C_p	Parallel stabilising capacitor	$[F]$
C_r	Equivalent capacitor modeling slip	$[F]$
C_s	Serial matching capacitor	$[F]$
d	Piezoelectric constant	$[C/N]$ or $[m/V]$
$\boldsymbol{D}$	Electric displacement	$[As/m^2]$
e	Piezoelectric constant	$[C/m^2]$ or $[N/Vm]$
$\boldsymbol{E}$	Electric field strength	$[V/m]$
$\boldsymbol{E}$	Matrix of simulations	[–]
$\boldsymbol{E}^*$	Matrix of simulations (absolute coord.)	[–]
E_c	Kinetic energy	$[V/m]$
E_d	Dielectric energy	$[V/m]$
E_e	Elastic energy	$[V/m]$
f	Frequency	[Hz]
F	Force (in the mechanical branch)	$[N]$

Symbol	Description	Units
f_0	Initial control frequency	$[Hz]$
f_a	Antiresonance frequency	$[Hz]$
$\boldsymbol{F}_B$	Vector of mechanical body forces	$[N]$
F_c	Traction applied to the piezoceramic	$[N]$
f_p	Parallel resonance frequency	$[Hz]$
$\boldsymbol{F}_P$	Vector of mechanical point forces	$[N]$
f_s	Series resonance frequency	$[Hz]$
$\boldsymbol{F}_S$	Vector of mechanical surface forces	$[N]$
f_r	Resonance frequency	$[Hz]$
g	Piezoelectric constant	$[Vm/N]$ or $[m^2/C]$
G_{LC}	LC resonant converter transfer function	[–]
G_{LLCC}	LLCC resonant converter transfer function	[–]
h	Piezoelectric constant	$[V/m]$ or $[N/C]$
i	Instantaneous current	$[A]$
I	Current	$[A]$
ID	Inner diameter	$[m]$
j	$\sqrt{-1}$	[–]
K_d	Phase detector gain	$[V/rad]$
K_o	VCO gain	$[rad/Vs]$
$\boldsymbol{K}_{\xi\xi}$	Stiffness matrix	$[N/m]$
$\boldsymbol{K}_{\phi\xi}$	Piezoelectric matrix	$[C/m^2]$
$\boldsymbol{K}_{\phi\phi}$	Dielectric matrix	$[F/m]$
L_m	Motional inductance	$[H]$
L_p	Parallel matching inductance	$[H]$
L_s	Serial matching inductance	$[H]$
m	Mass	$[kg]$
$\boldsymbol{M}$	Mass matrix	$[kg]$
m_e	Equivalent mass	$[kg]$
M_p	Figure of merict	[–]
m_r	Displaced mass portion of the rotor	$[kg]$
m_v	Vibrator mass	$[kg]$
OD	Outer diameter	$[m]$
$\boldsymbol{p}$	Neural network input vector	[–]
P_1	Starting point	[–]
P_2	End point	[–]
P_d	Mean power	$[W]$
Q	Electrical charge	$[As]$
Q_m	Quality factor	[–]
Q_P	Electrical point charge	$[As]$

Symbol	Description	Units
Q_S	Electrical surface charge	$[As/m^2]$
R_F	Equivalent slip losses	$[\Omega]$
R_L	Load resistance	$[\Omega]$
R_m	Motional resistance	$[\Omega]$
R_r	Equivalent mechanical losses	$[\Omega]$
s	Elastic compliance	$[m^2/N]$
$\boldsymbol{S}$	Strain tensor	$[m^2/N]$
t	Time	$[s]$
$\boldsymbol{T}$	Stress tensor	$[N/m^2]$
T	Temperature	$[K]$
U_c	Static capacitor voltage drop	$[V]$
U_{dc}	DC voltage	$[V]$
U_d	Mean voltage	$[V]$
v	Speed	$[m/s]$
V	Volume	$[m^3]$
$v_c(t), V_c(s)$	VCO control voltage	$[V]$
V_{cc}	Logic section voltage source	$[V]$
$v_d(t), V_d(s)$	Phase detector output voltage	$[V]$
V_{dd}	DC voltage source	$[V]$
w	Rotor length	$[m]$
W	Overall motor length	$[m]$
$\boldsymbol{W}$	Weight matrix	[–]
x, y, z	Cartesian coordinates	[–]
x', y', z'	Rotated cartesian coordinate system	[–]
X	Reactance	$[\Omega]$
$\boldsymbol{X}$	Model matrix	[–]
y	Response function	[–]
Y	Admittance	$[S]$
$\boldsymbol{Y}$	Response function (matrix form)	[–]
Y_0	Static admittance	$[S]$
Y_m	Motional admittance	$[S]$
Y_p	Parallel admittance	$[S]$
Z_{IN}	Input impedance	$[\Omega]$
Z_m	Motional impedance	$[\Omega]$

Symbol	Description	Units
Greek letters		
α	Angular position	$[rad]$
α	Mass damping coefficient	$[s^{-1}]$
β	Stiffness damping coefficient	$[s^{-1}]$
δ	First order variation	[–]
Δ	Difference	[–]
ϵ	Dielectric constant	$[Cm/V]$
ε	Strain	[–]
ζ	Loop damping	[–]
θ_i	Reference phase	$[rad]$
θ_o	VCO phase	$[rad]$
θ_e	Phase error $\theta_i - \theta_o$	$[rad]$
λ	Wave length	$[m]$
ξ	Displacement	$[m]$
$\boldsymbol{\xi}$	Nodal displacement vector	$[m]$
ξ_0	perpendicular displacement amplitude	$[m]$
ρ	Density	$[kg/m^3]$
σ	Stress	$[N/m^2]$
τ_i	Time constant, i=1,2,...	$[s]$
Φ	Electric potential	$[V]$
Φ_M	Gain margin	$[^\circ]$
ω_f	Filter resonance frequency	$[rad/s]$
ω_g	Geometric frequency	$[rad/s]$
ω_{fs}	Serial filter resonance frequency	$[rad/s]$
ω_{fp}	Parallel filter mechanical resonance frequency	$[rad/s]$
ω_{gc}	Gain crossover frequency	$[rad/s]$
ω_m	Angular mechanical resonance frequency	$[rad/s]$
ω_n	Natural frequency	$[rad/s]$
Subscripts		
d	Number of design variables	
max	Maximum	
min	Minimum	
p	Parallel	
r	Rotor component	
s	Serial / Stator component	

Symbol	Description
Superscripts	
D	At constant D
E	At constant E
S	At constant S
t	Transposed
T	At constant T

Acronym	Meaning
3D	3 dimensional
AC	Alternating current
ADC	Analog to digital converter
ANN	Artificial neural network
CAP	Capture unit (edge detection)
CPU	Central processing unit
DAC	Digital to analog converter
DSC	Digital signal controller
DC	Direct current
LUP	Lookup table
MAM	Motional admittance modulation
MCLK	Master clock
NCO	Numerically controlled oscillator
PM	Permanent magnet
PUM	Piezoelectric ultrasonic motor
PZT	Lead zirconium titanate
RMS	Root mean square
SCI	Serial communication interface
RMS	Serial peripheral interface
USM	Ultrasonic motor
VCO	Voltage controlled oscillator

Curriculum Vitae

Markus FLÜCKIGER
Born August 20, 1980
Swiss Citizen
markus.flueckiger@a3.epfl.ch

SINCE 2010	R&D Engineer at Sonceboz SA, Sonceboz, Switzerland.
2005–2010	Teaching assistant and Ph.D. student at the Integrated Actuators Laboratory (LAI), Ecole Polytechnique Fédérale de Lausanne (EPFL), Switzerland. Responsible for two KTI co-founded research projects: • Design, modeling and optimisation of a piezoelectric actuator for mechatronic lock systems. • Conception of an electronic circuit enabling the indirect position measurement of an ultrasonic motor.
2000–2005	Master of Science in Microengineering, Ecole Polytechnique Fédérale de Lausanne (EPFL), Switzerland.
2002–2003	Exchange student at the Indian Institute of Technology Delhi (IITD), New Delhi, India.
1995–2000	Matura Typus C, Maturitätsschule der Region Oberaargau, Langenthal, Switzerland.

Publications

Conference contributions related to this thesis:

M. Flückiger, Y. Perriard. Indirect Rotor Position Detection Method Based on Angular Admittance Modulation of Optimally Designed Piezoelectric Ultrasonic Motors. *IEEE/ASME International Conference on Advanced Intelligent Mechatronics (AIM).* Montreal, 2010

M. Flückiger, W. Zogg, Y. Perriard. Optimal Design and Sensorless Position Control of a Piezoelectric Motor Integrated into a Mechatronic Cylinder Lock. *IEEE Energy Conversion Congress and Exposition (ECCE).* Atlanta, 2010

M. Flückiger, J.M. Fernandez, Y. Perriard. Computer-Aided Design and Optimization of Piezoelectric Ultrasonic Motors. *ELECTRIMACS 2008, 9th International Conference on Modeling and Simulation of Electric Machines, Converters and Systems.* Quebec city, 2008

J.M. Fernandez, M. Flückiger, Y. Perriard. Study of a Hollow Ultrasonic Rotory Motor. *2008 IEEE International Ultrasonics Symposium Proceedings.* Beijing, 2008, pp. 1449–1452

M. Flückiger, J.M. Fernandez, Y. Perriard. Adaptive Control of Ultrasonic Motors Using the Maximum Power Point Tracking Method. *2008 IEEE International Ultrasonics Symposium Proceedings.* Beijing, 2008, pp. 1823–1826

M. Flückiger, J.M. Fernandez, M. Giljum, Y. Perriard. Optimization of a Single Phase Ultrasonic Linear Motor. *2007 IEEE Ultrasonics Symposium Proceedings.* New York, 2007 pp. 2327–2330

M. Flückiger, M. Bullo, Y. Perriard. Sensorless Speed Control of Traveling Wave Ultrasonic Motor. *Conference Record of the 2006 IEEE Industry Applications Conference. 41st IAS Annual Meeting.* Tampa, 2006, Vol. 5: pp. 2488–2495

M. Flückiger, M. Bullo, D. Chapuis, R. Gassert, and Y. Perriard. FMRI Compatible Haptic Interface Actuated with Traveling Wave Ultrasonic Motor. *Conference Record of the 2005 IEEE Industry Applications Conference. Fourtieth IAS Annual Meeting.* Hong Kong, 2005 Vol. 3: pp. 2075–2082

Journal articles related to this thesis:

M. Flückiger, J.M. Fernandez, Y. Perriard. Finite Element Method Based Design and Optimisation Methodology for Piezoelectric Ultrasonic Motors. *Mathematics and Computers in Simulation* (under peer review)

M. Flückiger. Optimierung piezoelektrischer Ultraschallmotoren. *Bulletin SEV/VSE*, no. 19, pp. 32-37, 2007